Numerical Calculation of the Saturation Induced Field Errors in the Main Dipole of CERN's future Large Hadron Collider

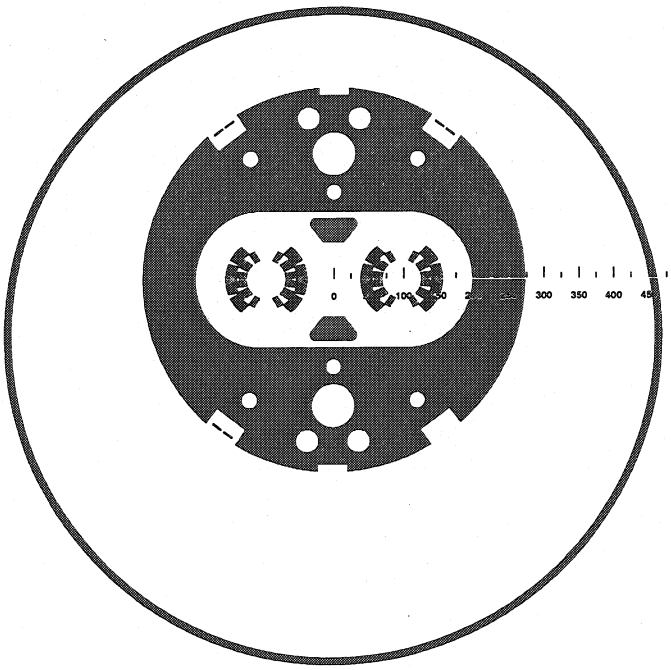

Numerical Calculation of the Saturation Induced Field Errors in the Main Dipole of CERN's future Large Hadron Collider

Dissertation

zur Erlangung des Grades

Doktor der technischen Wissenschaften

vorgelegt an der Fakultät für Elektrotechnik
der Technischen Universität Graz
von

Dipl.-Ing. Christian Paul

Graz, September 1997

Begutachter:

Ao.Univ.-Prof. Dr. techn. Kurt Preis
Ao.Univ.-Prof. Dr. techn. Oszkar Biró

TO MY PARENTS FOR THEIR

SUPPORT AND ENCOURAGEMENT

Preface

The work described in this thesis has been carried out partially in the LHC-ICP group at CERN and partially at the Institute for Fundamentals and Theory in Electrical Engineering at the Technical University of Graz, in the framework of the Doctoral Student Programme at CERN.

I wish to express my gratitude and appreciation to my Austrian supervisor, Kurt Preis, who actually initiated this work. His expert opinion has been valuable and encouraging.

I am most grateful to my current supervisor at CERN, Stephan Russenschuck, for his help and interest on this work. I have enjoyed a productive collaboration over the last two years at CERN.

I would like to thank Oszkar Biró for the excellent and complete review of this thesis. I appreciated as well his help in getting started when I was working in Graz on the implementation of the 3D reduced vector potential formulation.

I should also like to thank Theodor Tortschanoff, my former supervisor at CERN, for his efforts in promoting our ideas at CERN in the AT-MA group.

In addition, I would like thank all members of both groups for their help and pleasant atmosphere during the day.

Furthermore, I appreciated the help of the following persons:

Josef Pellizzari, for his untiring computing support,

Julio Lucas, for providing various OPERA and ANSYS results,

Angelika Paul, for correcting my English language.

Finally, I would like to thank my friends for their interest, encouragement, and our sporting activities in the mountains.

Geneva, September 1997 *Christian Paul*

Contents

List of Figures

List of Tables

Chapter 1

General Introduction

1.1 LHC - project

1.1.1 Introduction

The Large Hadron Collider (LHC) project [1] is a superconducting accelerator for protons, heavy ions, and electron-proton collisions to be installed at CERN. This collider will penetrate still further into the structure of matter and will recreate the conditions prevailing in the Universe just 10^{-12} second after the "Big Bang". The aim is to produce, not only high energy but a higher luminosity, or probability of collision, than existing hadron colliders. For example, the LEP machine, which is the latest and largest of CERN's existing accelerators, takes the fine detail with which the structure of matter can be studied down to the level of 10^{-15} millimetres. The LHC will increase this magnification by a factor of ten. The design principle of LHC is the same as that of LEP. Both machines are synchrotrons in which a stream of particles is accelerated and held in a circular orbit by thousands of electromagnets. The difference is that LEP collides electrons with their anti-particles, positrons, while both beams of particles which collide in the LHC are protons. The maximum energy of the leptons which collide in LEP is limited to about 100 GeV by the intense flux of synchrotron radiation which these light particles emit as they are bent into a circular path. The energy at which this happens to protons is much higher than for electrons and they can circulate at the highest energy that the superconducting magnets which form the guide field allow without the braking effect of this radiation. Since the machine is to be installed in the existing LEP tunnel, the peak energy is dictated by the maximum strength of the magnetic field which will hold the protons on their orbit. Using superconducting magnets which operate in super-fluid helium below 2 K will allow a guide field of about 10 Tesla, i.e. proton beams to be stored at an energy of more than 7 TeV per beam. The main performance parameters of the LHC for proton-proton operation are listed in Table (1.1).

1.1.2 Lattice

The machine [2] is subdivided into octants, each comprising one half of an arc section (1228 m long), two dispersion suppressor sections, (each 174 m long), and an insertion (528 m long). A schematic layout of the LHC with the location of the experiments is shown in Fig. (1.1). The beams cross in four points around the circumference where the physics experiments will

Table 1.1: Main Parameters of the LHC for Proton-Proton Operation

Centre-of-mass collision energy	TeV	14.0
Dipole field at collision energy	T	8.36
Injection energy	TeV	0.45
Luminosity	$cm^{-2}s^{-1}$	14.0
Circulating current/beam	A	0.54
Particles per beam		$2.9 * 10^{14}$
Stored energy per beam	MJ	334

be located. The two proton-proton experiments using high luminosity, ATLAS and CMS, are located in new underground areas. Two other experiments are programmed, ALICE which will be specialised in heavy ions physics and LHC-B devoted to B-physics.

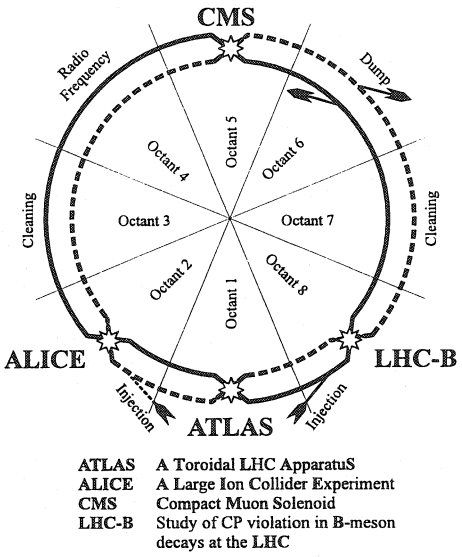

Figure 1.1: Schematic layout of the LHC

The four other straight sections, where the beams do not cross, are used for machine utilities: acceleration, beam cleaning and beam dump systems. The layout of point 4, however, which contains the r.f. acceleration system, is designed to allow the installation of an experiment in the future.

1.1.3 Magnet system

1.1.3.1 Types and number of magnets

Each of the 2456 m long arcs is made up of 23 cells formed of two identical half-cells, a bending/focusing configuration shown in Fig. (1.2) composed of three 14.2 m long twin-aperture main dipoles and a short straight section housing one 3.10 m long main quadrupole, a combined sextupole/dipole corrector, an octupole or a skew quadrupole or a trim quadrupole and a beam position monitor. Small 6-pole and 10-pole correctors are located at the ends of

the main dipoles. The main dipoles and the quadrupoles, as already mentioned in the introduction, are all of the twin-apertures design, while the corrector magnets are independent for each beam.

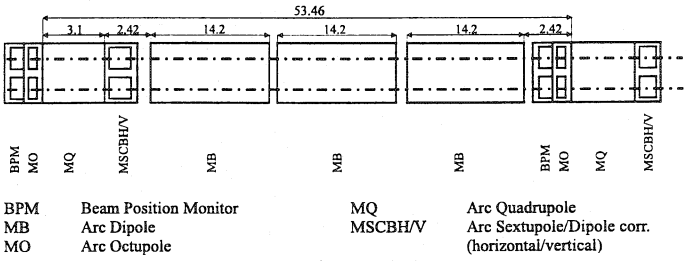

Figure 1.2: Layout of the half-cell

The dispersion suppressors, situated between the regular arcs and the insertion regions use 8 standard arc dipoles and 4 standard arc quadrupoles supplemented by small trim quadrupoles. Close to the crossing point, special dipoles recombine the two beams into a common channel. The final focusing triplet in the experimental insertions are built up from single bore 5.5m long quadrupoles (32 units) of a novel design based on graded coils wound from $NbTi$ cable. Their aperture is of 70 mm and they will produce a field gradient of up to 235 Tm^{-1}. In the LHC there will be 3444 superconducting magnet units, including 1232 main dipoles and 386 main quadrupoles, to which 4928 small correctors of the main dipole have to be added, for a total of about 8400 units of different size and importance. The LHC magnets are thus one of the most massive applications of superconductivity: the conductor quantity will be about 1200t of which 400 t will be $NbTi$ alloy, the mass to be kept at 1.8 K temperature will be about 30 000 t distributed over a 27 km circumference. In addition, there will be a number of room temperature magnets, i.e. 40 dipoles of classical construction and 48 twin-aperture quadrupoles of special design.

1.1.3.2 Technical choices

As the circumference of the machine is given by the existing tunnel, a bending field of about 8.4 T is required to reach the desired design energy. At present this high field can be reached reliably and economically in such a massive application only by the use of $NbTi$ superconductor technology and cooling the magnets to a very low temperature ($\leq 2K$) to increase the current carrying capacity versus the field of that type of conductor. The other route, i.e. using Nb_3Sn conductors at 4.2 K, is at present too expensive and too risky for a large application as the LHC magnets, though very successful short single-aperture dipole models have been built in industry and laboratories and tested at CERN [3]. Below 2.17 K, helium is in the super-fluid state, with extremely low viscosity, high heat capacity and very high thermal conductivity. These properties allow to design a particularly simple and efficient cooling scheme by which the magnet active parts operate at 1.9 K in a bath of static super-fluid helium at atmospheric pressure [4]. On the other hand, the enthalpy of all metallic parts in particular that of the superconducting cables diminishes by almost an order of magnitude between 4.2 K and 1.9 K, with a consequently faster and higher temperature rise for a given deposit of energy. This feature requires a particular care in limiting a sudden heat development and in particular any conductor motion. The electro-magnetic forces on

the conductor increases with B^2 and so does the stored electro-magnetic energy, calling for stronger force-retaining structures and more elaborate quench protection systems than for previous projects. To collide two beams of equally charged particles, they must circulate in separate magnetic channels with fields in opposite directions. Space limitations in the tunnel as well as cost considerations dictate a two-in-one magnet design, where the two rings are incorporated into the same cryostat.

1.1.4 Main dipoles

The main dipoles [2] are the most challenging components of the LHC technologically as well as from the cost point of view. The design is based on:

- design field: 8.36 T;
- twin-aperture in a common force retaining structure, flux return yoke and cryostat;
- beam distance: 194 mm;
- $NbTi$ superconductor operating in super-fluid helium at 1.9 K;
- two-shell coils with graded current density supported by collars and iron yoke surrounded and compressed by a shrinking cylinder.

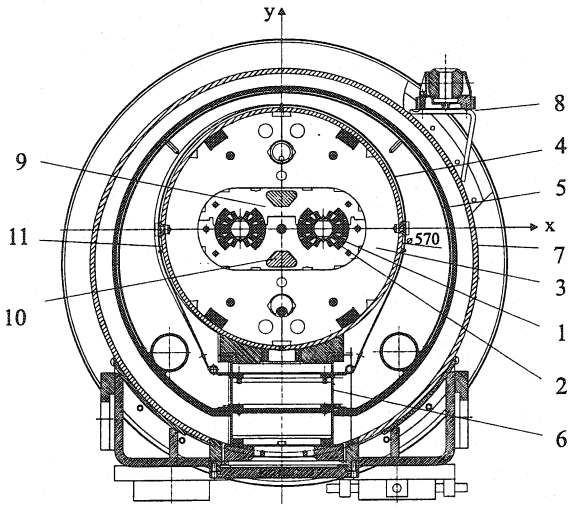

1. Beam screen 2. Cold bore 3. Cold mass at 1.9 K 4. Radiation screen,
5. Thermal shield 6. Support post 7. Vacuum vessel 8. Alignment target,
9. Aluminium collars 10. Magnetic steel inserts 11. Shrinking cylinder.

Figure 1.3: Cross-section of the dipole magnet with cryostat

The cross-section of the dipole magnet is shown in Fig. (1.3). The superconducting cables are formed of two winding layers made with keystoned cables of 15 mm width but of different thickness resulting from an optimised grading of the current density. The coils are held in place and pre-compressed by aluminium alloy collars common to both apertures, to guarantee

parallelism of the field in the two beam channels. Magnetic steel inserts in the collars, punched from 6 mm thick steel of the yoke laminations, double the thickness of the collars, correct the field distribution at the different field levels and at the same time firmly lock pairs of the collars together. The yoke which is vertically split in two halves and tightly fits and clamps the collars together is also held together by an outer welded stainless steel shrinking cylinder. The structure is designed to prevent any tensile stress in every part of the coils at all operating conditions. The shrinking cylinder is at the same time the outer shell of the helium tank, while the inner wall forms the beam vacuum chamber. The assembly between these two cylindrical walls, the "cold mass", is kept at 1.9 K in super-fluid helium at atmospheric pressure and cooled by two-phase low-pressure helium circulating in a heat exchanger tube installed in an axial hole of the iron yoke. At the ends of each dipole magnet, one small sextupole and one small decapole corrector are situated in order to compensate the corresponding multipole errors of the main dipole. The magnet is curved with a radius of 2700 m to match the beam paths.

1.1.5 Field quality

For defining the field quality [1] the following notation of a harmonic multipole analysis is used, namely:

$$B_y + iB_x = B_1 \sum_{n=1}^{\infty} (b_n + ia_n)(z/r_0)^{n-1} \tag{1.1}$$

where
B_1=magnitude of dipole field in the y (vertical) direction;
b_n=normal multipole coefficient;
a_n=skew multipole coefficient;
z=x +iy;
r_0=reference radius.

The index n=1 describes the dipole field, n=2 the quadrupole one, n=3 the sextupole, and so on. A perfect dipole magnet has just a pure B_1 vertical magnetic field. The errors with respect to this ideal field have different origins: design limitations due to the finite dimensions of the conductor and number of turns, conductor placement errors, iron saturation, coil deformations under the electro-magnetic forces, persistent and eddy currents. The lower-order multipoles tend to change with varying excitation. At low excitation these variations concern the multipoles created by persistent currents in the filaments - mainly sextupole, b_3, and decapole, b_5, components. When raising the current these perturbations die away. In the upper half of the excitation, multipoles caused by iron yoke saturation will appear. These again consist of sextupole and decapole components, but also of quadrupole, octupole, and higher-order components induced by the two-in-one geometry. The magnetic design of the yoke was aimed at keeping these multipoles, and especially their variation over the whole range of excitation, to a minimum, while at the same time reaching the highest possible dipole field to maintain an adequate load line margin.

1.2 Magnet design

From the principle electro-magnetic design of a magnet to the serial production lots of design work has to be done. Therefore, the computer program ROXIE [5] has been developed for the design of the superconducting magnets for the Large Hadron Collider (LHC) project. Together with the applied concept of features, the developer's work is simplified and design changes can be made with just a few high level commands.

1.2.1 The ROXIE program

In this section the basic structure of the ROXIE (Routine for the optimisation of magnet X-sections, inverse field calculation and coil end design) program [6] is being described. Feature modelling or "Designing by features" is an extension of parametric modelling (precondition for the use of mathematical optimisation methods) to the macroscopic level and enables to define the complicated shapes of the superconducting magnets with only a few input data. The Feature Based Design Module (FBDM) can be seen as the heart of the program which links the design tools, numerical algorithms, and the interfaces to other CAD-CAM tools. The Program structure is shown in Fig. (1.4).

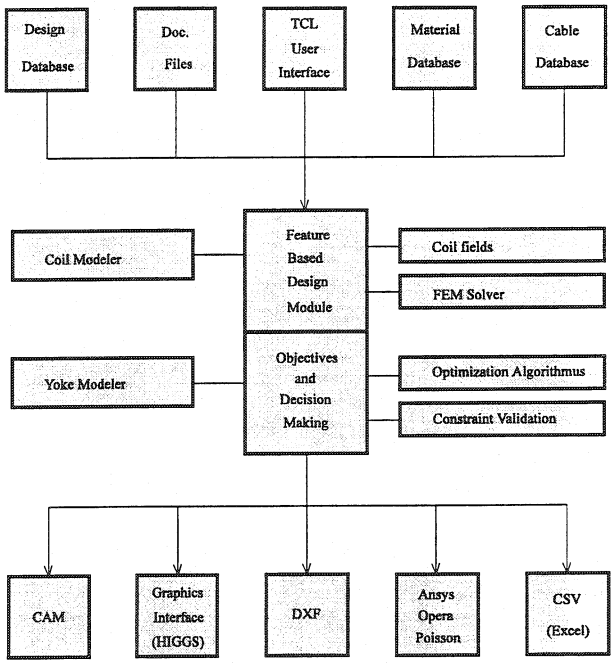

Figure 1.4: Program structure of the ROXIE program

The main steps of the integrated design process are:

- Feature-based geometry creation.
- Conceptual design using genetic algorithms .
- Calculation of field errors caused by persistent currents.
- Optimisation of coil cross-section.

- Minimisation of iron-induced multipoles.
- Calculation of quench propagation.
- 3d coil-end geometry and field optimisation.
- Calculation of the iron induced effects in the coil ends.
- Tolerance analysis.
- Production of drawings by means of a DXF interface.
- End-spacer design.
- Tracing of manufacturing errors.

An intermediate step in the integrated design process is the calculation of the iron induced effects by means of the Finite Element method. In order to properly determine these effects FE-formulations based on a reduced vector potential $\vec{A_r}$ for both the 2d and 3d case were investigated. The implementation of these methods in the feature based design concept of the ROXIE program was carried out by myself.

1.2.2 Numerical field computation methods

1.2.2.1 Influence of cable parameters on field errors

The field distribution in the LHC main dipole is dominated by the coil configuration and is, therefore extremely sensitive to conductor position errors. Furthermore, if the grading of the current density due to the keystoning of the cable is neglected in the numerical modelling an additional field error occurs. Fig. (1.5) shows a "perfect" coil with conductors aligned to the inner diameter whereas the conductors of the second coil, shown in Fig.(1.6), are aligned to the outer diameter. However, there seems to be no visible difference in the cross-sections, nevertheless, the good field region gets rather damaged. The grading of the current density is considered in the first case whereas it is neglected in the second one. In numbers, both effects cause evenly half a unit of sextupole.
Therefore a computational method that allows to model the coil and calculate the excitational field with a higher accuracy as it is possible with commercial FE packages is required.

1.2.2.2 Review of different finite element formulations

Several FE-formulations [7] to numerically solve Maxwell's equations either for the two or for the three dimensional magneto-static case based on different potentials have been developed. In the two dimensional case of a single component vector potential A_z the formulation reduces to:

$$\nabla \times \nu \nabla \times A_z = J \tag{1.2}$$

where J is the current density. The current density J appears on the right hand side of the differential equation. The consequence of this is that using the Finite Element method for

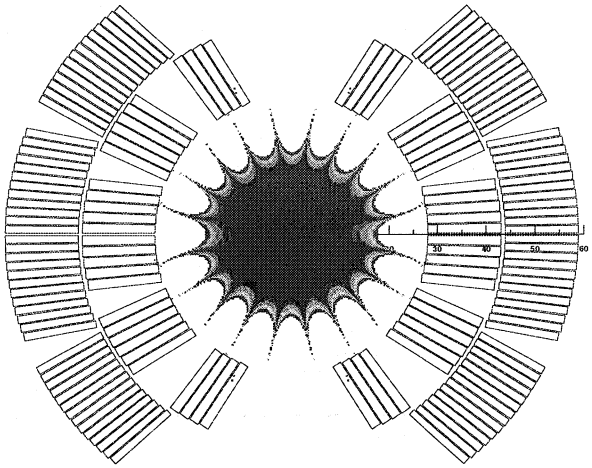

Figure 1.5: Good field region 1

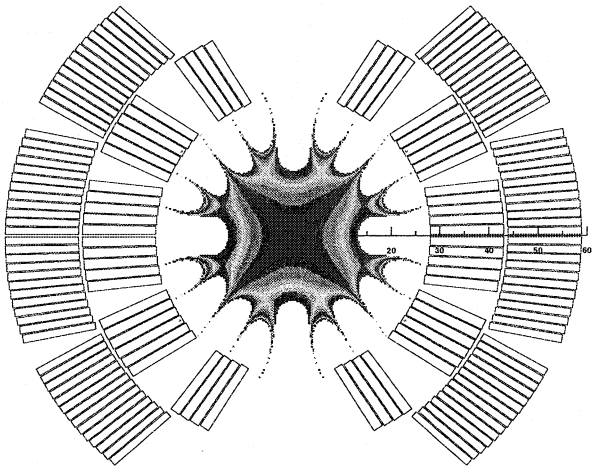

Figure 1.6: Good field region 2

the solution of this problem the relatively complicated shape of the coils has to be modelled in the FE-mesh. This might as well increase the finite element discritization in regions where the solution is of no interest.
The full vector form required for the three dimensional case may not be efficient for most problems whereas the scalar form

$$\nabla \cdot (\mu \nabla \phi) = \nabla \cdot \mu \vec{H}_s \tag{1.3}$$

is very appropriate where ϕ is the reduced scalar potential and $\vec{H}_s$ is mostly chosen as the magnetic field due to the known current density $\vec{J}$ in free space. This formulation is satisfactory as long as the permeability μ is not very high otherwise the well known cancellation errors will appear. Fortunately, the source current density in highly permeable, ferromagnetic parts is in most practical cases zero and is usually confined to coils made of non-ferromagnetic materials. In this case it is possible to derive the total magnetic field in media with high permeability as the gradient of a scalar ψ, the so called total magnetic scalar potential. In general, the field problem comprises both coils and ferromagnetic materials, thus both the reduced and the total magnetic scalar potential are to be introduced [8]. The differential equations for the two potentials read

$$\nabla \cdot (\mu_\phi \nabla \phi) = \nabla \cdot \mu_\phi \vec{H}_s \quad \text{in } \Omega_\phi, \tag{1.4}$$

$$\nabla \cdot (\mu_\psi \nabla \psi) = 0 \quad \text{in } \Omega_\psi. \tag{1.5}$$

Problems with a closed magnetic circuit surrounding coils with nonzero net current are excluded because this violates Ampere's law. This difficulty could be overcome by allowing the potential ψ to be discontinuous along cutting surfaces [8]. In fact, the identification of such cutting surfaces causes additional programming effort. Furthermore, it is well known from the TEAM workshop problem Nr. 13 that the numerical results in the region Ω_ψ are in general quantitatively higher compared to other FE-formulations [9].

1.2.2.3 $\vec{A}_r$-formulation

Here the numerical solution of the magneto-static field equations by means of a reduced vector potential is briefly described. The emphasis is put on the principal idea and the main advantage of this method for the calculation of fields in superconducting magnets.
The method was originally proposed by K. Preis et al [10] and a detailed description can be found in chapter 3.
The governing Maxwell equations for magneto-statics read:

$$\nabla \times \vec{H} = \vec{J} \tag{1.6}$$

$$\nabla \cdot \vec{B} = 0 \tag{1.7}$$

in region Ω, coupled through the material equations $\vec{B} = \mu \vec{H}$ resp. $\vec{H} = \nu \vec{B}$ together with the following boundary conditions;

$$\vec{H} \times \vec{n} = \vec{K} \quad \text{on } \Gamma_H \tag{1.8}$$

and

$$\vec{B} \cdot \vec{n} = -b_m \quad \text{on } \Gamma_B \tag{1.9}$$

where $\vec{K}$ is the surface current and b_m is a fictitious magnetic charge density on the boundary Γ of the region Ω. Because of Eq. (1.7) one can set $\vec{B} = \bigtriangledown \times \vec{A}$. Together with Eq. (1.6) it follows:

$$\bigtriangledown \times \nu \bigtriangledown \times \vec{A} = \vec{J} \tag{1.10}$$

where $\vec{J}$ is the current density. In order to make the vector potential $\vec{A}$ unique it is necessary to define its divergence and, on the boundary Γ, either its normal component or its tangential component. By introducing the Coulomb gauge described in [7] and chapter 3 and merging both differential equations the complete $\vec{A}$-formulation with its boundary conditions reads:

$$\begin{aligned}
\bigtriangledown \times \nu \bigtriangledown \times \vec{A} - \bigtriangledown \nu \bigtriangledown \cdot \vec{A} &= \vec{J} \quad \text{in } \Omega, && (1.11)\\
\nu \bigtriangledown \times \vec{A} \times \vec{n} &= \vec{K} \quad \text{on } \Gamma_H, && (1.12)\\
\vec{A} \cdot \vec{n} &= 0 \quad \text{on } \Gamma_H, && (1.13)\\
\vec{n} \times \vec{A} &= \vec{\alpha} \quad \text{on } \Gamma_B, && (1.14)\\
\nu \bigtriangledown \cdot \vec{A} &= 0 \quad \text{on } \Gamma_B. && (1.15)
\end{aligned}$$

As already stated above the current density in Eq. (1.11) has to be eliminated.

Therefore, the vector potential $\vec{A}$ is split into parts as

$$\vec{A} = \vec{A}_s + \vec{A}_r \tag{1.16}$$

where $\vec{A}_r$ is the reduced vector potential due to the magnetisation and $\vec{A}_s$ is the impressed vector potential due to the source currents in free space. The relationship between the impressed vector potential $\vec{A}_s$ and the field vector $\vec{H}_s$ is,

$$\bigtriangledown \times \vec{A}_s = \mu_0 \vec{H}_s \tag{1.17}$$

and by definition for conductor source regions with current density $\vec{J}_s$ the field vector $\vec{H}_s$ is given by,

$$\vec{H}_s = \frac{1}{4\pi} \int_{\Omega} \vec{J}_s \times \bigtriangledown (\frac{1}{R})\, d\Omega \tag{1.18}$$

where $R = \mid r_q - r_a \mid$ is the distance from the source point r_q to the field point r_a. Eq. (1.18) is known as the Biot Savart Law [11].

The field equations in terms of a reduced vector potential $\vec{A}_r$ then differ for the iron region Ω_i and the air region Ω_a where the sources (coils) are located. Following the same procedure as for the total vector potential leads to:

$$\nabla \times \nu \nabla \times \vec{A}_{r_i} - \nabla \nu \nabla \cdot \vec{A}_{r_i} = -\nabla \times \nu \nabla \times \vec{A}_s \quad \text{in } \Omega_i, \tag{1.19}$$

$$\nabla \times \nu_0 \nabla \times \vec{A}_{r_a} - \nabla \nu_0 \nabla \cdot \vec{A}_{r_a} = 0. \quad \text{in } \Omega_a. \tag{1.20}$$

Taking the curl of Eq. (1.17) gives $\nabla \times \nu_0 \nabla \times \vec{A}_s = \nabla \times \vec{H}_s$, which is obviously representing the current density $\vec{J}_s$. At this stage it is sufficient to show the complete $\vec{A}_r$-formulation where the surface current density $\vec{K}$ and the fictitious magnetic charge density b_m are assumed to be zero:

$$\begin{aligned}
\nabla \times \nu \nabla \times \vec{A}_{r_i} - \nabla \nu \nabla \cdot \vec{A}_{r_i} &= -\nabla \times \nu \nabla \times \vec{A}_s && \text{in } \Omega_i, && (1.21)\\
\nabla \times \nu_0 \nabla \times \vec{A}_{r_a} - \nabla \nu_0 \nabla \cdot \vec{A}_{r_a} &= 0 && \text{in } \Omega_a, && (1.22)\\
\nu \nabla \times \vec{A}_{r_i} \times \vec{n} &= 0 && \text{on } \Gamma_{H_i}, && (1.23)\\
\vec{A}_{r_i} \cdot \vec{n} &= 0 && \text{on } \Gamma_{H_i}, && (1.24)\\
\vec{n} \times \vec{A}_{r_i} &= 0 && \text{on } \Gamma_{B_i}, && (1.25)\\
\nu \nabla \cdot \vec{A}_{r_i} &= 0 && \text{on } \Gamma_{B_i}, && (1.26)\\
\nu_0 \nabla \times \vec{A}_{r_a} \times \vec{n} &= 0 && \text{on } \Gamma_{H_a}, && (1.27)\\
\vec{A}_{r_a} \cdot \vec{n} &= 0 && \text{on } \Gamma_{H_a}, && (1.28)\\
\vec{n} \times \vec{A}_{r_a} &= 0 && \text{on } \Gamma_{B_a}, && (1.29)\\
\nu_0 \nabla \cdot \vec{A}_{r_a} &= 0 && \text{on } \Gamma_{B_a}, && (1.30)
\end{aligned}$$

and along the interface Γ_{ai} between the iron and air region

$$(\nu_0 \nabla \times \vec{A}_{r_a} + \nu_0 \nabla \times \vec{A}_s) \times \vec{n_a} + (\nu \nabla \times \vec{A}_{r_i} + \nu \nabla \times \vec{A}_s) \times \vec{n_i} = 0 \quad \text{on } \Gamma_{ai}. \tag{1.31}$$

Using the node-based finite elements for the 3d implementation would create numerical convergence problems. The global set of shape functions is constructed to be continuous on the element boundaries. Since the reluctivity ν jumps on the material boundaries Γ_{ai} the condition

$$(\nu_0 \nabla \cdot \vec{A}_{r_a}) \cdot \vec{n_a} + (\nu \nabla \cdot \vec{A}_{r_i}) \cdot \vec{n_i} = 0 \quad \text{on } \Gamma_{ai} \tag{1.32}$$

is not satisfied. In the 2d case the divergence of the vector potential is identically zero and therefore this particular problem does not appear.
The use of a rather new type of finite elements in electro-magnetic field modelling, namely edge-elements which were first introduced by J. C. Nèdèlec [12] in 1980 is an alternative to eliminate these convergence problems. These are elements whose degrees of freedom are associated with edges, rather than with nodes. They have mostly been used to compute 3d vector electro-magnetic fields in microwave engineering. The most important property is that they allow the normal component of the vector to be discontinuous from one element to the next. Various tetrahedral and hexahedral elements have been developed [13],[14],[15].

1.3 Scope of the thesis

This thesis consists of the following four parts:

- In *chapter 2* a brief introduction to the electrodynamic behaviour of superconducting accelerator magnets is given. A survey of the main magnetostatic field problems arising in context with superconducting magnets is presented. The cardinal point is the treatment of the complicated coil shapes in the FE - model shown in Fig. (1.5).

- In *chapter 3* the FE-method is briefly described. The solution of the Maxwell equations for the magnetostatic field problem by means of a total vector $\vec{A}$ potential is dealt with. This FE-formulation has an important drawback when applying it to coil-dominated accelerator magnets. Since the coil structure is part of the FE-mesh a detailed description of the real coil geometry is hardly possible. By introducing a reduced vector potential $\vec{A_r}$ the coil structure can be eliminated from the FE-mesh.

  In *chapter 4* the numerical accuracy of this method is investigated by confronting results calculated with the most frequently used FE-software packages at CERN. Furthermore, an estimation of the saturation induced field errors of the present design of the LHC main dipole is given.

- The *chapter 5* is dedicated to the extension of the 2D reduced vector potential formulation to three dimensions. A formulation with node-based elements requires the continuity of $(\nu \bigtriangledown \cdot \vec{A}) \cdot \vec{n}$ on the material boundaries between iron and air. In the 2D formulation this continuity condition is implicitly satisfied since the divergence of the vector potential $\vec{A}$ is identically zero. In order to overcome these convergence problems a rather new type of finite elements, namely edge-elements are applied.

  In *chapter 6* the applicability of the 3D formulation to accelerator magnets is investigated. Firstly, a comparison of 2D and 3D results has been presented. Secondly, the field components and an estimate of the integrated harmonics in the magnet ends of the LHC main dipole are given.

- In *chapter 7* general conclusions are presented concerning the implementation of the reduced vector potential formulation to the classical ROXIE program. The improvement to the integrated design process is stated. The applicability of this FEM-formulation to superconducting accelerator magnets is discussed.

Chapter 2

Superconducting Accelerator Magnets

2.1 Introduction

In circular accelerators the beam energy is proportional to the machine radius and the bending magnetic field [16]. Therefore, it is of great interest to develop dipoles with continuously higher magnetic fields. Normal magnets with iron pole shoes are limited to dipole fields of about 2 Tesla and quadrupole gradients of 20 Tm^{-1} whereas superconducting magnets reach dipole fields up to 10 Tesla and quadrupole gradients of about 250 Tm^{-1}. Superconducting accelerator magnets fundamentally differ in their design compared to other superconducting magnets (e.g. large solenoids for particle detectors or toroidal coils for nuclear fusion machines):

- Very high current densities are needed to produce the required high bending fields;
- Strong electro-magnetic forces;
- extremely precise magnetic field distribution over a small aperture;
- High reliability and reproducibility.

Superconducting magnets have a number of properties which can not be found in normal magnets. Firstly, a superconducting magnet can quench. A quench [17] is the transition from the superconducting to the normal state and occurs if one of the three parameters: temperature, magnetic field or current density exceeds a critical value. In case of a quench, the stored energy should not destroy machine components and thus, a reliable protection system is required. Secondly, an unpleasant feature of superconducting magnets is the presence of the persistent eddy currents [18]. They are induced in the filaments of the superconductor during a change of the magnetic field. Since the resistance of the superconductor vanishes these currents persist for a long time as they decay only through flux creep. Fortunately, at injection energy where they really disturb they can be partly compensated by the coil design. Thirdly, superconducting accelerator magnets are generally equipped with an iron yoke. Its purpose differs considerably from the yoke of a normal magnet. On the one hand the inner magnetic field is increased by 10 to 40 %, depending on the proximity between coil and yoke and on the other hand the stored magnetic energy is reduced which is very important in case of a quench. The yoke shields as well the surroundings against the high inner field.

Furthermore, a cryogenic cooling system [19] is needed in order to keep the magnet system at operation temperature which is in the case of the LHC 1.9 K.

Basically, superconducting magnets can be categorised in three different classes:

- Magnets in which the field distribution is dominated by the coil configuration, e.g. the LHC main dipoles [1] and quadrupoles as many other superconducting magnets take part in this class.
- Iron dominated magnets, called super-ferric, in which the iron pole shape determines the field distribution (e.g. RHIC sextupoles [20]).
- Magnets in which both coil and yoke strongly contribute to produce the required field [21].

2.2 Field calculations for SC-accelerator magnets

2.2.1 Multipole expansion for a single current conductor

In beam guiding magnets the field problem is essentially bidimensional apart from the magnet ends. The current conductors in the straight section of the magnet are parallel to the beam direction and can be considered as infinitely long since the transverse dimensions of the magnet are much smaller than its length. Therefore, the adequate method is a two dimensional multipole expansion. Fig. (2.1) shows a typical superconducting dipole with its beam direction chosen to be the z axis of a cylindrical coordinate system (r,Θ,z).

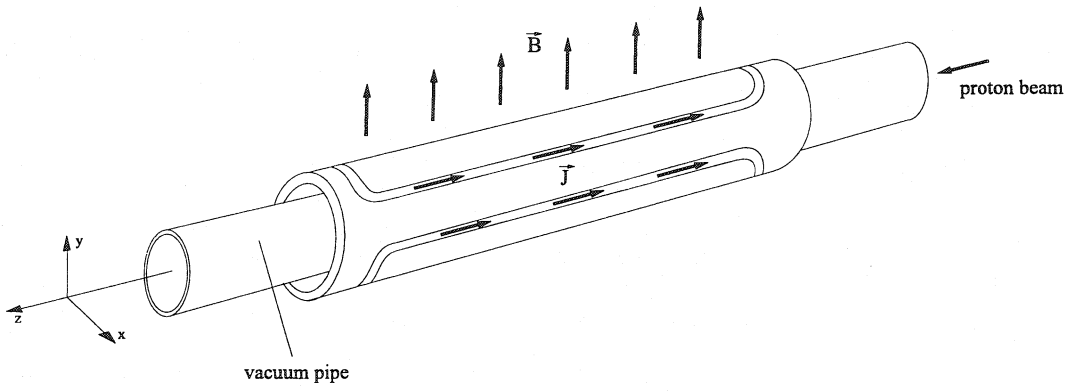

Figure 2.1: Schematic view of a SC dipole coil

Now we consider a line current in the positive z direction located at $\vec{r_q}$. The vector potential [11] generated by this current is then given by

$$A_z(r_a, \Theta) = -\frac{\mu_0 I}{2\pi} \ln\left(\frac{R}{r_q}\right) \tag{2.1}$$

where $R = \mid \vec{r_q} - \vec{r_a} \mid$ is the distance from the source point $\vec{r_q}$ to the field point $\vec{r_a}$.

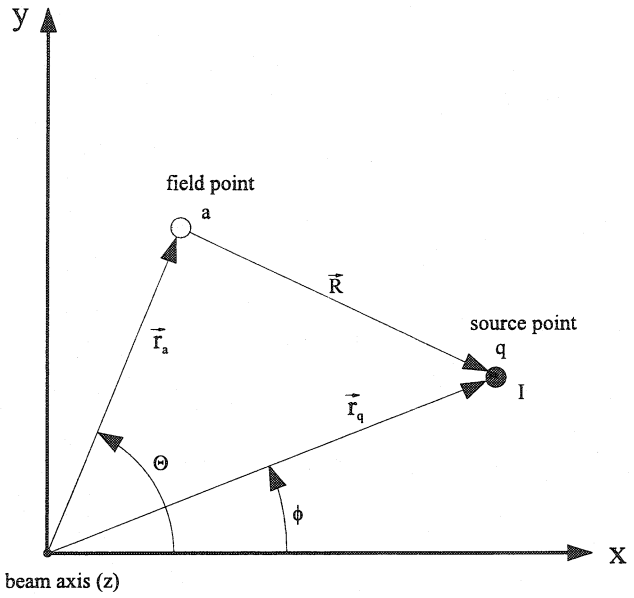

Figure 2.2: Field calculation for a line current

With the familiar power series for arbitrary complex numbers ξ with $|\,\xi\,| < 1$

$$\ln(1-\xi) = -\xi - \frac{1}{2}\xi^2 - \frac{1}{3}\xi^3 - \cdots - \frac{1}{n}\xi^n - \cdots \tag{2.2}$$

and the following identities

$$R^2 = r_q^2\,(\,1 - \frac{r_a}{r_q}\,e^{\,i(\phi-\Theta)}\,)\,(\,1 - \frac{r_a}{r_q}\,e^{\,-i(\phi-\Theta)}\,) \tag{2.3}$$

$$\ln(\frac{R}{r_q}) = \frac{1}{2}\ln(\,1 - \frac{r_a}{r_q}\,e^{\,i(\phi-\Theta)}\,) + \frac{1}{2}\ln(\,1 - \frac{r_a}{r_q}\,e^{-\,i(\phi-\Theta)}\,) \tag{2.4}$$

Eq. (2.1) reduces to

$$A_z(r_a,\Theta) = \frac{\mu_0 I}{2\pi}\sum_{n=1}^{\infty}\frac{1}{n}(\frac{r_a}{r_q})^n \cos[\,n\,(\phi-\Theta)\,] \tag{2.5}$$

for $r_a < r_q$.

In case of $r_a > r_q$ we rewrite Eq. (2.3)

$$R^2 = r_a^2\,(\,1 - \frac{r_q}{r_a}\,e^{\,i(\phi-\Theta)}\,)\,(\,1 - \frac{r_q}{r_a}\,e^{\,-i(\phi-\Theta)}\,) \tag{2.6}$$

$$\tag{2.7}$$

and obtain the z-component of the vector potential as follows:

$$A_z(r_a,\Theta) = -\frac{\mu_0 I}{2\pi}\ln(\frac{r_a}{r_q}) + \frac{\mu_0 I}{2\pi}\sum_{n=1}^{\infty}\frac{1}{n}(\frac{r_q}{r_a})^n \cos[\,n\,(\phi-\Theta)\,]. \tag{2.8}$$

The field components derive from the well known equation

$$\vec{B}(r,\Theta,z) = \bigtriangledown \times \vec{A} \tag{2.9}$$

and we get for $r_a < r_q$

$$B_\Theta = -\frac{\mu_0 I}{2\pi r_q} \sum_{n=1}^{\infty} (\frac{r_a}{r_q})^{n-1} \cos\left[n\left(\phi-\Theta\right)\right] \tag{2.10}$$

$$B_r = \frac{\mu_0 I}{2\pi r_q} \sum_{n=1}^{\infty} (\frac{r_a}{r_q})^{n-1} \sin\left[n\left(\phi-\Theta\right)\right] \tag{2.11}$$

$$B_z = 0 \tag{2.12}$$

and for $r_a > r_q$

$$B_\Theta = \frac{\mu_0 I}{2\pi r_a} + \frac{\mu_0 I}{2\pi r_q} \sum_{n=1}^{\infty} (\frac{r_q}{r_a})^{n+1} \cos\left[n\left(\phi-\Theta\right)\right] \tag{2.13}$$

$$B_r = \frac{\mu_0 I}{2\pi r_q} \sum_{n=1}^{\infty} (\frac{r_q}{r_a})^{n+1} \sin\left[n\left(\phi-\Theta\right)\right] \tag{2.14}$$

$$B_z = 0. \tag{2.15}$$

Looking closer at the n^{th} - Fourier component in the multipole expansion of the single line current in Eq. (2.5) two terms appear

$$A_{z,n}(r_a,\Theta) = \frac{\mu_0 I}{2\pi} (\frac{1}{n}) (\frac{r_q}{r_a})^n \left[\cos(n\phi)\ \cos(n\Theta) + \sin(n\phi)\ \sin(n\Theta)\right] \tag{2.16}$$

$$= b_n \cos(n\Theta) + a_n \sin(n\Theta). \tag{2.17}$$

The first term is called the "normal" multipole whereas the second is understood as the "skew" multipole. A normal multipole is transferred into a skew multipole by a rotation of $(\frac{\pi}{2m})$.

2.2.2 Generation of pure multipole fields

As it was shown in the previous section a single line current generates multipole fields of any order. Now we investigate uniform current distributions on a cylinder of radius r_a. A current density of the form

$$I_{(\phi)} = I_0 \cos(m\phi) \tag{2.18}$$

produces a pure multipole field of order $n = m$. The vector potential generated by the current distribution of Eq. (2.18) inside the cylinder is

$$A_z(r,\Theta) = \frac{\mu_0 I_0}{2\pi} \sum_{n=1}^{\infty} \frac{1}{n} (\frac{r}{r_q})^n \int_0^{2\pi} \cos(m\phi) \cos\left[n\left(\phi-\Theta\right)\right] d\phi. \tag{2.19}$$

Evaluating the integral in Eq. (2.19) with respect to

$$\cos\left[n\left(\phi-\Theta\right)\right]=\cos(n\phi)\cos(n\Theta)+\sin(n\phi)\sin(n\Theta) \tag{2.20}$$

gives

$$A_z(r,\Theta)=\frac{\mu_0 I_0}{2}\frac{1}{m}(\frac{r}{r_q})^m\cos(m\Theta). \tag{2.21}$$

So the magnetic field components reduce to

$$B_\Theta = -\frac{\mu_0 I_0}{2r_q}(\frac{r}{r_q})^{m-1}\cos(m\Theta) \tag{2.22}$$

$$B_r = -\frac{\mu_0 I_0}{2r_q}(\frac{r}{r_q})^{m-1}\sin(m\Theta). \tag{2.23}$$

For the special cases m=1, m=2 and m=3 the current distributions and the field patterns in Cartesian coordinates are:

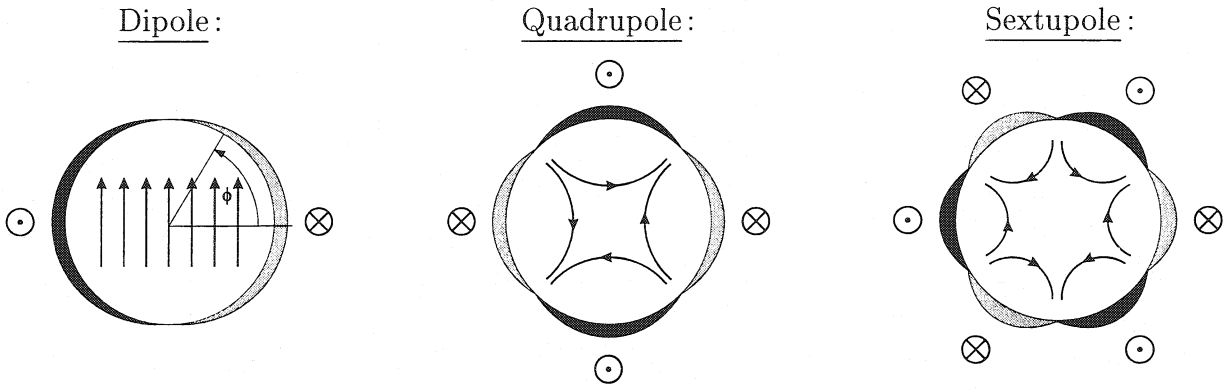

Figure 2.3: Generation of pure multipole fields by current distributions

2.2.3 Approximation of pure multipole coils

From the technological point of view a current distribution with $\cos\phi$ dependency can only be approximated by stacking discrete conductors. Different stacking techniques are applied to using concentric current shells, current shells with separated blocks, and block configurations with horizontal or vertical layers. Fig. (2.4) shows an ideal dipole configuration and some of its practical approximations.
For the LHC main dipoles and quadrupoles a Rutherford-type cable with keystoning is used. The coils are formed of two winding layers with five separate blocks, three blocks in the inner layer and two of them in the outer layer as shown in Fig. (2.5) .

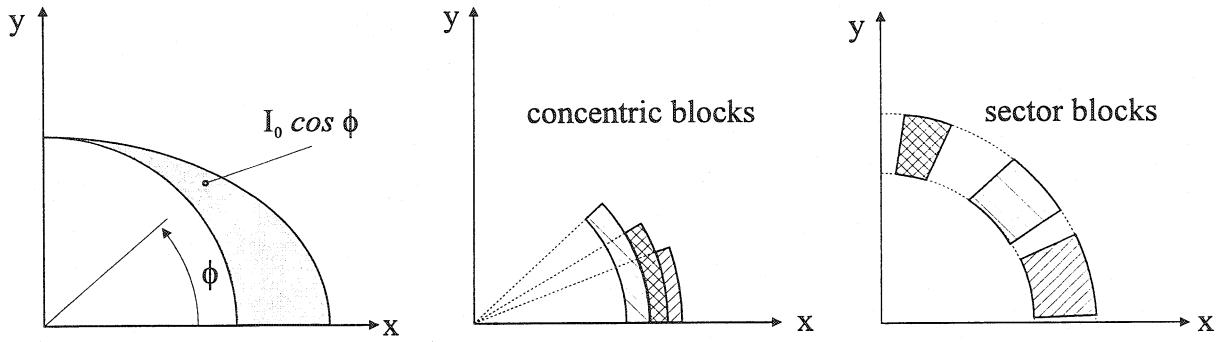

Figure 2.4: Practical approximation of a $\cos\phi$ current distribution

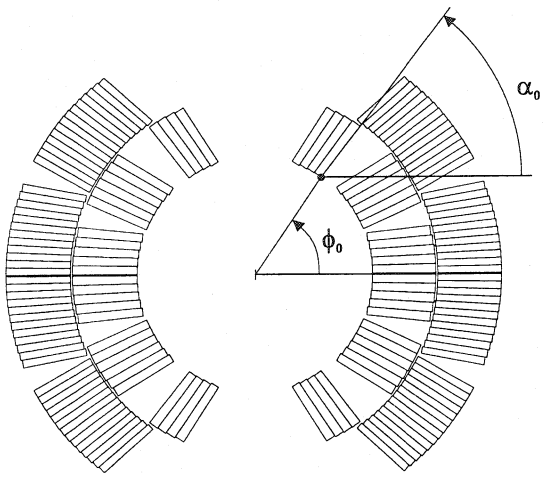

α_0 ... inclination angle
ϕ_0 ... positioning angle

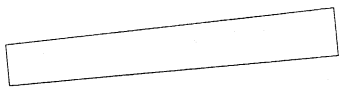

Cross-section of the Rutherford-type cable

Figure 2.5: Coil cross-section of the LHC main dipole with a Rutherford-type cable

Normally, the multipole coils have defined symmetries thus not the entire spectrum of multipoles appears. In the coil with a dipole symmetry, i.e. the LHC main dipole, all skew components disappear as well as the even normal multipoles ($\{n \mid n = (2m+1) \quad \forall \quad m = 0, \cdots, \infty\}$). The magnitude of the field of a multipole n is influenced by the arrangement of the conductor blocks. Unwanted multipoles can be eliminated by conveniently choosing the arrangement of the blocks and the current density. The position of each block is determined by the positioning angle ϕ_0 and the inclination angle α_0 of its first conductor with respect to the distance to the centre.

2.2.4 Influence of the iron yoke

The main dipole magnet Fig. (1.3) for the LHC accelerator is equipped with an iron yoke. It keeps together the superconducting coils which are mounted in the aluminium collars and absorbs the huge acting electro-magnetic forces. The increase of the magnetic field on the beam axis is of a magnitude of about 15 %. Furthermore, the fringe field of the coils outside the magnet is greatly reduced to approximately 60 mT at the nominal operation point at 8.4 T. The influence of the iron yoke can be roughly determined by means of the method of image currents [17] provided the iron is not saturated and the permeability μ is uniform.
The field errors caused by the saturation effects depend strongly on the coil-yoke distance. In principle, there are two classical types of magnets, namely the "warm" iron magnets and the "cold" iron magnets [17]. In the warm iron magnets the yoke is located outside the cryostat thus fairly far away from the coil. The saturation effects can therefore be neglected whereas for cold iron magnets they have to be carefully investigated. The LHC main dipole belongs to the second group. The first higher order multipoles (4-pole and 6-pole) are mainly concerned. The quadrupole component results from the two-in-one design the magnetic flux being divided into two paths, one across the mid-plane $x = 0$ into the second aperture and one across the plane $y = 0$ into the lower half of the yoke. Lower order skew components arise as the vacuum vessel is off-centred with respect to the magnet horizontal axis. Numerical methods are needed to compute the field errors caused by the saturation of the iron yoke and other ferromagnetic material surrounding the magnets.

2.2.5 Variation of lower order multipoles during ramp

A stepwise excitation or ramping of the accelerator magnet complex [22] is necessary to reach the nominal operation point at 8.4 T. In the present design of the main dipole, the lower order multipoles vary much with excitation. The quadrupole error gets strongly pronounced at fields of about 7.5 T and the sextupole error fairly increases at fields higher than 6 T. About -0.7 units of sextupole result from the iron geometry. For beam stability reasons the goal of the design is to keep the variation within certain limits. Fig. (2.6) shows the typical behaviour of the lower order harmonics as a function of the main field of the LHC main dipole calculated by means of the extended ROXIE program.

2.2.6 Magnet end fields

As shown in Fig. (2.1) the coil of a dipole magnet consists in principle of two parts: the straight section and the end sections. In the straight section, the design goals are rather

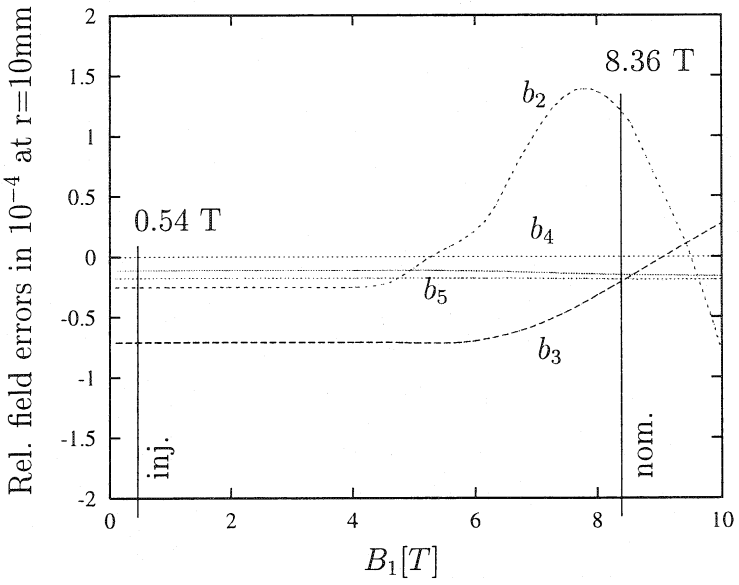

Figure 2.6: Typical behaviour of the multipole errors versus excitation due to coil geometry and iron yoke saturation of the LHC main dipole (*inj.* ... injection field, *nom.* ... nominal field)

simple. The conductors are grouped in blocks and their position is chosen to minimise the field errors in the aperture. Optimisation algorithms [23] have been applied to find the optimal arrangement of the blocks and to minimise the peak fields in the conductors.
In contrast, the design issues for the coil ends get numerous. A widely used mathematical description for coil ends is the constant perimeter model [24]. Fig. (2.7) shows a constant perimeter coil-end designed for the LHC with the ROXIE program. The design of the ends depends both on magnetic and mechanical considerations. The main magnetic objectives are to minimise integrated multipoles and to reduce the fields at the conductors whereas mechanical stability and the minimisation of the geometrical length to limit the loss of magnetic length are the most important mechanical ones. It is obvious that some kind of compromise has to be found for the optimal choice of the objectives.

2.3 Load-line characteristic

As the reduced field coming from the iron magnetization and the excitational field from the coil can be calculated separately it is also possible to calculate the peak field in the coils with a higher accuracy than before. A line current is assumed to represent a superconducting strand in the model of a conductor as shown in Fig. (2.8).
The peak field in the conductor is evaluated at four points surrounding the line current to avoid the result being singular. If the field is averaged over these four points the self field of the strand cancels out. If the self field has to be considered, the maximum of the field in the four surrounding points is taken. As the self field is not compensated in the critical current measurement of the strands it is therefore not considered in the ROXIE calculations. It is

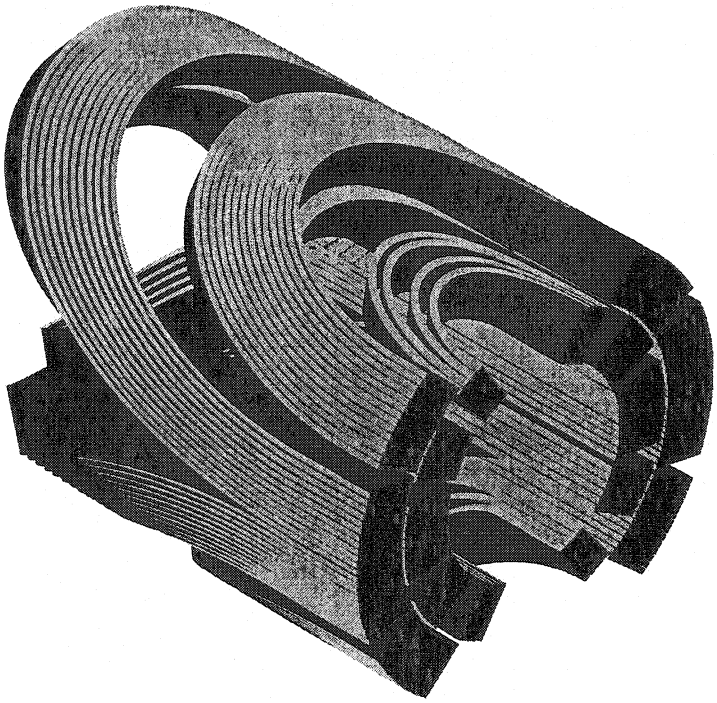

Figure 2.7: 3D view of the coil-end at the non-connection side of a five-block LHC-type dipole magnet

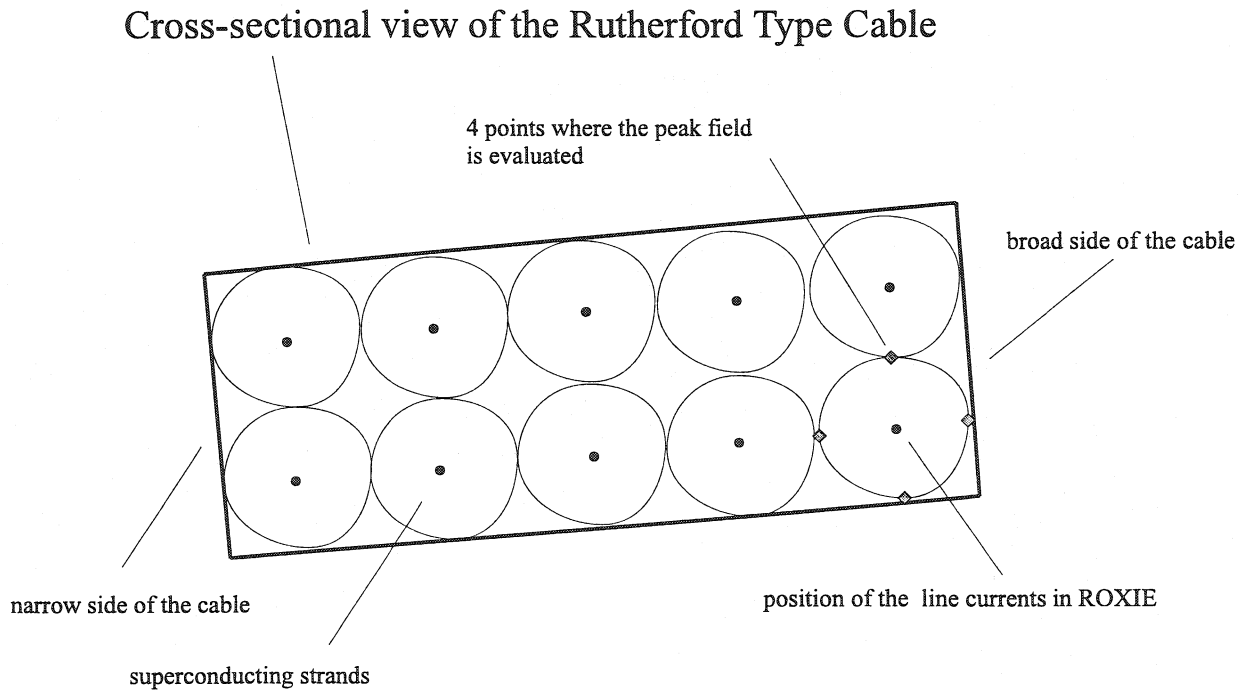

Figure 2.8: Peak field calculation in a superconducting cable

incorporated in the values for the critical current density used for the load line characteristic calculations. Fig. (2.9) shows the load line curves for the coil blocks of the main dipole magnet. Blocks 1 and 2 are in the outer layer, blocks 3 - 5 are in the inner layer.

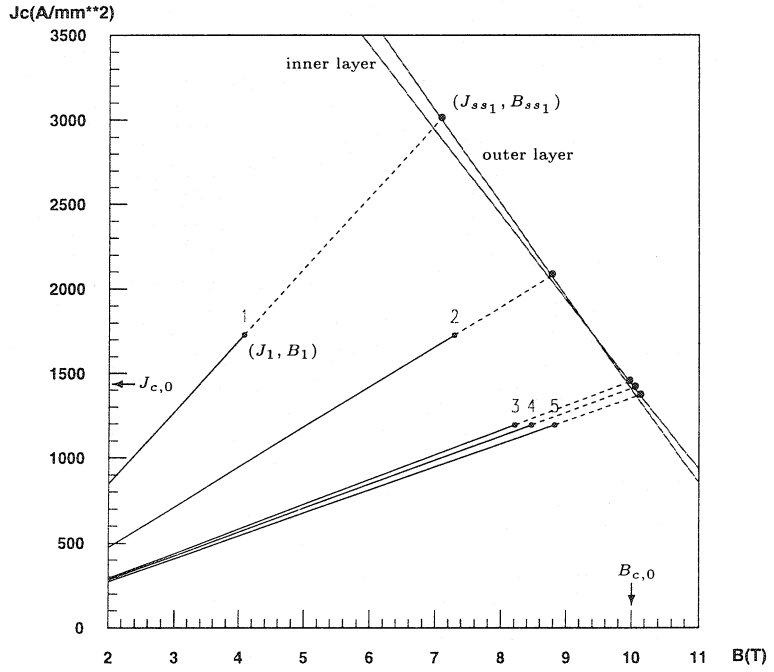

Figure 2.9: Load-line for the main dipole. Blocks 1 and 2 are in the outer layer, 3,4,and 5 are the inner layer coil blocks

The point J_{ss_1}, B_{ss_1} for coil block 1 is derived from solving the equations

$$B_{ss_1} = \lambda_1 \cdot B_1 = B_{c,0} + \lambda_2 \tag{2.24}$$

$$J_{ss_1} = \lambda_1 \cdot J_1 = J_{c,0} + \lambda_2 \frac{dJ_c}{dB}. \tag{2.25}$$

The current density in the superconductor is given by

$$J_c = \frac{I_{cable}}{A_{sc}} = \frac{I_{cable} \cdot (1 + \frac{Cu}{Sc})}{n \cdot \frac{d^2 \cdot \pi}{4}} \tag{2.26}$$

where I_{cable} is the total current in the cable, n is the number of strands in the cable and d is the strand diameter. From the critical current density $J_{c,0}$ and dJ_c/dB the percentage of the critical current density in the operating point can be evaluated. The short sample $B - J$ characteristic curves are approximated by

$$J_c = -\frac{dJ_c}{dB} \cdot B + J_{c,0} \tag{2.27}$$

at 1.9 Kelvin.

The assumptions of the cable characteristics [1] are:

Inner layer:
$T_{c,0}$=1.9 K, $B_{c,0}$=10 T, $J_{c,0}$=1433.3 Amm^{-2}, $\frac{dJ_c}{dB}$=500.34 $Amm^{-2}T^{-1}$.
Outer layer:
$T_{c,0}$=1.9 K, $B_{c,0}$= 9 T, $J_{c,0}$=1953.0 Amm^{-2}, $\frac{dJ_c}{dB}$=550.03 $Amm^{-2}T^{-1}$.

Chapter 3

The $\vec{A}_r$-Formulation with Node-based Elements

3.1 Mathematical details

In this chapter the numerical solution of the magnetostatic field equations by means of a reduced vector potential is reviewed. The method was originally proposed by K. Preis et al. [10]. The method of description follows the investigations done in *"CAD in electromagnetism"* [7]. For completeness, the total vector potential formulation is stated first in order to discuss the uniqueness of the vector potential and the gauging procedure.
The first step in the numerical solution of differential equations is to reduce them to a system of algebraic equations. This has been approached differently by mathematicians and engineers. The most famous ones are the method of finite differences [25], variational principles [26] and Ritz's method [27]. Here, Ritz's method is used and its numerical implementation in form of the finite element method is worked out.

3.1.1 Magnetostatic field equations

The analysis of electromagnetic field problems is based on Maxwell's equations [11]. The equations describing the magnetostatic field are

$$\nabla \times \vec{H} = \vec{J} \tag{3.1}$$

$$\nabla \cdot \vec{B} = 0 \tag{3.2}$$

in a region Ω. The field vectors are not independent since they are related by material properties, given by the following equations

$$\vec{B} = \mu \vec{H} \tag{3.3}$$

or

$$\vec{H} = \nu \vec{B} \tag{3.4}$$

where μ and ν are the material permeability and reluctivity . In practice μ and ν are often field dependent quantities.

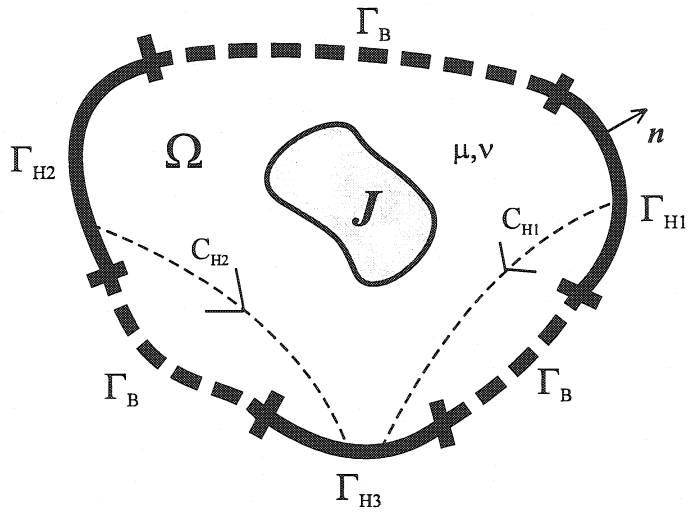

Figure 3.1: The elementary model problem for a magnetostatic field

A typical magnetostatic field problem can be defined as it is shown in Fig. (3.1). It may consist of a region Ω bounded by the surface Γ which itself consists of two different parts Γ_H and Γ_B. The field vectors $\vec{B}$ and $\vec{H}$ must satisfy the following boundary conditions;

$$\vec{H} \times \vec{n} = \vec{K} \quad \text{on } \Gamma_H \tag{3.5}$$

and

$$\vec{B} \cdot \vec{n} = -b_m \quad \text{on } \Gamma_B \tag{3.6}$$

where $\vec{K}$ is the surface current and b_m is a fictitious magnetic charge density.
If, as it is shown in Fig. (3.1), the surface Γ_H consists of n_H disjunct parts Γ_{H_i} certain integral conditions, either the surface flux ψ_i on Γ_{H_i}

$$\int_{\Gamma_{H_i}} \vec{B} \cdot \vec{n}\, d\Gamma \;=\; -\psi_i \quad \forall \quad \text{i=1,2,}\cdots\text{,}n_H\text{-1} \tag{3.7}$$

or the magnetic voltage U_{m_i} integrated along C_{H_i}

$$\int_{C_{H_i}} \vec{H} \cdot d\vec{l} \;=\; U_{m_i} \quad \forall \quad \text{i=1,2,}\cdots\text{,}n_H\text{-1} \tag{3.8}$$

have to be specified where C_{H_i} is the integration path connecting the surface Γ_{H_i} to the section $\Gamma_{H_{n_H}}$.

3.1.2 Uniqueness of vector potentials

Since the field vector $\vec{B}$ has a zero divergence, Eq. (3.2), it can be expressed in terms of a magnetic vector potential $\vec{A}$

$$\vec{B} = \nabla \times \vec{A}. \tag{3.9}$$

From Eq. (3.1) and Eq. (3.9) it follows that,

$$\nabla \times \nu \nabla \times \vec{A} = \vec{J}. \tag{3.10}$$

Choosing the constraints (3.7), the magnetostatic field equations written in terms of a vector potential $\vec{A}$ are

$$\begin{aligned}
\nabla \times \nu \nabla \times \vec{A} &= \vec{J} \quad \text{in } \Omega, && (3.11)\\
\nu \nabla \times \vec{A} \times \vec{n} &= \vec{K} \quad \text{on } \Gamma_H, && (3.12)\\
\nabla \times \vec{A} \cdot \vec{n} &= -b_m \quad \text{on } \Gamma_B, && (3.13)\\
\int_{\Gamma_{H_i}} \nabla \times \vec{A} \cdot \vec{n}\, d\Gamma &= -\psi_i \quad \forall \quad \text{i=1,2,}\cdots\text{,}n_H\text{-1.} && (3.14)
\end{aligned}$$

It is well known that this system of equations is unique for the field vectors $\vec{H}$ and $\vec{B}$ but does not define the vector potential uniquely. This can be shown by adding a gradient vector of any type to $\vec{A}$ and the curl of $\vec{A}$ remains unchanged.

In order to make the vector potential $\vec{A}$ unique [7] it is necessary to define its divergence and, on the boundary Γ, either its normal component or its tangential component:

$$\begin{aligned}
\nabla \times \vec{A} &\quad \text{given in } \Omega, && (3.15)\\
\nabla \cdot \vec{A} &\quad \text{given in } \Omega, && (3.16)\\
\vec{A} \cdot \vec{n} &\quad \text{given on } \Gamma_1, && (3.17)\\
\vec{n} \times \vec{A} &\quad \text{given on } \Gamma_2 && (3.18)
\end{aligned}$$

where Ω is the global volume of the problem bounded by a surface Γ with two different parts as

$$\Gamma = \Gamma_1 \cup \Gamma_2. \tag{3.19}$$

Proof : Let $\vec{A_1}$ and $\vec{A_2}$ be two vector potentials which fulfil the conditions (3.15) - (3.18) above.

For the difference $\vec{A_0}$

$$\vec{A_0} = \vec{A_1} - \vec{A_2} \tag{3.20}$$

(3.15 - 3.18) read:

$$\begin{aligned}
\nabla \times \vec{A_0} &= 0 \quad \text{in } \Omega, && (3.21)\\
\nabla \cdot \vec{A_0} &= 0 \quad \text{in } \Omega, && (3.22)\\
\vec{A_0} \cdot \vec{n} &= 0 \quad \text{on } \Gamma_1, && (3.23)\\
\vec{n} \times \vec{A_0} &= 0 \quad \text{on } \Gamma_2. && (3.24)
\end{aligned}$$

Now, as it can be seen from Eq. (3.21) the vector potential $\vec{A}_0$ can be written in terms of a scalar function u_0 as

$$\vec{A}_0 = \nabla u_0. \tag{3.25}$$

Eq. (3.22) to Eq. (3.24) reduce to

$$\begin{aligned} \triangle u_0 &= 0 \quad \text{in } \Omega, && (3.26)\\ \nabla u_0 \cdot \vec{n} &= 0 \quad \text{on } \Gamma_1, && (3.27)\\ u_0 &= 0 \quad \text{on } \Gamma_2, && (3.28) \end{aligned}$$

i.e. the function u_0 is a harmonic function that fulfills a homogenous Dirichlet boundary condition on Γ_1 and a homogenous Neumann boundary condition on Γ_2.
Applying Green's first theorem

$$\int_\Omega (\nabla u \cdot \nabla v + u \triangle v)\, d\Omega = \int_\Gamma u \nabla v \cdot d\vec{\Gamma} \tag{3.29}$$

which is here stated without proof, the following identity for a harmonic function can be written as

$$\int_\Omega (\nabla u_0)^2\, d\Omega = -\int_\Omega (u_0 \triangle u_0)\, d\Omega + \int_\Gamma u_0 \nabla u_0 \cdot \vec{n}\, d\Gamma \tag{3.30}$$

where $\vec{n}$ is the outward normal on the boundary Γ.

According to Eq. (3.26) - Eq. (3.28) the right hand side of Eq. (3.30) vanishes and thus

$$\int_\Omega (\nabla)^2 u_0\, d\Omega \equiv 0 \tag{3.31}$$

only and only if

$$\nabla u_0 = 0. \tag{3.32}$$

Hence, since the conditions (3.15) to (3.18) are satisfied and

$$\vec{A}_0 = \vec{A}_1 - \vec{A}_2 = \nabla u_0 = 0 \tag{3.33}$$

the vector potential $\vec{A}$ is unique.

3.1.3 Coulomb gauging

As it was shown in the previous section, to make the vector potential $\vec{A}$ unique, it is necessary to define its divergence and, on the boundary Γ, either its normal component or its tangential

component. One of the commonest conditions is the Coulomb gauge where the divergence of $\vec{A}$ is set to zero as in

$$\nabla \cdot \vec{A} = 0. \tag{3.34}$$

The Equation (3.13) can be satisfied by setting the tangential component of $\vec{A}$ on Γ_B as

$$\vec{n} \times \vec{A} = \vec{\alpha}. \tag{3.35}$$

The function $\vec{\alpha}$ itself has to fulfil the equation

$$\nabla \cdot \vec{\alpha} = b_m \tag{3.36}$$

which is evident from the identity

$$\nabla \cdot (\vec{n} \times \vec{A}) = -\nabla \cdot (\vec{A} \times \vec{n}) = -\vec{n} \cdot (\nabla \times \vec{A}) = b_m. \tag{3.37}$$

Thus the choice of the tangential component implies as well the prescription of the fluxes of the section of Γ_H. Applying Stokes' Theorem to Eq. (3.14) gives

$$\oint_{\Gamma_H} \nabla \times \vec{A} \cdot \vec{n}\, d\Gamma = \oint_{C_{\psi_i}} \vec{A} \cdot\, d\vec{l} = \oint_{C_{\psi_i}} (\vec{n} \times \vec{A}) \times \vec{n} \cdot\, d\vec{l} \tag{3.38}$$

where C_{ψ_i} is the curve bounding the surface section Γ_{H_i} and therefore separates it from the section Γ_B. From Eq. (3.35) and Eq. (3.38) it follows that,

$$\oint_{C_{\psi_i}} (\vec{\alpha} \times \vec{n}) \cdot\, d\vec{l} = -\psi_i \tag{3.39}$$

must also be satisfied by $\vec{\alpha}$ in addition to Eq. (3.36). For the choice of the function $\vec{\alpha}$ no general guidelines can be given. It has in any case to satisfy Eq. (3.36) and (3.39). Besides, in a large number of magnetostatic problems the fictitious magnetic charge density b_m is zero and $n_H = 1$, so that there are no fluxes prescribed. This allows for $\vec{\alpha} = 0$ in the boundary condition in Eq. (3.35), i.e. the tangential component of the vector potential $\vec{A}$ can be chosen to be zero on Γ_B.
Since the tangential component of the vector potential $\vec{A}$ is specified on Γ_B which corresponds to Γ_2 in Eq. (3.18) it is obvious to specify its normal component on Γ_H corresponding to Γ_1 in Eq. (3.17). A way to do this is to introduce the additional boundary condition

$$\vec{A} \cdot \vec{n} = 0 \quad \text{on } \Gamma_H. \tag{3.40}$$

3.1.3.1 The complete $\vec{A}$-formulation

As a summary the differential equations and the boundary conditions describing a unique vector potential are collected here:

$$\begin{aligned}
\nabla \times \nu \nabla \times \vec{A} &= \vec{J} \quad \text{in } \Omega, && (3.41)\\
\nabla \cdot \vec{A} &= 0 \quad \text{in } \Omega, && (3.42)\\
\nu \nabla \times \vec{A} \times \vec{n} &= \vec{K} \quad \text{on } \Gamma_H, && (3.43)\\
\vec{A} \cdot \vec{n} &= 0 \quad \text{on } \Gamma_H, && (3.44)\\
\vec{n} \times \vec{A} &= \vec{\alpha} \quad \text{on } \Gamma_B. && (3.45)
\end{aligned}$$

In order to further deal with one differential equation only, an additional term [10] is introduced in Eq. (3.41) :

$$\nabla \times \nu \nabla \times \vec{A} - \nabla \nu \nabla \cdot \vec{A} = \vec{J} \quad \text{in } \Omega. \tag{3.46}$$

How to ensure that the function $(\nu \nabla \cdot \vec{A})$ is always identically zero, i.e. the Eq. (3.41) remains unchanged? The divergence of Eq. (3.46) yields

$$\triangle (\nu \nabla \cdot \vec{A}) = 0 \quad \text{in } \Omega. \tag{3.47}$$

Taking the normal component of Eq. (3.46) on the surface Γ_H gives

$$\vec{n} \cdot \nabla \times \nu \nabla \times \vec{A} - \frac{\partial}{\partial n}(\nu \nabla \cdot \vec{A}) = \vec{n} \cdot \vec{J} \quad \text{in } \Omega. \tag{3.48}$$

With the vector identity

$$\vec{n} \cdot \nabla \times \nu \nabla \times \vec{A} = \nabla \cdot (\nu \nabla \times \vec{A} \times \vec{n}) \tag{3.49}$$

Eq. (3.48) and the boundary condition (3.43) reduce to

$$\nabla \cdot \vec{K} - \vec{n} \cdot \vec{J} = \frac{\partial}{\partial n}(\nu \nabla \cdot \vec{A}) \quad \text{on } \Gamma_H. \tag{3.50}$$

The left hand side of Eq. (3.50) is zero because the sources of a surface current density $\vec{K}$ are always caused by a current density J_n

$$\frac{\partial}{\partial n}(\nu \nabla \cdot \vec{A}) = 0 \quad \text{on } \Gamma_H. \tag{3.51}$$

Thus, the function $\nu \nabla \cdot \vec{A}$ is a harmonic function which satisfies a Neumann boundary condition on Γ_H. Hence, the function $\nu \nabla \cdot \vec{A}$ must furthermore satisfy a homogenous Dirichlet boundary condition on Γ_B

$$\nu \nabla \cdot \vec{A} = 0 \tag{3.52}$$

in order to be zero in region Ω.
The complete $\vec{A}$-formulation with its differential equation and boundary conditions is summerised below:

$$\begin{aligned}
\nabla \times \nu \nabla \times \vec{A} - \nabla \nu \nabla \cdot \vec{A} &= \vec{J} \quad \text{in } \Omega, && (3.53)\\
\nu \nabla \times \vec{A} \times \vec{n} &= \vec{K} \quad \text{on } \Gamma_H, && (3.54)\\
\vec{A} \cdot \vec{n} &= 0 \quad \text{on } \Gamma_H, && (3.55)\\
\vec{n} \times \vec{A} &= \vec{\alpha} \quad \text{on } \Gamma_B, && (3.56)\\
\nu \nabla \cdot \vec{A} &= 0 \quad \text{on } \Gamma_B. && (3.57)
\end{aligned}$$

3.1.4 Ritz's method

3.1.4.1 Ritz's equations

In the static case a differential equation of the form

$$Lu = f \quad \text{in } \Omega \tag{3.58}$$

is to be solved where L is a second order elliptic differential operator (or the sum of such operators), u is the unknown function to be determined and f is the known forcing function. The boundary condition on Γ_D is of the form

$$u = u_0 \quad \text{on } \Gamma_D. \tag{3.59}$$

This kind of problem is equivalent to the variational problem

$$W^{(u)} = \frac{1}{2}\int_{\Omega} (u \cdot L\,u)\; d\Omega - \int_{\Omega} (u \cdot f)\; d\Omega \tag{3.60}$$

wherein the solution is out of a set of functions satisfying the boundary condition in Eq. (3.59).

The unknown function u is approximated by an expansion in terms of m elements of an entire function set $\{\vec{f}_i\}$:

$$u \approx u^{(n)} = u_D + \sum_{i=1}^{m} {a_i}^{(n)} \vec{f}_i \tag{3.61}$$

where the function u_D satisfies the inhomogenous Dirichlet boundary condition in Eq. (3.59) and the elements of the function set $\{\vec{f}_i\}$ satisfy homogenous Dirichlet boundary conditions as

$$f_i = 0 \quad \text{on } \Gamma_D. \tag{3.62}$$

In order to determine the coefficients ${a_i}^{(n)}$ the following set of partial differential equations has to be solved:

$$\frac{\partial W^{(u^{(n)})}}{\partial a_i} = 0 \quad \forall \quad \text{i=1,2,}\cdots\text{,m.} \tag{3.63}$$

Differentiating Eq. (3.60) yields

$$\begin{aligned}\frac{\partial W^{(u^{(n)})}}{\partial a_i} &= \frac{\partial}{\partial a_i}\left\{\frac{1}{2}\int_{\Omega}(u^{(n)} \cdot L\,u^{(n)})\,d\Omega - \int_{\Omega}(u^{(n)} \cdot f)\,d\Omega\right\} = \\ &= \frac{1}{2}\int_{\Omega}\left(\frac{\partial u^{(n)}}{\partial a_i} L u^{(n)}\right) d\Omega + \frac{1}{2}\int_{\Omega}\left(u^{(n)}\frac{\partial (L u^{(n)})}{\partial a_i}\right) d\Omega - \int_{\Omega}\left(\frac{\partial (u^{(n)})}{\partial a_i} f\right) d\Omega.\end{aligned} \tag{3.64}$$

Furthermore it can be shown from Eq. (3.61) that:

$$\frac{\partial u^{(n)}}{\partial a_i} = f_i, \tag{3.65}$$

$$\frac{\partial(Lu^{(n)})}{\partial a_i} = Lf_i. \tag{3.66}$$

Inserting these two results in Eq. (3.64) yields

$$\frac{\partial W_{(u^{(n)})}}{\partial a_i} = \frac{1}{2}\int_\Omega \left(f_i \cdot Lu^{(n)}\right) d\Omega + \frac{1}{2}\int_\Omega \left(u^{(n)} \cdot Lf_i\right) d\Omega - \int_\Omega (f_i \cdot f)\, d\Omega. \tag{3.67}$$

By assuming that the operator L is symmetric, the so-called Ritz equations are obtained:

$$\int_\Omega f_i \cdot \left(Lu^{(n)} - f\right) d\Omega = 0 \quad \forall \quad \text{i=1,2,}\cdots\text{,m.} \tag{3.68}$$

The above procedure is known in the literature as *Ritz's method.*

3.1.4.2 Symmetric operator for $\vec{A}$

By deriving Ritz's equations it was assumed that the differential operator L is symmetric. The differential equation (3.53) and the boundary conditions (3.54) and (3.57) can be brought together representing a general Laplacian differential operator:

$$\bigtriangledown\times\nu\bigtriangledown\times\vec{A} - \bigtriangledown\nu\,\bigtriangledown\cdot\vec{A} + \delta_{\Gamma_H}\nu\bigtriangledown\times\vec{A}\times\vec{n} + \delta_{\Gamma_B}\nu\bigtriangledown\cdot\vec{A}\,\vec{n} = \vec{J} + \delta_{\Gamma_H}\vec{K} \tag{3.69}$$

where δ_Γ is a general Dirac function reducing a volume integral to a surface integral on a surface Γ

$$\int_\Omega \delta_\Gamma\, w\, d\Omega = \oint_\Gamma w\, d\Gamma \tag{3.70}$$

for any arbitrary function w.
A differential operator as on the left hand side of Eq. (3.69) is symmetric if the vector potential $\vec{A}$ satisfies homogenous Dirichlet boundary conditions on the boundaries Γ_H and Γ_B. In order to work out the proof the following two Green identities will be used:

$$\int_\Omega \vec{A_1}\cdot(\bigtriangledown\times\nu\bigtriangledown\times\vec{A_2})d\Omega = \int_\Omega(\bigtriangledown\times\vec{A_1}\cdot\nu\bigtriangledown\times\vec{A_2})d\Omega - \oint_\Gamma \vec{n}\cdot(\vec{A_1}\times\nu\bigtriangledown\times\vec{A_2})\,d\Gamma \tag{3.71}$$

$$-\int_\Omega \vec{A_1}\cdot(\bigtriangledown\nu\bigtriangledown\cdot\vec{A_2})\,d\Omega = \int_\Omega(\bigtriangledown\cdot\vec{A_1}\,\nu\bigtriangledown\cdot\vec{A_2})\,d\Omega - \oint_\Gamma(\nu\bigtriangledown\cdot\vec{A_2})\vec{A_1}\cdot\vec{n}\,d\Gamma \tag{3.72}$$

Proof : Let $\vec{A_1}$ and $\vec{A_2}$ be two vector potentials of the same type as $\vec{A}$. The differential operator in terms of $\vec{A_1}$ is then:

$$\bigtriangledown\times\nu\bigtriangledown\times\vec{A_1} - \bigtriangledown\nu\,\bigtriangledown\cdot\vec{A_1} + \delta_{\Gamma_H}\nu\bigtriangledown\times\vec{A_1}\times\vec{n} + \delta_{\Gamma_B}\nu\bigtriangledown\cdot\vec{A_1}\,\vec{n} = \vec{J} + \delta_{\Gamma_H}\vec{K}. \tag{3.73}$$

Using $\vec{A}_2$ as weighting function, the Ritz equations are:

$$\int_\Omega \vec{A}_2 \cdot (\bigtriangledown \times \nu \bigtriangledown \times \vec{A}_1 - \bigtriangledown \nu \bigtriangledown \cdot \vec{A}_1) \, d\Omega + \int_\Omega \vec{A}_2 \cdot (\delta_{\Gamma_H} \nu \bigtriangledown \times \vec{A}_1 \times \vec{n} + \delta_{\Gamma_B} \nu \bigtriangledown \cdot \vec{A}_1 \, \vec{n}) \, d\Omega - \int_\Omega \vec{A}_2 \cdot (\vec{J} + \delta_{\Gamma_H} \vec{K}) \, d\Omega = 0. \tag{3.74}$$

Applying the Green identities (3.71) and (3.72) and investigating the differential operator only, gives:

$$\begin{aligned} &\int_\Omega \vec{A}_2 \cdot (\bigtriangledown \times \nu \bigtriangledown \times \vec{A}_1 - \bigtriangledown \nu \bigtriangledown \cdot \vec{A}_1) \, d\Omega + \\ &\int_\Omega \vec{A}_2 \cdot (\delta_{\Gamma_H} \nu \bigtriangledown \times \vec{A}_1 \times \vec{n} + \delta_{\Gamma_B} \nu \bigtriangledown \cdot \vec{A}_1 \, \vec{n}) \, d\Omega = \\ &\int_\Omega (\bigtriangledown \times \vec{A}_1 \cdot \nu \bigtriangledown \times \vec{A}_2) \, d\Omega + \int_\Omega (\bigtriangledown \cdot \vec{A}_1 \, \nu \bigtriangledown \cdot \vec{A}_2) \, d\Omega - \\ &\oint_\Gamma \vec{n} \cdot (\vec{A}_1 \times \nu \bigtriangledown \times \vec{A}_2) \, d\Gamma + \oint_{\Gamma_H} \vec{n} \cdot (\vec{A}_1 \times \nu \bigtriangledown \times \vec{A}_2) \, d\Gamma - \\ &\oint_\Gamma (\nu \bigtriangledown \cdot \vec{A}_2) \vec{A}_1 \cdot \vec{n} \, d\Gamma + \oint_{\Gamma_B} (\nu \bigtriangledown \cdot \vec{A}_2) \vec{A}_1 \cdot \vec{n} \, d\Gamma. \end{aligned} \tag{3.75}$$

It is clear that the surface integrals on Γ can be taken apart into pieces on Γ_H and Γ_B. Now, both surface integrals appear twice but with negative sign, therefore leaving us with

$$\begin{aligned} &\int_\Omega \vec{A}_2 \cdot (\bigtriangledown \times \nu \bigtriangledown \times \vec{A}_1 - \bigtriangledown \nu \bigtriangledown \cdot \vec{A}_1) \, d\Omega + \\ &\int_\Omega \vec{A}_2 \cdot (\delta_{\Gamma_H} \nu \bigtriangledown \times \vec{A}_1 \times \vec{n} + \delta_{\Gamma_B} \nu \bigtriangledown \cdot \vec{A}_1 \, \vec{n}) \, d\Omega = \\ &\int_\Omega (\bigtriangledown \times \vec{A}_1 \cdot \nu \bigtriangledown \times \vec{A}_2) \, d\Omega + \int_\Omega (\bigtriangledown \cdot \vec{A}_1 \, \nu \bigtriangledown \cdot \vec{A}_2) \, d\Omega - \\ &\oint_{\Gamma_B} (\vec{n} \times \vec{A}_1 \cdot \nu \bigtriangledown \times \vec{A}_2) \, d\Gamma - \oint_{\Gamma_H} \vec{A}_1 \cdot \vec{n} (\nu \bigtriangledown \cdot \vec{A}_2) \, d\Gamma. \end{aligned} \tag{3.76}$$

Since the vector potential satisfies the homogenous Dirichlet boundary conditions; the right

hand side of Eq. (3.76) reduces to

$$\int_\Omega \vec{A}_2 \cdot (\nabla\times\nu\nabla\times\vec{A}_1 - \nabla\nu\,\nabla\cdot\vec{A}_1)\,d\Omega + \int_\Omega \vec{A}_2 \cdot (\delta_{\Gamma_H}\nu\nabla\times\vec{A}_1\times\vec{n} + \delta_{\Gamma_B}\nu\nabla\cdot\vec{A}_1\,\vec{n})\,d\Omega = \int_\Omega (\nabla\times\vec{A}_1\cdot\nu\,\nabla\times\vec{A}_2 + \nabla\cdot\vec{A}_1\,\nu\,\nabla\cdot\vec{A}_2)\,d\Omega. \tag{3.77}$$

The functions $\vec{A}_1$ and $\vec{A}_2$ have the same properties thus they are exchangeable. Hence, the differential operator in (3.69) is symmetric. Furthermore, this operator is positive which can be shown by setting

$$\vec{A}_1 = \vec{A}_2 = \vec{A}. \tag{3.78}$$

The right hand side of Eq. (3.77) becomes therefore

$$\int_\Omega \vec{A}\cdot(\nabla\times\nu\nabla\times\vec{A} - \nabla\nu\,\nabla\cdot\vec{A})\,d\Omega + \int_\Omega \vec{A}\cdot(\delta_{\Gamma_H}\nu\nabla\times\vec{A}\times\vec{n} + \delta_{\Gamma_B}\nu\nabla\cdot\vec{A}\,\vec{n})\,d\Omega = \int_\Omega \nu\{(\nabla\times\vec{A})^2 + (\nabla\cdot\vec{A})^2\}\,d\Omega \tag{3.79}$$

which is always bigger or equal zero.

3.1.5 The Finite Element Method

The Finite Element Method is based on a division of the studied region Ω into small subregions, so called, finite elements. The potential functions are approximated by low order polynomials within each finite element. Elements of various shapes are in current use, triangles and quadrilaterals being the most popular ones in the two-dimensional case. The elements are defined by means of nodes as it is shown in Fig. (3.2). Special interpolation polynomials, called element shape functions are used for the approximation of the potentials within each element. One element shape function $f_k^{(e)}$ is associated with each node in an element; it assumes the value 1 at this node and is zero at all other nodes:

$$f_k^{(e)} = \begin{cases} 1 \text{ at the node k,} \\ 0 \text{ at other nodes.} \end{cases} \tag{3.80}$$

The element shape functions are conveniently defined in a local coordinate system associated with each element. The two dimensional, eight-noded, rectangular element is shown in the local as well as in the global coordinate system in Fig. (3.3). The element shape functions

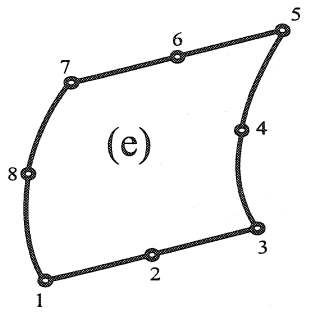

Figure 3.2: Eight-noded, rectangular element

can be written

for corner nodes ($\eta_k = \pm 1$, $\xi_k = \pm 1$):

$$f_k^{(e)}(\xi,\eta) = \frac{1}{4}(1+\xi\,\xi_k)(1+\eta\,\eta_k)(\xi\,\xi_k+\eta\,\eta_k-1), \tag{3.81}$$

for mid-side nodes ($\xi_k = 0$, $\eta_k = \pm 1$):

$$f_k^{(e)}(\xi,\eta) = \frac{1}{2}(1-\xi^2)(1+\eta\,\eta_k) \tag{3.82}$$

and for mid-side nodes ($\eta_k = 0$, $\xi_k = \pm 1$):

$$f_k^{(e)}(\xi,\eta) = \frac{1}{2}(1-\eta^2)(1+\xi\,\xi_k) \tag{3.83}$$

where (ξ_k, η_k) are the local coordinates of the node k. Two of the shape functions represented by Eq. (3.81) - (3.83) are shown in Fig. (3.4). They are quadratic polynomials and are easily seen to satisfy the conditions (3.81), (3.82) and (3.83).

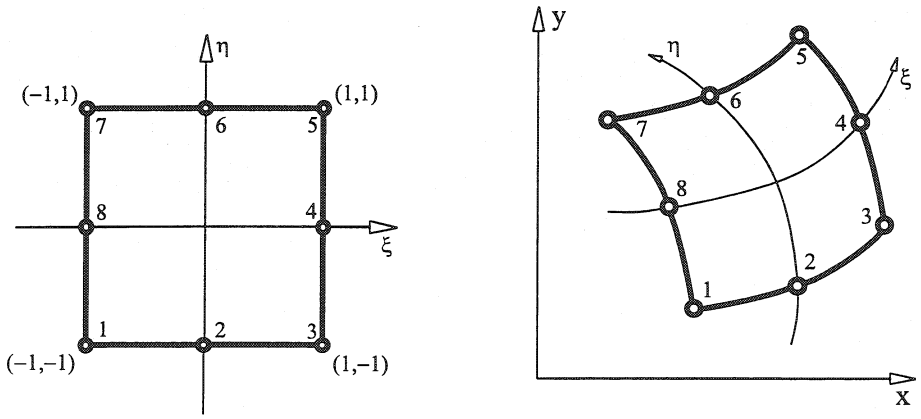

Figure 3.3: The local and global coordinate system

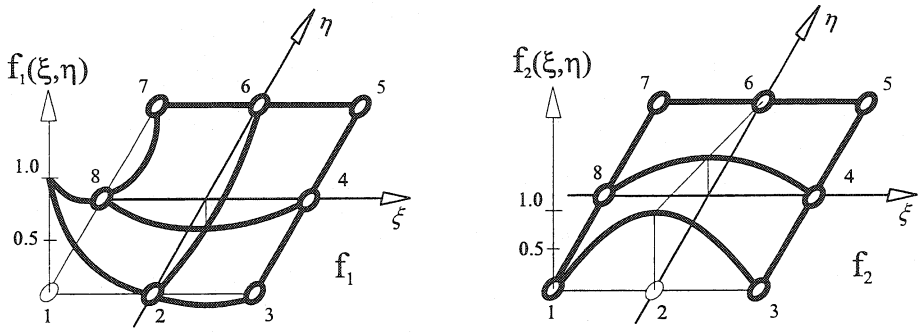

Figure 3.4: The element shape functions for node one and two

A transformation between the local and global coordinates of an element with $n_n^{(e)}$ nodes can be defined by means of the locally defined shape functions:

$$\begin{aligned} x(\xi,\eta) &= \sum_{k=1}^{n_n^{(e)}} x_k f_k^{(e)}(\xi,\eta), \\ y(\xi,\eta) &= \sum_{k=1}^{n_n^{(e)}} y_k f_k^{(e)}(\xi,\eta) \end{aligned} \tag{3.84}$$

where (x_k, y_k) are the global coordinates of the k-th node. Evidently, the local coordinates of the nodes are transformed into their global coordinates in view of the property (3.80) of the element shape functions. This transformation also defines the element shape functions in terms of the global coordinates x and y.
The function approximating the potential function can be written in an element as

$$u^{(e)}(x,y) = \sum_{k=1}^{n_n^{(e)}} u_k f_k^{(e)}(x,y), \tag{3.85}$$

where u_k is the value of the potential in the node k. Indeed, the condition (3.80) ensures that the function $u^{(e)}$ yields the value at the k-th node.
The division of the region Ω into finite elements defines a global set of nodes where the nodes of the neighbouring elements coincide. One global shape function f_k can be associated with each global node by defining it to be equal to the relevant element shape function in each element containing this global node and to be zero in all other elements. These global shape functions are hence continuous not only within the elements but also on the element boundaries. They satisfy the condition (3.80), i.e. they equal unity at the corresponding global node and are zero at all other nodes. Therefore, they allow an approximation of a potential function u in the region Ω in terms of its nodal values u_k:

$$u \approx u^{(n)}(x,y) = \sum_{k=1}^{n_n} u_k f_k(x,y) \tag{3.86}$$

where n_n is the number of global nodes.
The global shape functions can serve as expansion functions in the approximation of the potentials in Ritz's method. They can also be used in a straightforward manner for the construction of functions satisfying the Dirichlet boundary conditions [7].

3.1.6 The $\vec{A}_r$-formulation

3.1.6.1 The elementary model problem

For deriving the field equations in terms of a reduced vector potential $\vec{A}_r$ it is convenient to consider the elementary model problem (e.m.p.) for the magnetostatic case. The e.m.p. shown in Fig. (3.5) may consist of two different volumes Ω_i and Ω_a where Ω_i is the iron region with the permeability μ or the reluctivity ν and the air region Ω_a with the permeability μ_0 or reluctivity ν_0 of vacuum. The regions are connected to each other at the interface Γ_{ai}. Furthermore, each volume is bounded by a surface Γ_j consisting itself of two different disjunct parts Γ_H and Γ_B and where $\vec{n}$ is the outward normal. The global boundary of the e.m.p. can now be written as

$$\Gamma = \Gamma_{H_i} \cup \Gamma_{H_a} \cup \Gamma_{B_i} \cup \Gamma_{B_a}. \tag{3.87}$$

The non conductive air region Ω_a may also contain a certain number of conductor sources $\vec{J}_s$ which do not intersect the iron region Ω_i.

3.1.6.2 Reduced vector potential $\vec{A}_r$

The vector potential $\vec{A}$ is split into parts as

$$\vec{A} = \vec{A}_s + \vec{A}_r \tag{3.88}$$

where $\vec{A}_r$ is the reduced vector potential due to the magnetisation and $\vec{A}_s$ is the impressed vector potential due to the source currents in free space. The relationship between the impressed vector potential $\vec{A}_s$ and the field vector $\vec{H}_s$ is,

$$\nabla \times \vec{A}_s = \mu_0 \vec{H}_s \tag{3.89}$$

and by definition for conductor source regions with current density $\vec{J}_s$ the field vector $\vec{H}_s$ is given by

$$\vec{H}_s = \frac{1}{4\pi} \int_{\Omega} \vec{J}_s \times \nabla(\frac{1}{R})\, d\Omega \tag{3.90}$$

where $R = \mid r_q - r_a \mid$ is the distance from the source point r_q to the field point r_a, Eq. (3.90) is known as the Biot Savart Law [11].

3.1.6.3 Field equations in terms of $\vec{A}_r$

In this section the field equations in terms of a reduced vector potential $\vec{A}_r$ for both the iron region Ω_i and the air region Ω_a are worked out. As it can be seen in Fig. (3.5) the current density $\vec{J}$ in Ω_i is by definition set to zero. Thus Eq. (3.53) reduces to

$$\nabla \times \nu \nabla \times \vec{A} - \nabla \nu \nabla \cdot \vec{A} = 0 \quad \text{in } \Omega_i. \tag{3.91}$$

Applying Eq. (3.88) gives

$$\nabla \times \nu \nabla \times (\vec{A}_{r_i} + \vec{A}_s) - \nabla \nu \nabla \cdot \vec{A}_{r_i} = 0 \quad \text{in } \Omega_i. \tag{3.92}$$

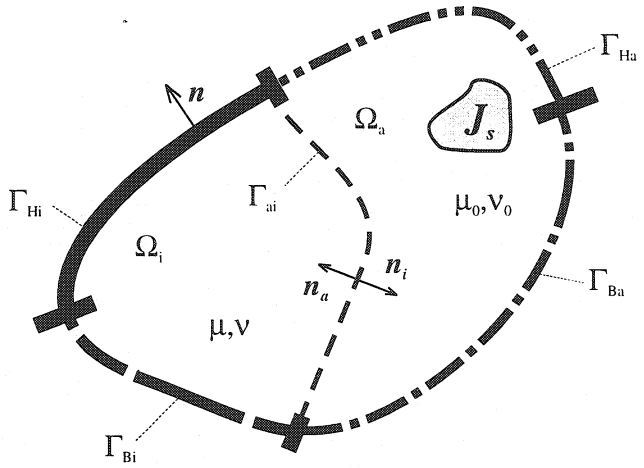

Figure 3.5: The elementary model problem for $\vec{A}_r$

Rearranging Eq. (3.92), i.e. transferring the known quantities to the right hand side of the equation leads to

$$\nabla \times \nu \nabla \times \vec{A_{r_i}} - \nabla \nu \nabla \cdot \vec{A_{r_i}} = -\nabla \times \nu \nabla \times \vec{A_s} \quad \text{in } \Omega_i. \tag{3.93}$$

For the air region Ω_a the procedure is straightforward. The differential equation can be written as

$$\nabla \times \nu_0 \nabla \times (\vec{A_{r_a}} + \vec{A_s}) - \nabla \nu_0 \nabla \cdot \vec{A_{r_a}} = \vec{J_s} \quad \text{in } \Omega_a. \tag{3.94}$$

Taking the curl of Eq. (3.89) gives

$$\nabla \times \nu_0 \nabla \times \vec{A_s} = \nabla \times \vec{H_s}, \tag{3.95}$$

which is obviously representing the current density $\vec{J_s}$. Thus, the differential equation is

$$\nabla \times \nu_0 \nabla \times (\vec{A_{r_a}} + \vec{A_s}) - \nabla \nu_0 \nabla \cdot \vec{A_{r_a}} = \nabla \times \nu_0 \nabla \times \vec{A_s} \quad \text{in } \Omega_a. \tag{3.96}$$

As it can be seen in Eq. (3.96) the curl-curl expression of the impressed vector potential $\vec{A_s}$ appears once on the left hand side of the equation and on the right hand side as well and thus cancels out. The differential equation therefore reduces to

$$\nabla \times \nu_0 \nabla \times \vec{A_{r_a}} - \nabla \nu_0 \nabla \cdot \vec{A_{r_a}} = 0 \quad \text{in } \Omega_a. \tag{3.97}$$

The impressed vector potential $\vec{A_s}$ is assumed to satisfy the boundary conditions (3.54) - (3.57). In fact, this may not be exact on the far field boundaries. Since the field is assumed to be negligible there, this can be accepted. Hence, the same boundary conditions are valid for the reduced vector potential $\vec{A_r}$. On the interface Γ_{ai} between Ω_i and Ω_a interface conditions have to be satisfied:

$$\vec{B_i} \cdot \vec{n_i} + \vec{B_a} \cdot \vec{n_a} = 0 \quad \text{on } \Gamma_{ai}, \tag{3.98}$$

$$\vec{H_i} \times \vec{n_i} + \vec{H_a} \times \vec{n_a} = 0 \quad \text{on } \Gamma_{ai} \tag{3.99}$$

where $\vec{n_i}$ and $\vec{n_a}$ are the outer normals associated with the respective subregions. The normal component of the magnetic flux density B_n is continuous due to the chosen shape functions. For the tangential component of the magnetic field intensity the Eq. (3.99) written in terms of the reduced vector potential is:

$$(\nu_0 \bigtriangledown \times \vec{A_{r_a}} + \nu_0 \bigtriangledown \times \vec{A_s}) \times \vec{n_a} + (\nu \bigtriangledown \times \vec{A_{r_i}} + \nu \bigtriangledown \times \vec{A_s}) \times \vec{n_i} = 0 \quad \text{on } \Gamma_{ai}. \tag{3.100}$$

At this stage it is sufficient to state the complete $\vec{A_r}$-formulation where the surface current density $\vec{K}$ and the fictitious magnetic charge density b_m are assumed to be zero:

$$\bigtriangledown \times \nu \bigtriangledown \times \vec{A_{r_i}} - \bigtriangledown \nu \bigtriangledown \cdot \vec{A_{r_i}} = -\bigtriangledown \times \nu \bigtriangledown \times \vec{A_s} \quad \text{in } \Omega_i, \tag{3.101}$$

$$\bigtriangledown \times \nu_0 \bigtriangledown \times \vec{A_{r_a}} - \bigtriangledown \nu_0 \bigtriangledown \cdot \vec{A_{r_a}} = 0 \quad \text{in } \Omega_a, \tag{3.102}$$

$$\nu \bigtriangledown \times \vec{A_{r_i}} \times \vec{n} = 0 \quad \text{on } \Gamma_{H_i}, \tag{3.103}$$

$$\vec{A_{r_i}} \cdot \vec{n} = 0 \quad \text{on } \Gamma_{H_i}, \tag{3.104}$$

$$\vec{n} \times \vec{A_{r_i}} = 0 \quad \text{on } \Gamma_{B_i}, \tag{3.105}$$

$$\nu \bigtriangledown \cdot \vec{A_{r_i}} = 0 \quad \text{on } \Gamma_{B_i}, \tag{3.106}$$

$$\nu_0 \bigtriangledown \times \vec{A_{r_a}} \times \vec{n} = 0 \quad \text{on } \Gamma_{H_a}, \tag{3.107}$$

$$\vec{A_{r_a}} \cdot \vec{n} = 0 \quad \text{on } \Gamma_{H_a}, \tag{3.108}$$

$$\vec{n} \times \vec{A_{r_a}} = 0 \quad \text{on } \Gamma_{B_a}, \tag{3.109}$$

$$\nu_0 \bigtriangledown \cdot \vec{A_{r_a}} = 0 \quad \text{on } \Gamma_{B_a}, \tag{3.110}$$

and along the interface Γ_{ai}

$$(\nu_0 \bigtriangledown \times \vec{A_{r_a}} + \nu_0 \bigtriangledown \times \vec{A_s}) \times \vec{n_a} + (\nu \bigtriangledown \times \vec{A_{r_i}} + \nu \bigtriangledown \times \vec{A_s}) \times \vec{n_i} = 0 \quad \text{on } \Gamma_{ai}. \tag{3.111}$$

3.1.6.4 Ritz's equations

Similarly to the total vector potential formulation in section (3.1.4.2) the differential equations (3.101), (3.102) and the boundary conditions (3.103) - (3.110) can be brought together forming a generalized Laplacian operator. In the particular case of the reduced vector potential, the following operators for the regions Ω_i and Ω_a are found:

$$\begin{aligned} \bigtriangledown \times \nu \bigtriangledown \times \vec{A_{r_i}} - \bigtriangledown \nu \bigtriangledown \cdot \vec{A_{r_i}} + \\ \delta_{\Gamma_{H_i}} \nu \bigtriangledown \times \vec{A_{r_i}} \times \vec{n} + \delta_{\Gamma_{B_i}} \nu \bigtriangledown \cdot \vec{A_{r_i}} \vec{n} + \\ \delta_{\Gamma_{ai}} \{(\nu \bigtriangledown \times \vec{A_{r_i}} + \nu \bigtriangledown \times \vec{A_s}) \times \vec{n_i}\} + \\ \delta_{\Gamma_{ai}} \{(\nu_0 \bigtriangledown \times \vec{A_{r_a}} + \nu_0 \bigtriangledown \times \vec{A_s}) \times \vec{n_a}\} = -\bigtriangledown \times \nu \bigtriangledown \times \vec{A_s} \end{aligned} \tag{3.112}$$

in Ω_i and

$$\begin{aligned} \bigtriangledown \times \nu_0 \bigtriangledown \times \vec{A_{r_a}} - \bigtriangledown \nu \bigtriangledown \cdot \vec{A_{r_a}} + \\ \delta_{\Gamma_{H_a}} \nu_0 \bigtriangledown \times \vec{A_{r_a}} \times \vec{n} + \delta_{\Gamma_{B_a}} \nu_0 \bigtriangledown \cdot \vec{A_{r_a}} \vec{n} + \\ \delta_{\Gamma_{ai}} \{(\nu_0 \bigtriangledown \times \vec{A_{r_a}} + \nu_0 \bigtriangledown \times \vec{A_s}) \times \vec{n_a}\} + \\ \delta_{\Gamma_{ai}} \{(\nu_0 \bigtriangledown \times \vec{A_{r_i}} + \nu_0 \bigtriangledown \times \vec{A_s}) \times \vec{n_i}\} = 0 \end{aligned} \tag{3.113}$$

in Ω_a.
These operators are both symmetric and positive. The proof is similar to that in section (3.1.4.2).
Applying Ritz's method and approximating the vector potential as

$$\vec{A}_r \approx \vec{A_r}^n = \vec{A_{r_D}} + \sum_{k=1}^{m} A_{r_k} \vec{f}_k. \tag{3.114}$$

Ritz's equations are:

$$\begin{aligned}
&\int_{\Omega_i} \vec{f}_j \cdot (\nabla \times \nu \nabla \times \vec{A_{r_i}}^n - \nabla \nu \nabla \cdot \vec{A_{r_i}}^n)\, d\Omega + \\
&\int_{\Gamma_{H_i}} \vec{f}_j \cdot (\nu \nabla \times \vec{A_{r_i}}^n \times \vec{n})\, d\Gamma + \int_{\Gamma_{B_i}} (\nu \nabla \cdot \vec{A_{r_i}}^n)\, \vec{n} \cdot \vec{f}_j\, d\Gamma + \\
&\int_{\Gamma_{ai}} \vec{f}_j \cdot \{(\nu \nabla \times \vec{A_{r_i}}^n + \nu \nabla \times \vec{A}_s) \times \vec{n_i}\}\, d\Gamma + \\
&\int_{\Gamma_{ai}} \vec{f}_j \cdot \{(\nu_0 \nabla \times \vec{A_{r_a}}^n + \nu_0 \nabla \times \vec{A}_s) \times \vec{n_a}\}\, d\Gamma \\
&= -\int_{\Omega_i} \vec{f}_j \cdot (\nabla \times \nu \nabla \times \vec{A}_s)\, d\Omega
\end{aligned} \tag{3.115}$$

in Ω_i and

$$\begin{aligned}
&\int_{\Omega_a} \vec{f}_j \cdot (\nabla \times \nu_0 \nabla \times \vec{A_{r_a}}^n - \nabla \nu_0 \nabla \cdot \vec{A_{r_a}}^n)\, d\Omega + \\
&\int_{\Gamma_{Ha}} \vec{f}_j \cdot (\nu_0 \nabla \times \vec{A_{r_a}}^n \times \vec{n})\, d\Gamma + \int_{\Gamma_{Ba}} (\nu_0 \nabla \cdot \vec{A_{r_a}}^n)\, \vec{n} \cdot \vec{f}_j\, d\Gamma + \\
&\int_{\Gamma_{ai}} \vec{f}_j \cdot \{(\nu_0 \nabla \times \vec{A_{r_a}}^n + \nu_0 \nabla \times \vec{A}_s) \times \vec{n_a}\}\, d\Gamma + \\
&\int_{\Gamma_{ai}} \vec{f}_j \cdot \{(\nu \nabla \times \vec{A_{r_i}}^n + \nu \nabla \times \vec{A}_s) \times \vec{n_i}\}\, d\Gamma = 0
\end{aligned} \tag{3.116}$$

in Ω_a for all $j = 1, \cdots, n$.

The vector functions $\vec{f}_k$ must satisfy the homogeneous Dirichlet boundary conditions

$$\vec{n} \times \vec{f}_k = 0 \quad \text{on } \Gamma_B, \tag{3.117}$$

$$\vec{n} \cdot \vec{f}_k = 0 \quad \text{on } \Gamma_H, \tag{3.118}$$

and the function $\vec{A_{r_D}}$ the Dirichlet boundary conditions

$$\vec{n} \times \vec{A_{r_D}} = \vec{\alpha} \quad \text{on } \Gamma_B, \tag{3.119}$$

$$\vec{A_{r_D}} \cdot \vec{n} = 0 \quad \text{on } \Gamma_H. \tag{3.120}$$

With the following two Green identities

$$\int_\Omega \vec{f} \cdot (\bigtriangledown \times \nu \bigtriangledown \times \vec{A_r})\, d\Omega = \int_\Omega (\bigtriangledown \times \vec{f} \cdot \nu \bigtriangledown \times \vec{A_r})\, d\Omega - \oint_\Gamma \vec{f} \cdot (\nu \bigtriangledown \times \vec{A_r} \times \vec{n})\, d\Gamma \tag{3.121}$$

$$-\int_\Omega \vec{f} \cdot (\bigtriangledown \nu \bigtriangledown \cdot \vec{A_r})\, d\Omega = \int_\Omega (\bigtriangledown \cdot \vec{f}\, \nu \bigtriangledown \cdot \vec{A_r})\, d\Omega - \oint_\Gamma (\nu \bigtriangledown \cdot \vec{A_r})\, \vec{n} \cdot \vec{f}\, d\Gamma \tag{3.122}$$

these equations can be rewritten as:

$$\begin{aligned}
&\int_{\Omega_i} (\bigtriangledown \times \vec{f_j} \cdot \nu \bigtriangledown \times \vec{A_{r_i}^n})\, d\Omega - \oint_{\Gamma_i} \vec{f_j} \cdot (\nu \bigtriangledown \times \vec{A_{r_i}^n} \times \vec{n})\, d\Gamma + \\
&\int_{\Omega_i} (\bigtriangledown \cdot \vec{f_j}\, \nu \bigtriangledown \cdot \vec{A_{r_i}^n})\, d\Omega - \oint_{\Gamma_i} (\nu \bigtriangledown \cdot \vec{A_{r_i}^n}) \vec{n} \cdot \vec{f_j}\, d\Gamma + \\
&\int_{\Gamma_{H_i}} \vec{f_j} \cdot (\nu \bigtriangledown \times \vec{A_{r_i}^n} \times \vec{n})\, d\Gamma + \int_{\Gamma_{B_i}} (\nu \bigtriangledown \cdot \vec{A_{r_i}^n})\, \vec{n} \cdot \vec{f_j}\, d\Gamma + \\
&\int_{\Gamma_{ai}} \vec{f_j} \cdot \{(\nu \bigtriangledown \times \vec{A_{r_i}^n} + \nu \bigtriangledown \times \vec{A_s}) \times \vec{n_i}\}\, d\Gamma + \\
&\int_{\Gamma_{ai}} \vec{f_j} \cdot \{(\nu_0 \bigtriangledown \times \vec{A_{r_a}^n} + \nu_0 \bigtriangledown \times \vec{A_s}) \times \vec{n_a}\}\, d\Gamma \\
&= -\int_{\Omega_i} (\bigtriangledown \times \vec{f_j} \cdot \nu \bigtriangledown \times \vec{A_s})\, d\Omega + \oint_{\Gamma_i} \vec{f_j} \cdot (\nu \bigtriangledown \times \vec{A_s} \times \vec{n})\, d\Gamma
\end{aligned} \tag{3.123}$$

for the region Ω_i and

$$\int_{\Omega_a}(\bigtriangledown \times \vec{f_j} \cdot \nu_0 \bigtriangledown \times \vec{A_{r_a}^n})\, d\Omega - \oint_{\Gamma_a} \vec{f_j} \cdot (\nu_0 \bigtriangledown \times \vec{A_{r_a}^n} \times \vec{n})\, d\Gamma +$$
$$\int_{\Omega_a}(\bigtriangledown \cdot \vec{f_j}\, \nu_0 \bigtriangledown \cdot \vec{A_{r_a}^n})\, d\Omega - \oint_{\Gamma_a} (\nu_0 \bigtriangledown \cdot \vec{A_{r_a}^n})\, \vec{n} \cdot \vec{f_j}\, d\Gamma +$$
$$\int_{\Gamma_{Ha}} \vec{f_j} \cdot (\nu_0 \bigtriangledown \times \vec{A_{r_a}^n} \times \vec{n})\, d\Gamma + \int_{\Gamma_{Ba}} (\nu_0 \bigtriangledown \cdot \vec{A_{r_a}^n})\, \vec{n} \cdot \vec{f_j}\, d\Gamma +$$
$$\int_{\Gamma_{ai}} \vec{f_j} \cdot \{(\nu_0 \bigtriangledown \times \vec{A_{r_a}^n} + \nu_0 \bigtriangledown \times \vec{A_s}) \times \vec{n_a}\}\, d\Gamma +$$
$$\int_{\Gamma_{ai}} \vec{f_j} \cdot \{(\nu \bigtriangledown \times \vec{A_{r_i}^n} + \nu \bigtriangledown \times \vec{A_s}) \times \vec{n_i}\}\, d\Gamma = 0 \qquad (3.124)$$

for the region Ω_a. As a matter of fact, several surface integrals appear twice with different signs and therefore cancel out. Furthermore, applying the conditions (3.117) and (3.118) the equations reduce to:

$$\int_{\Omega_i}\{\bigtriangledown \times \vec{f_j} \cdot \nu \bigtriangledown \times \vec{A_{r_i}^n} + \bigtriangledown \cdot \vec{f_j}\, \nu \bigtriangledown \cdot \vec{A_{r_i}^n}\}\, d\Omega +$$
$$\int_{\Gamma_{ai}} \vec{f_j} \cdot \{\, (\nu_0 \bigtriangledown \times \vec{A_{r_a}^n} + \nu_0 \bigtriangledown \times \vec{A_s}) \times \vec{n_a}\, \}\, d\Gamma +$$
$$= - \int_{\Omega_i} (\bigtriangledown \times \vec{f_j} \cdot \nu \bigtriangledown \times \vec{A_s})\, d\Omega \qquad (3.125)$$

in Ω_i and

$$\int_{\Omega_a}(\bigtriangledown \times \vec{f_j} \cdot \nu_0 \bigtriangledown \times \vec{A_{r_a}^n} + \bigtriangledown \cdot \vec{f_j}\, \nu_0 \bigtriangledown \cdot \vec{A_{r_a}^n})\, d\Omega +$$
$$\int_{\Gamma_{ai}} \vec{f_j} \cdot (\nu_0 \bigtriangledown \times \vec{A_s} \times \vec{n_a})\, d\Gamma +$$
$$\int_{\Gamma_{ai}} \{(\nu \bigtriangledown \times \vec{A_{r_i}^n} + \nu \bigtriangledown \times \vec{A_s}) \times \vec{n_i}\, \}\, d\Gamma = 0 \qquad (3.126)$$

in Ω_a. Due to the interface condition (3.111) and keeping in mind that $\vec{n_i} = -\vec{n_a}$ the Eq. (3.35) can be reformulated as

$$\int_{\Omega_i}\{\bigtriangledown \times \vec{f_j} \cdot \nu_0 \bigtriangledown \times \vec{A_{r_a}^n} + \bigtriangledown \cdot \vec{f_j}\, \nu_0 \bigtriangledown \cdot \vec{A_{r_a}^n}\}\, d\Omega -$$
$$\int_{\Gamma_{ai}} \vec{f_j} \cdot \{\, \nu_0 \bigtriangledown \times \vec{A_{r_a}^n} \times \vec{n_a}\, \}\, d\Gamma = 0 \qquad (3.127)$$

in Ω_i.

Finally, by adding Eq. (3.126) and Eq. (3.127) Ritz's equations for $\Omega = \Omega_i \cup \Omega_a$ have the following form:

$$\int_{\Omega_i} \{\nabla \times \vec{f}_j \cdot \nu \nabla \times \vec{A}_{r_i}^n + \nabla \cdot \vec{f}_j \, \nu \nabla \cdot \vec{A}_{r_i}^n\} \, d\Omega +$$

$$\int_{\Omega_a} \{\nabla \times \vec{f}_j \cdot \nu_0 \nabla \times \vec{A}_{r_a}^n + \nabla \cdot \vec{f}_j \, \nu_0 \nabla \cdot \vec{A}_{r_a}^n\} \, d\Omega$$

$$= -\int_{\Omega_i} (\nabla \times \vec{f}_j \cdot \nu \nabla \times \vec{A}_s) \, d\Omega + \int_{\Gamma_{ai}} \vec{f}_j \cdot \{\nu_0 \nabla \times \vec{A}_s \times \vec{n}_i\} \, d\Gamma. \tag{3.128}$$

3.1.6.5 Numerical implementation

The numerical implementation of the $\vec{A}_r$-formulation for the 2d-case much simplifies. The vector potential has just a component in z-direction and can therefore be treated as a scalar potential [7]. A gauging procedure, as described in section (3.1.2), is not necessary. Equation (3.128) thus further reduces to:

$$\int_{\Omega_i} (\nabla \times \vec{f}_j \cdot \nu \nabla \times \vec{A}_{r_i}^n) \, d\Omega + \int_{\Omega_a} (\nabla \times \vec{f}_j \cdot \nu_0 \nabla \times \vec{A}_{r_a}^n) \, d\Omega$$

$$= -\int_{\Omega_i} (\nabla \times \vec{f}_j \cdot \nu \nabla \times \vec{A}_s) \, d\Omega + \int_{\Gamma_{ai}} \vec{f}_j \cdot \{\nu_0 \nabla \times \vec{A}_s \times \vec{n}_i\} \, d\Gamma. \tag{3.129}$$

The full vector form of Eq. (3.128) is not appropriate for the numerical implementation. The set of the global shape functions is defined to be continuous in the entire region $\Omega = \Omega_i \cup \Omega_a$. The solution $\vec{A}_r$ as well as the function $\nabla \cdot \vec{A}_r$ are therefore continuous. Because of jumping material properties the function $\nu \nabla \cdot \vec{A}_r$ is by far not continuous. This causes convergence problems in solving the equation system of Eq. (3.128). To eliminate these kind of problems a new FE-formulation based on edge-elements was developed. The formulation is worked out in detail in chapter (5).

Chapter 4

Numerical Investigations in 2D

4.1 Comparison to FE-codes based on a $\vec{A}$-formulation

A simple test case shown in Fig. (4.1) was created to evaluate the results gained by the $\vec{A}_r$-formulation. The analytical solution of the linear problem by means of the method of image currents [17] is taken for ease of reference. The solution was further investigated and compared to results calculated by several commercially available FE-codes frequently applied to the integrated magnet design at CERN. All of these classical FE-codes (ANSYS, FEM2D, OPERA, and POISSON) are based on a total vector potential $\vec{A}$-formulation.

4.1.1 Simple dipole magnet

The coil used for the study is a simple one-layer design with three blocks, as proposed for the D1 magnets [1]. The yoke was chosen to allow the results, calculated by the method of image currents, to be used for reference, i.e. a hollow iron yoke with a collar radius of r=75mm and with a yoke radius of r=180mm.

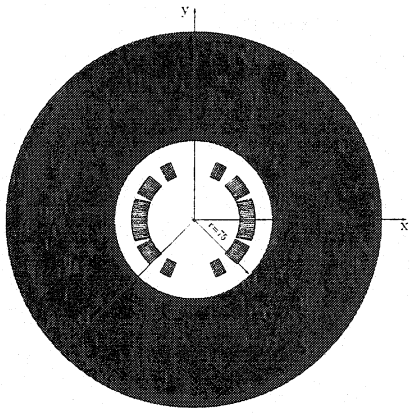

Figure 4.1: Simple dipole magnet

ANSYS and FEM2D are FE-codes which are based on quadrilateral finite elements whereas OPERA and POISSON use triangular finite elements. Quadratic shape functions were chosen to reach higher accuracy. To keep the comparison highly objective, each FE-model kept

the same number of equations, namely 25000. The POISSON code is based on linear triangular elements. Thus, to reach the same accuracy in the solution, at least three times as many elements are necessary. The maximum number of elements in POISSON is 60000.

4.1.2 Results calculated by means of different FE-codes

Table (4.1) shows the results calculated by means of the FE-codes most frequently applied to magnet design at CERN.

Table 4.1: Relative multipole errors at I=500A, at r=10mm in units of 10^{-4} ($*\ldots$ calculated at r=20mm and scaled down by means of Eq. (1.1))

	analytical	numerical solution				
$I[A]$	$ROXIE$	$FEM2D$	$ANSYS^*$	$OPERA^*$	$FEM2D$	$POISSON$
500	$B_{iot}S_{avart}$	A_{red}	A_{tot}			
$B_1[T]$	−0.25690	−0.25691	−0.25671	−0.25699	−0.25625	−0.2567
b_3	−0.06715	−0.06476	0.08332	0.01292	0.40220	0.0174
b_5	−0.00292	−0.00303	−0.00132	−0.00736	0.00045	−0.0155
b_7	−0.00068	−0.00067	−0.00032	−0.00090	−0.00078	−0.0019
b_9	−0.00069	−0.00069	−0.00079	−0.00073	−0.00073	−0.0007

It has to be remarked that the releases of ANSYS and OPERA currently available at CERN present results with floating numbers restricted to six significant figures after the decimal point. The differences between the results can be explained as follows: Due to the keystoning of the superconducting cable the current density is higher at the narrow side of the cable. As the grading of the current density is not considered in the class of FE-codes based on the total vector potential $\vec{A}$-formulation, most of the difference in the b_3 component can be explained. The difference in the higher order multipoles, i.e. b_5, b_7, and b_9 may result from the incomplete coil modelling.

4.1.3 Influence of the coil modelling on the field errors

As well as the above mentioned FE-codes, the classical ROXIE program is able to handle an homogeneous current density distribution within the conductors and so the influence of the coil modelling on the field errors can be investigated. Analysing the results shown in Table (4.2), it can be seen that the grading of the current density has a strong influence not only on b_3 but also on all higher order multipoles. Furthermore, the influence of the incomplete modelling of the coil seems to be even stronger than that of the grading of the current density. This indicates a certain influence of the nature of the finite element on the field distribution, depending on the finite element type used in the FE-code.
Fig. (4.2) shows the approximation of an arc-shaped conductor by means of triangular elements and quadrilateral isoparametric elements. On bent shapes, the intermediate points between two vertices of a finite element do not coincide and therefore, the distribution of the sampling points chosen for the Gauss quadrature is slightly different. Thus, the finite element itself has an influence on the shape of the integrated field.

Table 4.2: Relative multipole errors at I=500A, at r=10mm in units of 10^{-4} ($*$... calculated at r=20mm and scaled down by means of Eq. (1.1))

	analytical	numerical solution				
$I[A]$	$ROXIE$	$FEM2D$	$ANSYS^*$	$OPERA^*$	$FEM2D$	$POISSON$
500	$B_{iot}S_{avart}$	A_{red}	A_{tot}			
$B_1[T]$	−0.25652	−0.25613	−0.25671	−0.25699	−0.25625	−0.2567
b_3	0.08525	0.08765	0.08332	0.01292	0.40220	0.0174
b_5	0.00444	0.00433	−0.00132	−0.00736	0.00045	−0.0155
b_7	−0.00051	−0.00050	−0.00032	−0.00090	−0.00078	−0.0019
b_9	−0.00065	−0.00065	−0.00079	−0.00073	−0.00073	−0.0007

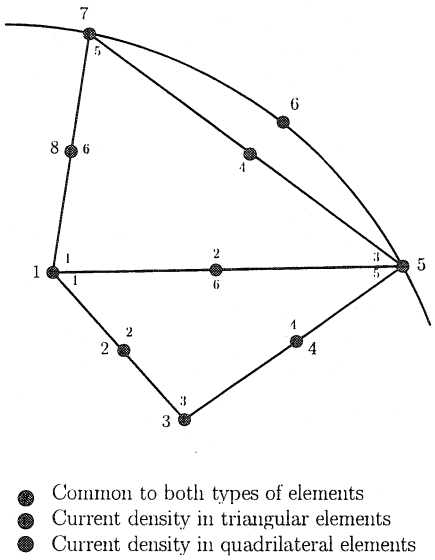

Figure 4.2: Modelling of an arc-shaped conductor by means of different types of finite elements

To see this influence on the field errors, the D1 coil was replaced by a simple racetrack dipole coil with rectangular-shaped conductors as shown in Fig. (4.3). Table (4.3) gives the results for the rectangular-shaped dipole coil.

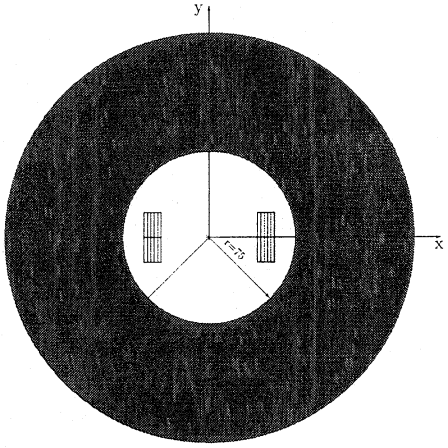

Figure 4.3: Simple rectangular-shaped dipole coil

Table 4.3: Relative multipole errors at I=500A, at r=10mm in units of 10^{-4} ($*$... calculated at r=20mm and scaled down by means of Eq. (1.1))

	analytical	numerical solution				
$I[A]$	*ROXIE*	*FEM2D*	*ANSYS**	*OPERA**	*FEM2D*	*POISSON*
500	$B_{iot}S_{avart}$	A_{red}	A_{tot}			
$B_1[T]$	−0.05603	−0.05603	−0.05603	−0.05603	−0.05603	−0.05603
b_3	237.66988	237.68603	237.01230	237.65981	237.69085	237.62851
b_5	5.39382	5.39358	5.36514	5.39223	5.39258	5.39212
b_7	0.07658	0.07690	0.08020	0.07613	0.07652	0.07642
b_9	−0.00083	−0.00039	−0.00080	−0.00073	−0.00045	−0.00062

Now the results compare perfectly well. Fig. (4.4) does give an answer to it. In ROXIE, the position of the line-currents within a conductor is chosen according to the position of the strands in the cable. Fig. (4.4) shows the position of these line currents in a rectangular-shaped conductor. The line currents lay inside the edges of the finite elements.
To conclude then, the conformity between the different approaches of coil modelling is just given for simple coils using rectangular-shaped conductors. This is considered invalid when single conductors of keystoned-type are joined to make blocks without forming a perfectly smooth surface on the inner and outer radius of the coil layer as shown in Fig. (2.5).

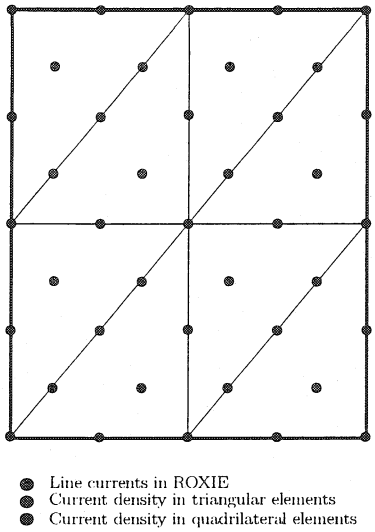

Figure 4.4: Modelling of the current density in a rectangular-shaped conductor by finite elements and by the ROXIE-program

4.2 The main dipole geometry

4.2.1 Coil geometry

The coil used for the study is the re-optimized design (drawing no. 06LHCMB-T-00010) which partly compensates the b_5 ,b_7 , and b_9 components resulting from persistent currents at injection. They were estimated to be [28], Table (4.4). Fig. (4.5) shows the coil cross-section. Note that due to the insufficient keystoning of the cable the blocks do not follow the curvature of circles on the outer diameter of the coils.

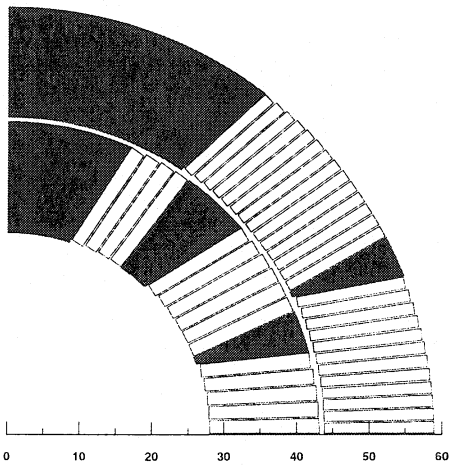

Figure 4.5: Coil with re-optimized block angles for part compensation of the persistent current multipole errors at injection

Table 4.4: Relative multipole errors due to persistent currents at injection, at r=10mm in units of 10^{-4} for main dipole coil, see Fig. (4.5)

b3	−4.1667
b5	+0.2073
b7	−0.0357
b9	+0.0073
b11	+0.0008

4.2.2 Yoke geometry

For the yoke, the drawing 06LHCMBP-N10070 for the warm laminations was given and the cold dimensions were calculated. Note that the beam separation distance is 194 mm in cold conditions (see Table (4.5)). This assumption would leave the yoke laminations unchanged to the present drawings. Fig. (4.6) shows a sketch of the yoke with the symbols used in the ROXIE input file. All these dimensions can be addressed as design variables for a subsequent yoke optimisation or fine-tuning. The dipole geometry with coil and iron yoke is displayed in Fig. (4.7).

4.2.3 Results

4.2.3.1 Mesh size

In Table (4.6) you can see the calculated multipole content for the LHC main dipole for different numbers of elements in the finite-element mesh. The results show convergence for meshes bigger than 28000 equations. Note that the relative high values for the b_5, b_7, b_9 components are due to the fact that the persistent currents at injection are partly compensated for by the coil design. The higher order multipoles b_7, b_9, b_{11} are hardly influenced by the yoke and the iron saturation effect. The estimates for a coil in an infinitely permeable iron yoke are $b_7 = 0.034$, $b_9 = -0.010$, and $b_{11} = 0.0088$. These multipoles are therefore a good measure for the accuracy of the field solution. The quadrupole component that arises from the two-in-one geometry is relatively insensitive to the mesh size.

4.2.3.2 Influence of the boundary conditions

Table (4.7) shows the calculated multipole content for the LHC main dipole depending on the boundary conditions. The boundary was chosen to be 1.1, 5., and 10. times the radius of the cold mass. The result shows that the higher order multipoles are not dependent on the boundary, whereas the iron induced quadrupole component and the sextupole component can be used as a measure for the accuracy of the solution. A boundary which is at least 5 times the radius of the cold mass should be sufficient.

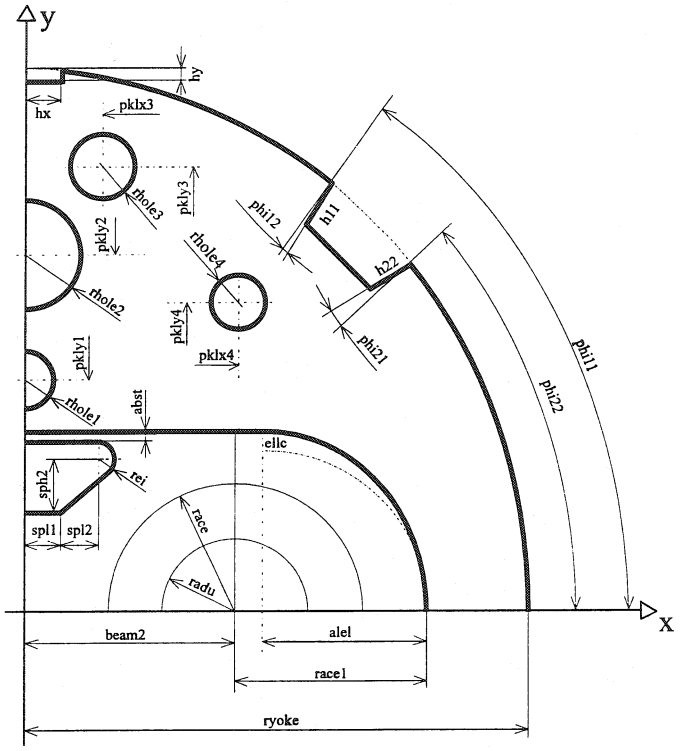

Figure 4.6: Symbolic input data for the main dipole geometry, see Table (4.5)

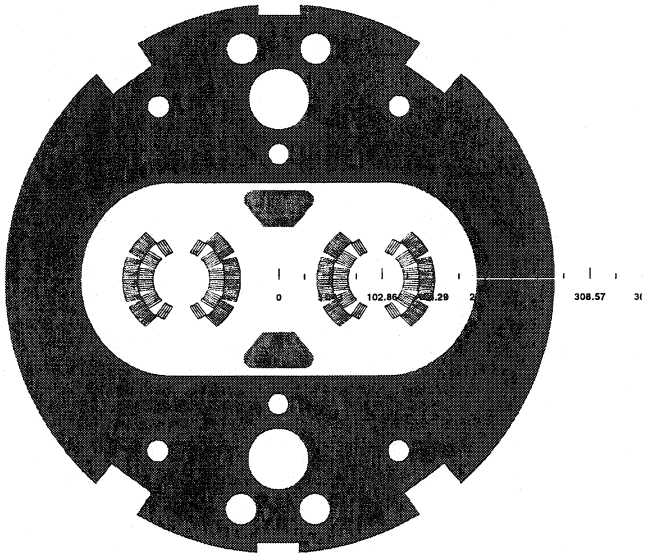

Figure 4.7: Geometrical model of the main dipole cold mass

Table 4.5: Warm and cold dimension for the yoke laminations considered for the study

	Warm dim. (m)	cold dim. (m)	Description
beam2	0.09718	0.097	Beam separation distance / 2.
ryoke	0.275	0.27448	Radius of iron yoke
radu	0.055	0.055	Radius inside coil (for meshing reasons)
racel	0.10082	0.10062	Collar outer diameter (from center of coil)
alel	0.0904	0.09023	Center of ellipse (from collar outer diam.)
ellc	0.0058	0.00579	Ellipticity
abst	0.007	0.00699	Dist. of iron insert from collar outer diam.
rei	0.010	0.00998	Radius of insert
spl1	0.0152	0.01517	Width 1 of insert
spl2	0.0101	0.01008	Width 2 of insert
sph2	0.027	0.02695	Height of insert
pklx1	0.	0.	x-position of hole
pkly1	0.125	0.12476	y-position of hole
rhole1	0.010	0.00998	Radius of hole
pklx2	0.	0.	x-position of hole (Heat exchanger)
pkly2	0.180	0.1796	y-position of hole
rhole2	0.030	0.02994	Radius of hole
pklx3	0.037	0.03693	x-position of hole
pkly3	0.230	0.22956	y-position of hole
rhole3	0.015	0.01497	Radius of hole
pklx4	0.1205	0.12027	x-position of hole
pkly4	0.172	0.17167	y-position of hole
rhole4	0.0103	0.01028	Radius of hole
fill1	0.985	0.985	Filling factor iron yoke
fill2	0.963	0.963	Filling factor iron insert
hx	0.021	0.02096	Width of gap control spacer
hy	0.011	0.01098	Depth of gap control spacer
h11	0.026	0.02595	Depth of bus-bar slot on upper angle
phi11	58.9	58.9	Upper positioning angle
phi12	-3.	-3.	Upper inclination angle
h22	0.026	0.02595	Depth of slot on lower angle
phi22	48.3	48.	Lower positioning angle
phi21	3.	3.	Lower inclination angle

Table 4.6: Relative multipole errors in units of 10^{-4} as a function of mesh size at normal operation 8.4 T (r=10mm); main dipole without helium vessel; (far field boundary at 5.0 × ryoke)

	Number of equations			
	1800	7200	28500	36000
n	norm. b_n	norm. b_n	norm. b_n	norm. b_n
2	1.19320	1.27823	1.28336	1.28377
3	−0.21129	−0.24245	−0.23930	−0.23928
4	−0.14697	−0.14834	−0.14867	−0.14875
5	−0.20487	−0.18869	−0.18650	−0.18650
6	0.01211	0.00060	0.00060	0.00067
7	−0.06011	0.03308	0.03381	0.03380
8	0.02150	−0.00040	0.00003	0.00002
9	0.06972	−0.00338	−0.01025	−0.01026
10	−0.00654	0.00003	0.00000	0.00009
11	−0.00996	0.01680	0.00771	0.00769

Table 4.7: Relative multipole errors in units of 10^{-4} depending on the far field boundary at nominal operation 8.4 T (r=10mm); main dipole without helium vessel; calculated with 28500 equations

	Distance of far field boundary		
	1.1 × ryoke	5.0 × ryoke	10.0 × ryoke
n	b_n	b_n	b_n
1	$-8.40231T$	$-8.36833T$	$-8.36815T$
2	2.36867	1.28336	1.27138
3	−0.13080	−0.23930	−0.24019
4	−0.13138	−0.14867	−0.14885
5	−0.18591	−0.18650	−0.18651
6	0.00067	0.00060	0.00060
7	0.03378	0.03381	0.03381
8	0.00004	0.00003	0.00003
9	−0.01024	−0.01025	−0.01025
10	0.00000	0.00000	0.00000
11	0.00773	0.00771	0.00770

Table 4.8: Relative multipole errors in units of 10^{-4} considering the grading of the current density in the superconducting cable compared to the results with no grading (r=10mm); main dipole without helium vessel; (5.0 × ryoke, 28500 equations)

	At injection, 0.54T		At nominal operation, 8.4T	
	without grading	with grading	without grading	with grading
n	b_n	b_n	b_n	b_n
2	−0.25362	−0.24612	1.24352	1.28336
3	−0.12407	−0.71274	0.39358	−0.23930
4	−0.11136	−0.11050	−0.14982	−0.14867
5	−0.18642	−0.17652	−0.19540	−0.18650
6	0.00185	0.00183	0.00056	0.00060
7	0.03782	0.03556	0.03836	0.03381
8	−0.00002	−0.00002	−0.00002	0.00003
9	−0.01006	−0.01056	−0.01017	−0.01025
10	0.00002	0.00002	0.00001	0.00000
11	0.00662	0.00704	0.00693	0.00771

4.2.3.3 Influence of the grading of the current density

Due to the keystoning of the superconducting cable the current density is higher at the narrow side of the cable. This effect cannot be neglected as the sextupole field component changes. Table (4.8) shows the results for a grading of the current density and where the grading is not considered. The difference is an offset of the sextupole component of 0.6 units. The saturation effects are the same since the excitational field in the iron does not change very much with this grading. Therefore, also the quadrupole components that are due to the two in one design shows only little dependence on the grading. If the accurateness of the modelling of the coils is not sufficient (as, is the case in most of the commercially available FE packages) the sextupole component may contain a relatively large error.

4.3 Numerical results on different applications

In this section the latest estimates for the multipole errors in the LHC main dipoles are collected.

4.3.1 Characteristic design features of the main dipole magnet

Fig. (4.8) and Fig. (4.9) show the physical explanation of the measures taken to minimize the variation of the quadrupole component (see section (2.2.5)). The quadrupole component results from the two-in-one design and the flux being divided into one path across the mid plane x=0 into the second aperture and one across the y=0 into the lower half of the yoke. The little hole (hole 1) in the mid plane helps to balance the flux in the two paths, one across the mid plane into the second aperture and the second along the yoke leg across the y=0

plane. The effect of this hole vanishes with saturation but the second hole (hole 3) between heat exchanger tube (hole 2) and the outer yoke radius leads to local saturation effects at nominal current thus it balances the flux in the two paths.

4.3.2 The influence of the asymmetric helium vessel

The helium vessel with its off-center with respect to the y=0 axis of the magnet cold mass introduces some skew dipole and skew quadrupole which are still relatively small at 8.4 T. The effect gets more pronounced at fields higher than 9 T as can be seen in Fig. (4.10). However, the helium vessel also has an influence on the variation of the normal quadrupole which increases and is then about 2 units at 8.4 T. Sextupole and higher order multipoles are basically not affected. For the sake of completeness also the multipoles for a symmetric vessel are given in Table (4.9). The skew terms in that case are spurious as they are intrinsically not existent in the symmetric case. These components are a measure for the accuracy of the field solution and were therefore not omitted from the table. The effect of the recent change in thickness from 10mm to 12mm can be neglected.

4.3.3 The influence of the bus-bar

Table (4.10) shows the multipole content for the main dipole in its off-centered helium vessel with the bus-bars powered. The bus-bar and the asymmetry caused by the trim bus-bar with its lower current have some effect on the skew multipole terms at high fields. They partly compensate the effects from the asymmetric helium vessel, but that depends on the powering of the bus-bars. If the powering is reversed the values displayed in the lower section of the table are obtained. The geometry of the main dipole cold mass with its off-centered vacuum vessel and SC bus-bars is shown in Fig. (4.12).

4.3.4 Vertical shift of coils in iron yoke

The big advantage of the new program is that the coils have not to be meshed and therefore asymmetries caused by deformations or shifts of the coil blocks can easily be calculated. As an example the effects resulting from a vertical (y direction) off-centering of the coils with respect to the yoke are calculated given in Table (4.11). The coil was shifted by 0.05 mm in upward direction. As expected, the main effect is on the skew quadrupole of about -0.17 units at injection. Interesting is the reduction of these errors with excitation because of the different saturation in the upper and lower yoke halfs (see Fig. (4.13)). At the nominal field the skew quadrupole is -0.11 units.

4.3.5 The fringing field outside the cold mass

Fig. (4.14) shows the fringing field at a radius of 290 mm outside the cold mass with the bus-bar powered as a function of the angular position, -90 deg. is the lower edge of the magnet, 90 deg. the upper. The influence of the bus-bar at a position of 56 deg is clearly visible. For the sake of completeness Fig. (4.15) shows the fringing field at the same radius without the bus-bars.

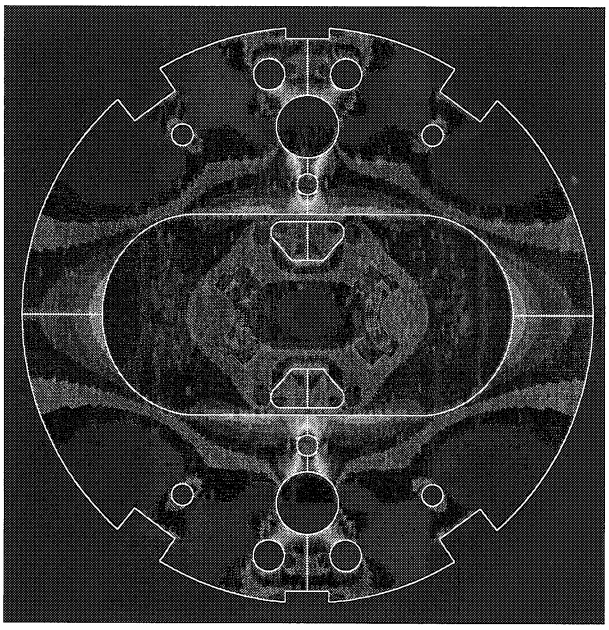

Figure 4.8: Reduced field (resulting from iron magnetization only) at injection

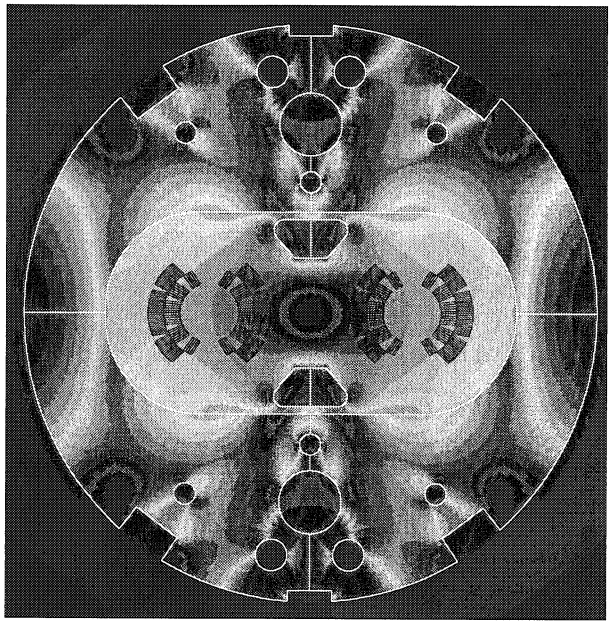

Figure 4.9: Reduced field at nominal operation

plane. The effect of this hole vanishes with saturation but the second hole (hole 3) between heat exchanger tube (hole 2) and the outer yoke radius leads to local saturation effects at nominal current thus it balances the flux in the two paths.

4.3.2 The influence of the asymmetric helium vessel

The helium vessel with its off-center with respect to the y=0 axis of the magnet cold mass introduces some skew dipole and skew quadrupole which are still relatively small at 8.4 T. The effect gets more pronounced at fields higher than 9 T as can be seen in Fig. (4.10). However, the helium vessel also has an influence on the variation of the normal quadrupole which increases and is then about 2 units at 8.4 T. Sextupole and higher order multipoles are basically not affected. For the sake of completeness also the multipoles for a symmetric vessel are given in Table (4.9). The skew terms in that case are spurious as they are intrinsically not existent in the symmetric case. These components are a measure for the accuracy of the field solution and were therefore not omitted from the table. The effect of the recent change in thickness from 10mm to 12mm can be neglected.

4.3.3 The influence of the bus-bar

Table (4.10) shows the multipole content for the main dipole in its off-centered helium vessel with the bus-bars powered. The bus-bar and the asymmetry caused by the trim bus-bar with its lower current have some effect on the skew multipole terms at high fields. They partly compensate the effects from the asymmetric helium vessel, but that depends on the powering of the bus-bars. If the powering is reversed the values displayed in the lower section of the table are obtained. The geometry of the main dipole cold mass with its off-centered vacuum vessel and SC bus-bars is shown in Fig. (4.12).

4.3.4 Vertical shift of coils in iron yoke

The big advantage of the new program is that the coils have not to be meshed and therefore asymmetries caused by deformations or shifts of the coil blocks can easily be calculated. As an example the effects resulting from a vertical (y direction) off-centering of the coils with respect to the yoke are calculated given in Table (4.11). The coil was shifted by 0.05 mm in upward direction. As expected, the main effect is on the skew quadrupole of about -0.17 units at injection. Interesting is the reduction of these errors with excitation because of the different saturation in the upper and lower yoke halfs (see Fig. (4.13)). At the nominal field the skew quadrupole is -0.11 units.

4.3.5 The fringing field outside the cold mass

Fig. (4.14) shows the fringing field at a radius of 290 mm outside the cold mass with the bus-bar powered as a function of the angular position, -90 deg. is the lower edge of the magnet, 90 deg. the upper. The influence of the bus-bar at a position of 56 deg is clearly visible. For the sake of completeness Fig. (4.15) shows the fringing field at the same radius without the bus-bars.

Table 4.9: Relative multipole errors in units of 10^{-4} at r=10mm for the main dipole in an symmetric and asymmetric helium vessel of 10mm or 12mm thickness

	Centered helium vessel (10mm thick)			
	At injection, 0.54T		At nominal operation, 8.4T	
n	b_n	a_n	b_n	a_n
2	−0.24788	0.00000	1.98609	0.00000
3	−0.71298	0.00000	−0.15191	0.00000
4	−0.11049	−0.00002	−0.13634	−0.00001
5	−0.17651	0.00000	−0.18475	0.00000
6	0.00183	0.00000	0.00064	0.00000
7	0.03555	0.00000	0.03598	0.00000
8	−0.00002	−0.00002	−0.00002	−0.00001
9	−0.01055	0.00000	−0.01065	0.00000
10	0.00002	0.00000	0.00001	0.00000
11	0.00703	0.00000	0.00737	0.00000

	Off-centered (80mm) helium vessel (10mm thick)			
	At injection, 0.54T		At nominal operation, 8.4T	
n	b_n	a_n	b_n	a_n
1		0.00003		0.59679
2	−0.24788	0.00000	2.00339	−0.06615
3	−0.71298	0.00000	−0.14886	0.00540
4	−0.11049	0.00002	−0.13595	−0.00024
5	−0.17651	−0.00000	−0.18474	−0.00001
6	0.00183	0.00000	0.00064	0.00000
7	0.03555	0.00000	0.03597	0.00000
8	−0.00002	0.00002	−0.00002	−0.00001
9	−0.01055	−0.00000	−0.01065	0.00000
10	0.00002	0.00000	0.00001	0.00000
11	0.00703	0.00000	0.00737	0.00000

	Off-centered (80mm) helium vessel (12mm thick)			
	At injection, 0.54T		At nominal operation, 8.4T	
n	b_n	a_n	b_n	a_n
1		0.00003		0.59679
2	−0.24788	0.00000	2.00362	−0.06635
3	−0.71298	0.00000	−0.14884	0.00542
4	−0.11049	−0.00002	−0.13595	−0.00024
5	−0.17651	0.00000	−0.18474	0.00001
6	0.00183	0.00000	0.00064	0.00000
7	0.03555	0.00000	0.03597	0.00000
8	−0.00002	−0.00002	−0.00002	−0.00001
9	−0.01055	0.00000	−0.01065	0.00000
10	0.00002	0.00000	0.00001	0.00000
11	0.00703	0.00000	0.00737	0.00000

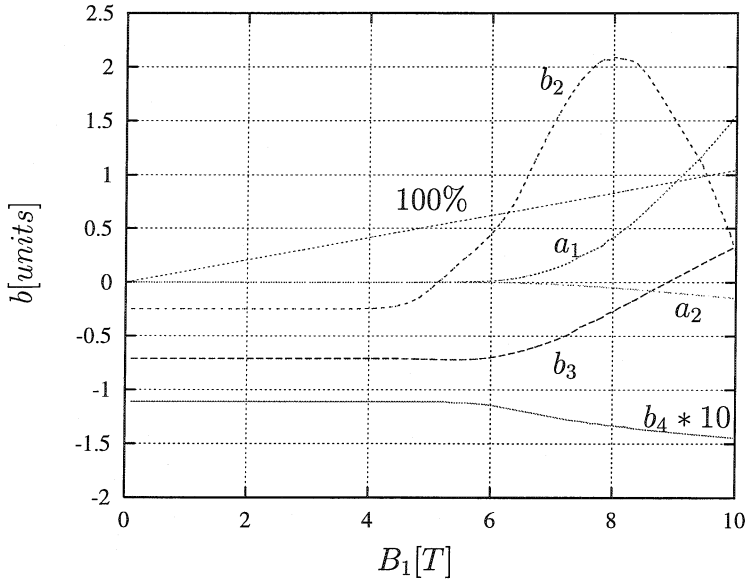

Figure 4.10: Variation of lower order multipole errors with main field (main dipole in asymmetric helium vessel)

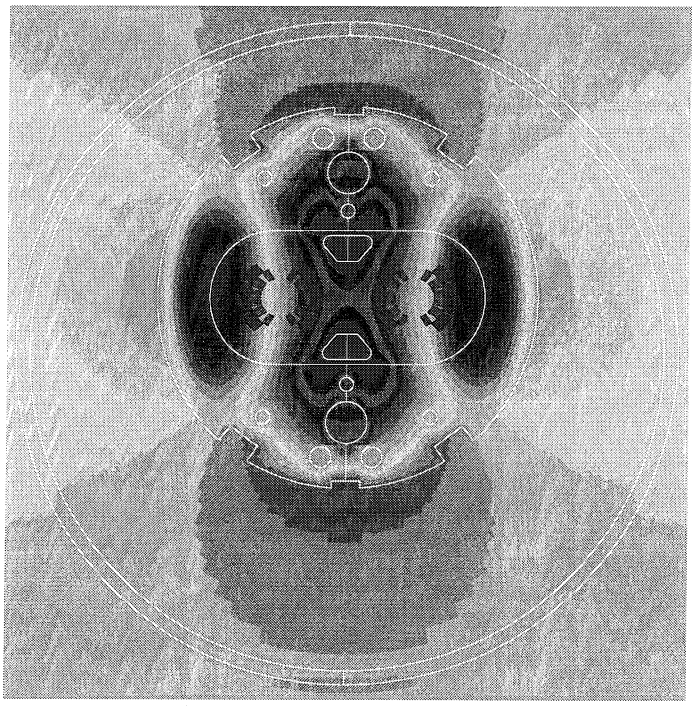

Figure 4.11: Reduced vector potential for main dipole in asymmetric helium vessel

Table 4.10: Relative multipole errors in units 10^{-4} at r=10mm for main dipole in off-centered cryostat considering the bus bars with different powering

	At injection, 0.54T		At nominal operation, 8.4T	
	norm.	skew	norm.	skew
n	b_n	a_n	b_n	a_n
1	0.00000	−0.00088	0.00000	0.39255
2	−0.24794	0.00007	1.98838	−0.04313
3	−0.71297	0.00000	−0.15161	0.00389
4	−0.11049	−0.00002	−0.13627	−0.00015
5	−0.17651	0.00000	−0.18475	0.00001
6	0.00183	0.00000	0.00064	0.00000
7	0.03555	0.00000	0.03598	0.00000
8	−0.00002	−0.00002	−0.00002	−0.00001
9	−0.01055	0.00000	−0.01066	0.00000
10	0.00002	0.00000	0.00001	0.00000
11	0.00703	0.00000	0.00737	0.00000

	At injection, 0.54T		At nominal operation, 8.4T	
	norm.	skew	norm.	skew
n	b_n	a_n	b_n	a_n
1	0.00000	0.00088	0.00000	0.78260
2	−0.24782	−0.00007	2.00940	−0.08839
3	−0.71299	0.00000	−0.15323	0.00693
4	−0.11049	−0.00002	−0.13575	−0.00033
5	−0.17651	0.00000	−0.18466	0.00001
6	0.00183	0.00000	0.00065	0.00000
7	0.03555	0.00000	0.03597	0.00000
8	−0.00002	−0.00002	−0.00002	−0.00001
9	−0.01055	0.00000	−0.01065	0.00000
10	0.00002	0.00000	0.00001	0.00000
11	0.00703	0.00000	0.00737	0.00001

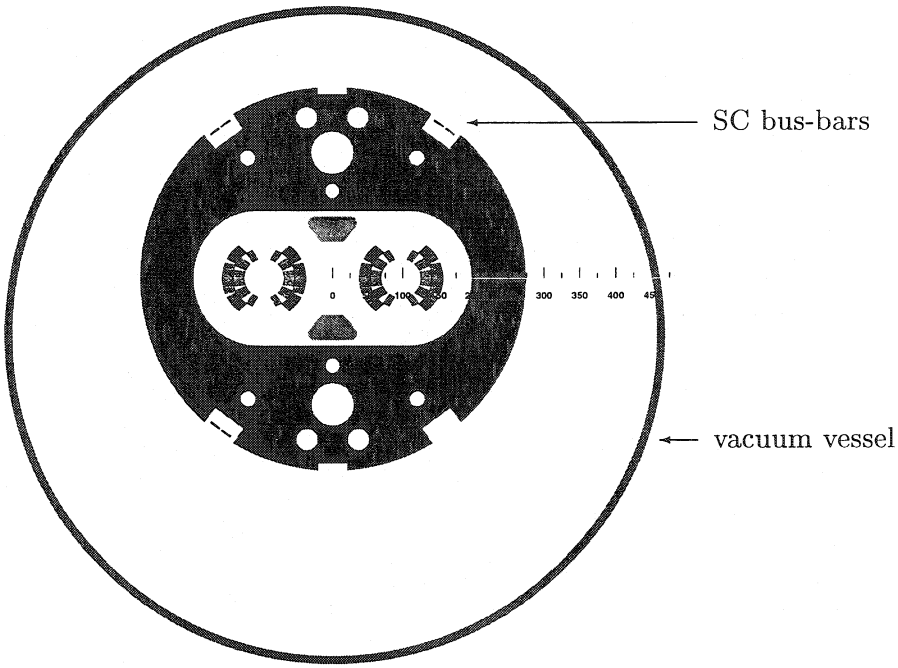

Figure 4.12: Geometry of main dipole cold mass with its off-centered vacuum vessel and SC bus-bars

Table 4.11: Relative multipole errors in units of 10^{-4} at r=10mm for main dipole with off-centering of the coils, the cryostat was assumed to be centered with respect to the cold mass in order to avoid part cancellation of effects

	At injection, 0.54T		At nominal operation, 8.4T	
n	norm. b_n	skew a_n	norm. b_n	skew a_n
1	0.00000	0.02206	0.00000	−0.00068
2	−0.24787	−0.17156	1.98608	−0.11609
3	−0.71296	−0.00019	−0.15188	0.00047
4	−0.11049	0.00387	−0.13634	0.00352
5	−0.17652	0.00001	−0.18476	0.00001
6	0.00183	−0.00104	0.00064	−0.00106
7	0.03556	0.00000	0.03598	0.00000
8	−0.00002	0.00040	−0.00002	0.00041
9	−0.01056	0.00000	−0.01067	0.00000
10	0.00002	−0.00045	0.00001	−0.00046
11	0.00703	0.00000	0.00737	0.00000

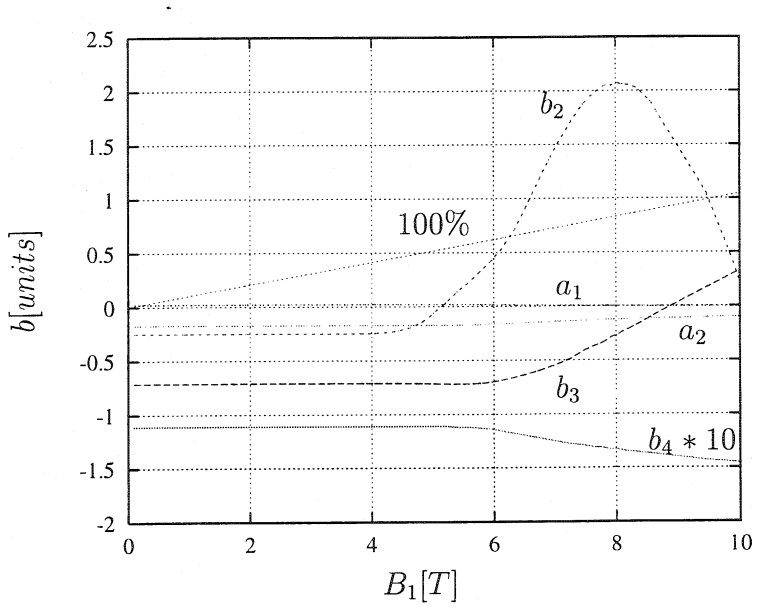

Figure 4.13: Variation of the lower order multipoles versus main field (coil off-centered)

4.3.6 Different filling factors in upper and lower iron insert

Table (4.12) shows the multipole content for the main dipole in a symmetric cryostat but different filling factors in the upper and lower iron insert in the collars. The filling factors used in the calculations are 0.963 in the upper and 0.8667 in the lower insert.

4.3.7 Collared coil structure without yoke

After the collaring of the coils, magnetic measurements are made at room temperature in order to check the field quality. As in the collared coil structure the iron insert has a large influence on the quadrupole and sextupole component, the effects have to be separated if acceptance of the coil is based on these measurements. Table (4.13) shows the relative multipole errors for the coil collar assembly at 15 A excitation.

4.3.8 The effect of tuning-shims

Fig. (4.18) a., Fig. (4.18) b., and Fig. (4.18) c. show the effect of tuning-shims to correct skew dipole components that might arise from up-down asymmetries in the coil halfs or off-centering of the coil with respect to the yoke. Note that the tuning-shims are symmetrically placed with respect to the two beam channels as shown in Fig. (4.17). Table (4.14) gives the corresponding multipole errors for injection and operation field level.

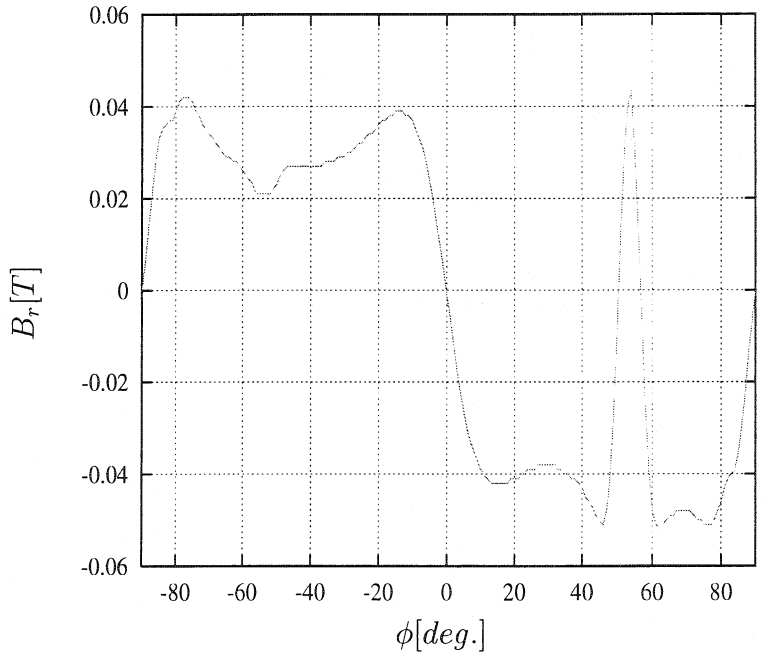

Figure 4.14: Fringing field outside the cold mass (r=290 mm) with the bus-bar powered, main dipole in asymmetric helium vessel

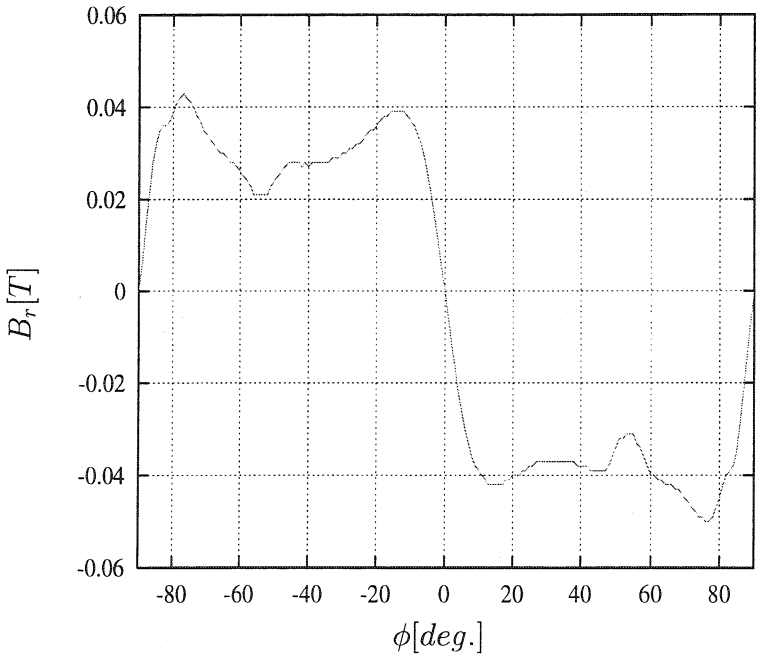

Figure 4.15: Fringing field outside the cold bore (radius=290 mm), main dipole in asymmetric helium vessel

Table 4.12: Relative multipole errors in units of 10^{-4} at r=10mm for the main dipole with different filling factors in upper and lower iron insert, (difference in filling factor 10%). The cryostat was assumed to be centered with respect to the cold mass in order to avoid part cancellation of effects

	At injection, 0.54T		At nominal operation, 8.4T	
n	norm. b_n	skew a_n	norm. b_n	skew a_n
1	0.00000	−0.00343	0.00000	−0.28687
2	−0.24693	0.00001	2.05968	−0.02278
3	−0.71307	0.00009	−0.16609	0.01122
4	−0.11049	−0.00003	−0.13650	−0.00170
5	−0.17651	0.00000	−0.18457	0.00014
6	0.00183	0.00000	0.00063	0.00000
7	0.03555	0.00000	0.03598	0.00000
8	−0.00002	−0.00002	−0.00002	−0.00001
9	−0.01055	0.00000	−0.01066	0.00000
10	0.00002	0.00000	0.00001	0.00000
11	0.00703	0.00000	0.00736	0.00001

Table 4.13: Relative multipole errors in units of 10^{-4} at r=10mm for collared coil with iron insert (excitation at room temperature; I=15 A)

	At injection, 0.54T	
n	norm. b_n	skew a_n
2	−99.78772	0.00000
3	6.36313	0.00000
4	−0.06524	0.00000
5	−0.25720	0.00000
6	0.00595	0.00000
7	0.03858	0.00000
8	−0.00001	0.00000
9	−0.01174	0.00000
10	0.00006	0.00000
11	0.01007	0.00000

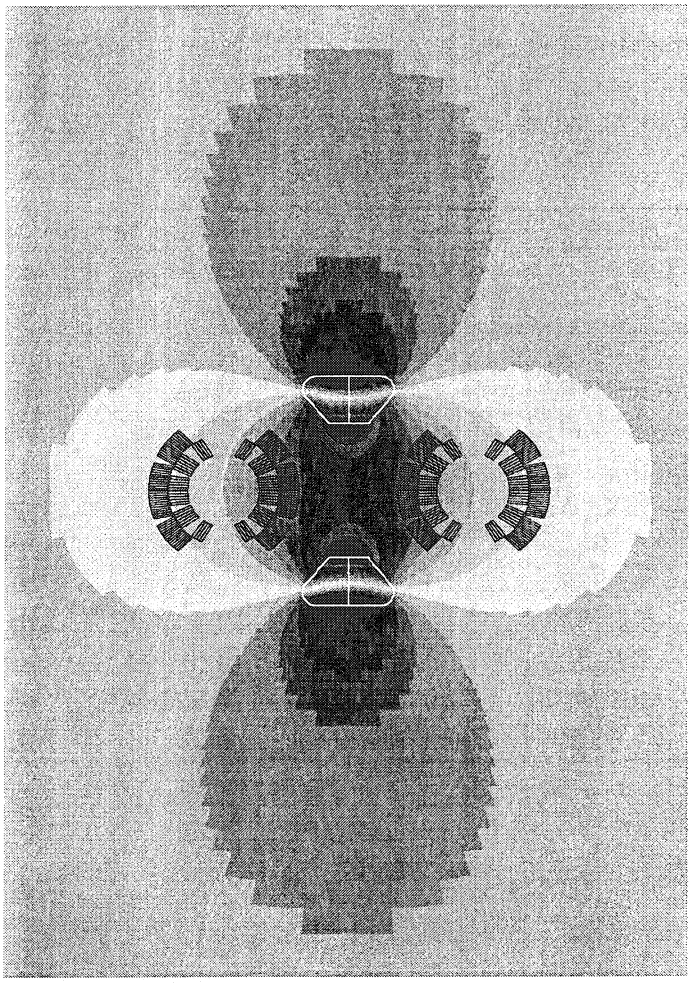

Figure 4.16: Reduced vector potential in the coil collar assembly with both apertures powered with 15 A at room temperature

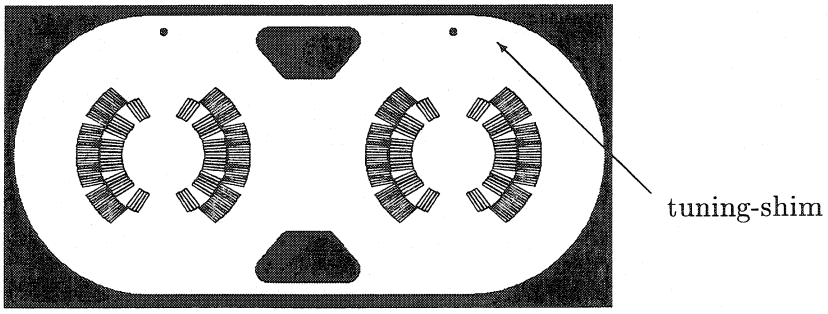

Figure 4.17: Collar structure of the LHC main dipole magnet showing the tuning-shims

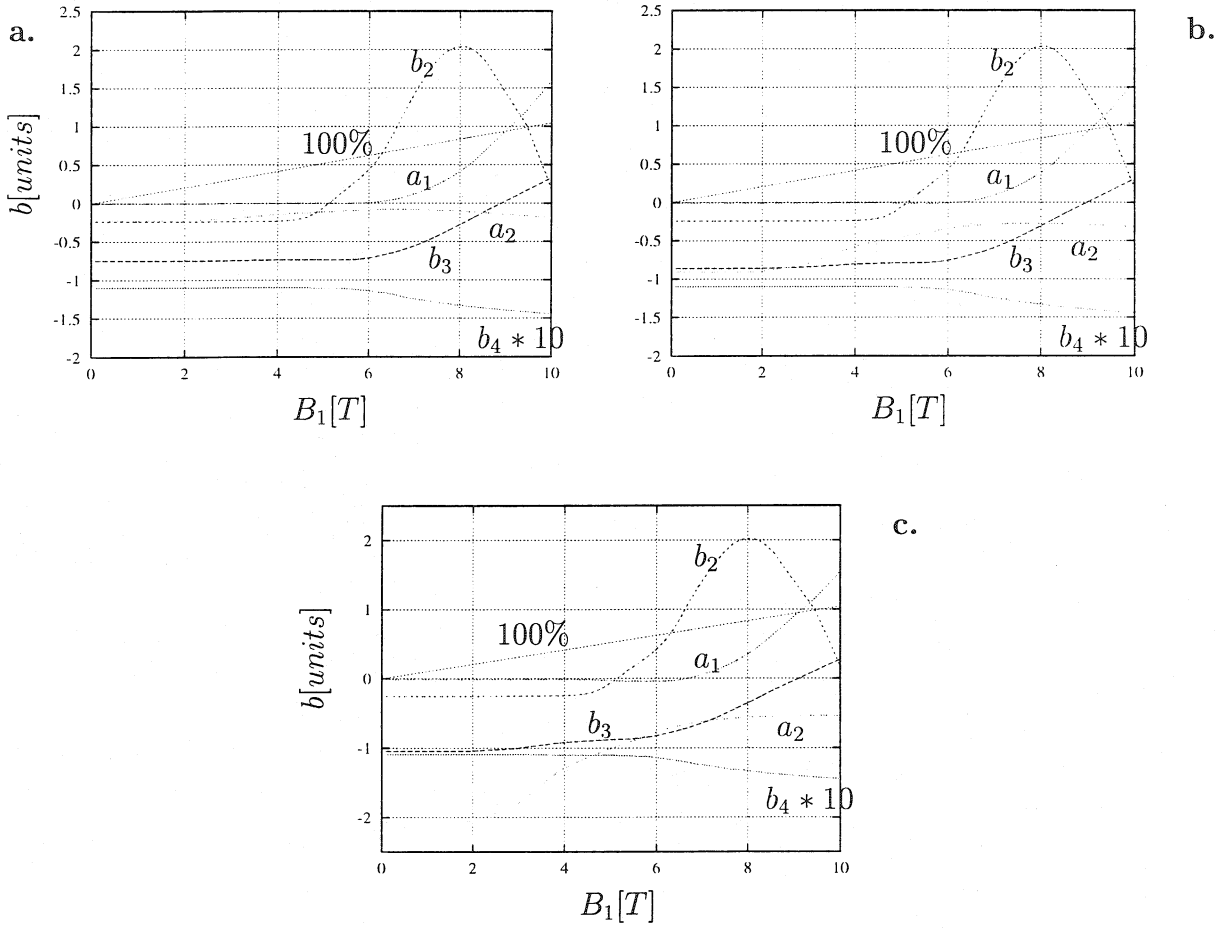

Figure 4.18: Variation of the lower order multipoles versus main field for main dipole with tuning-shims: a.) 2mm, b.) 4mm, and c.) 6mm diameter

Table 4.14: Relative multipole errors in units of 10^{-4} at r=10mm for dipole coil with tuning-shims in the upper half of the collar

	2mm diameter shim			
	At injection, 0.54T		At nominal operation, 8.4T	
n	b_n	a_n	b_n	a_n
1	0.00000	−0.00141	0.00000	0.60191
2	−0.23794	−0.22341	1.94473	−0.12116
3	−0.75166	0.00059	−0.15858	0.00580
4	−0.11004	0.00499	−0.13601	0.00094
5	−0.17577	−0.00001	−0.18463	0.00002
6	0.00132	−0.00012	0.00021	−0.00003
7	0.03648	0.00001	0.03686	0.00002
8	−0.00044	−0.00011	−0.00037	−0.00011
9	−0.00966	0.00001	−0.00993	0.00003
10	0.00098	−0.00002	0.00081	−0.00001
11	0.00500	0.00001	0.00556	0.00001

	4mm diameter shim			
	At injection, 0.54T		At nominal operation, 8.4T	
n	b_n	a_n	b_n	a_n
1		−0.00585		0.57960
2	−0.24405	−0.90807	1.93815	−0.28135
3	−0.86048	0.00236	−0.18433	0.00655
4	−0.10972	0.02070	−0.13597	0.00475
5	−0.17351	−0.00006	−0.18406	0.00001
6	0.00131	−0.00042	0.00021	−0.00011
7	0.03646	0.00001	0.03686	0.00002
8	−0.00044	−0.00006	−0.00037	−0.00009
9	−0.00963	0.00001	−0.00992	0.00003
10	0.00098	−0.00004	0.00081	−0.00001
11	0.00492	0.00000	0.00555	0.00000

	6mm diameter shim			
	At injection, 0.54T		At nominal operation, 8.4T	
n	b_n	a_n	b_n	a_n
1		−0.01333		0.54247
2	−0.25438	−2.06748	1.92718	−0.54804
3	−1.04479	0.00536	−0.22720	0.00780
4	−0.10918	0.04730	−0.13591	0.01110
5	−0.16967	−0.00014	−0.18312	0.00001
6	0.00130	−0.00092	0.00021	−0.00024
7	0.03643	0.00000	0.03685	0.00002
8	−0.00044	0.00004	−0.00037	−0.00007
9	−0.00957	0.00001	−0.00991	0.00003
10	0.00098	−0.00006	0.00081	−0.00002
11	0.00479	−0.00001	0.00552	0.00000

Chapter 5

The $\vec{A}_r$-Formulation with Edge-Elements

5.1 Edge-elements and their properties

5.1.1 Introduction

The earliest finite elements were scalar, and had as unknown parameters the values of the scalar field at the nodes of the element. When the interest on vector fields came up, the natural approach was to treat the vector field as three coupled scalar fields. The elements were still scalar, but each node had three unknowns instead of one:

$$\vec{A} = \sum_{i=1}^{n_n} f_i \left(A_x \vec{e_x} + A_y \vec{e_y} + A_z \vec{e_z}\right). \tag{5.1}$$

The continuity of all three components between elements is imposed by setting nodal values in adjacent elements to be identical as shown in Fig. (5.1).

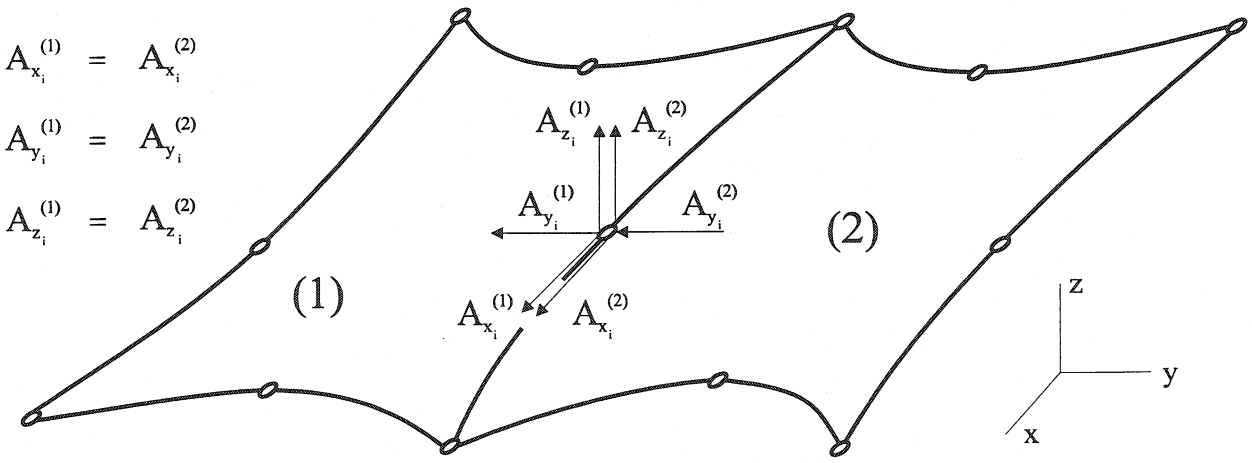

Figure 5.1: Continuity conditions between two adjacent node-based elements

For instance, consider the interface conditions between two different materials of reluctivities ν_1 and ν_2. It is well known that the continuity requirements of the magnetic field at the

interface are

$$\vec{n} \cdot \vec{B}_1 = \vec{n} \cdot \vec{B}_2 \tag{5.2}$$

$$\vec{n} \times \vec{H}_1 = \vec{n} \times \vec{H}_2 \tag{5.3}$$

where $\vec{B}$ is the magnetic flux density, $\vec{H}$ is the magnetic field, and $\vec{n}$ is the unit normal to the interface. Eq. (5.2) and Eq. (5.3) may be rewritten in terms of the vector potential $\vec{A}$ as

$$\vec{n} \cdot (\bigtriangledown \times \vec{A}_1) = \vec{n} \cdot (\bigtriangledown \times \vec{A}_2) \tag{5.4}$$

$$\vec{n} \times \nu_1(\bigtriangledown \times \vec{A}_1) = \vec{n} \times \nu_2(\bigtriangledown \times \vec{A}_2). \tag{5.5}$$

Expanding Eq. (5.4) in components shows that there are just tangential variables involved. It follows that continuity of the normal component of the magnetic flux $\vec{B}$ density is ensured by setting the tangential components of the vector potential $\vec{A}$ to be continuous. Eq. (5.5) contains the natural interface condition of the variational functional for magnetostatics [29] and thus it is not necessary to set the normal components of the vector potential to be $\vec{A_{1n}} = \vec{A_{2n}}$. Imposing this continuity by the element shape functions leads to numerical convergence problems as mentioned in section (3.1.6.5).

An alternative to the node-based element is the *edge-element* [12],[13],[14],[15]. They have mostly been used to compute 3d vector fields in microwave engineering but are also well suited for magnetostatic applications. The field in the edge element is represented by a defined number of basis functions $\vec{N}_{e_i}$ associated with edges, rather than nodes:

$$\vec{A} = \sum_{i=1}^{N_e} A_i \, \vec{N}_{e_i} \tag{5.6}$$

where N_{e_i} is a polynomial on edge i of the finite element. The most important property from the point of view of magnetostatic field modelling is that they allow the normal component of the vector to be discontinuous from one element to the next Fig. (5.2).

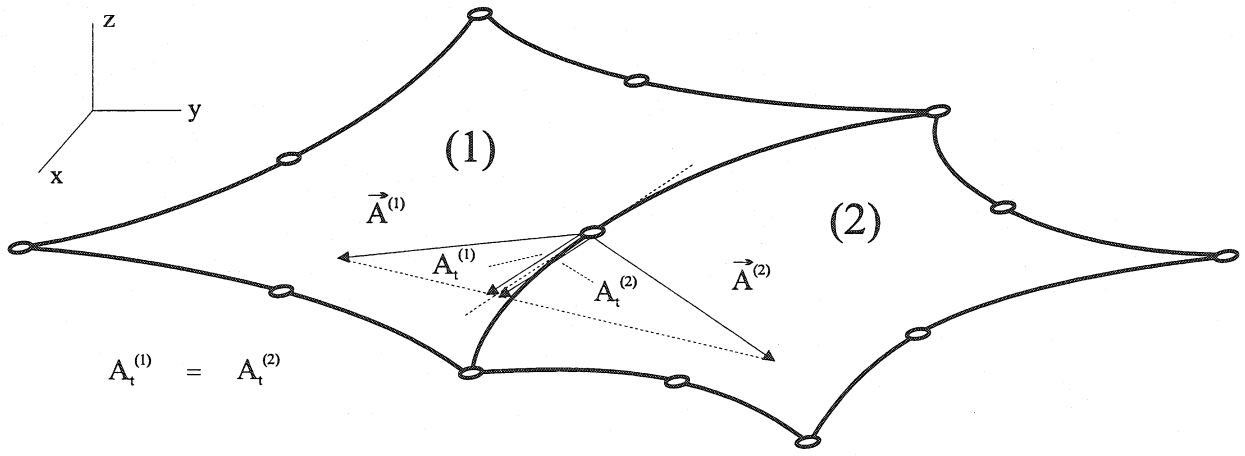

Figure 5.2: Continuity conditions between two adjacent edge-elements

Furthermore, they allow for the elimination of spurious modes of eigenvalue problems and gradient fields can be modelled exactly.

5.1.2 Tangential continuity

For the sake of simplicity we focuse on linear elements with 12 edges. A local coordinate system (ξ, η, ζ) is used for the interpolation of the field in the finite element domain. The mapping from the local to the global coordinate system is carried out using the same mapping procedure as for node-based elements:

$$\vec{r} = \sum_{i=1}^{n_n} f_i(\xi, \eta, \zeta)\,(\vec{e_x}\,x_i + \vec{e_y}\,y_i + \vec{e_z}\,z_i) \tag{5.7}$$

where f_i depends on the local coordinates. The field vector expressed in terms of the covariant coordinate directions [30] is :

$$\begin{aligned} \vec{A} = &\ A_\xi\,\vec{a^\xi} + A_\eta\,\vec{a^\eta} + A_\zeta\,\vec{a^\zeta} = \\ = &A_\xi \bigtriangledown \xi + A_\eta \bigtriangledown \eta + A_\zeta \bigtriangledown \zeta \end{aligned} \tag{5.8}$$

where $\vec{a^\xi}$, $\vec{a^\eta}$, and $\vec{a^\zeta}$ are the covariant coordinate directions shown in Fig. (5.3).

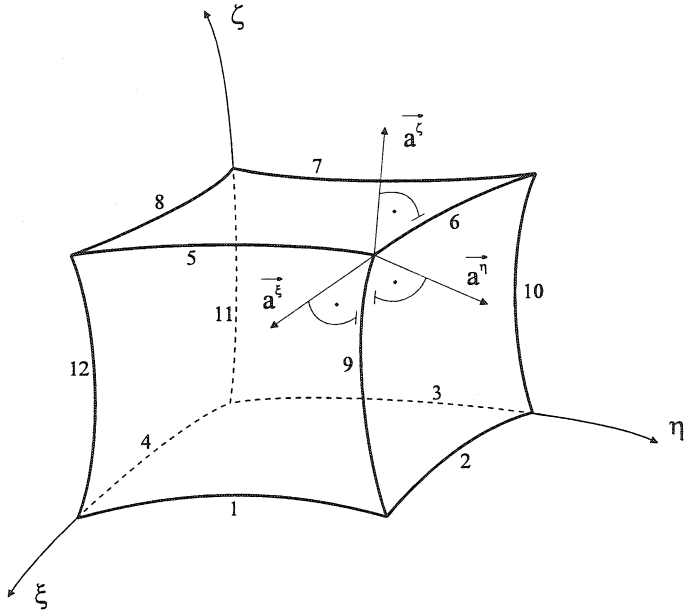

Figure 5.3: Hexahedral edge-element in the local coordinate system

The scalar coefficients A_ξ, A_η, and A_ζ are interpolated as:

$$A_\xi = \sum_{i=1}^{N_\xi} A_{\xi_i}\,N_{\xi_i}(\xi, \eta, \zeta) \tag{5.9}$$

$$A_\eta = \sum_{j=1}^{N_\eta} A_{\eta_j}\,N_{\eta_j}(\xi, \eta, \zeta) \tag{5.10}$$

$$A_\zeta = \sum_{k=1}^{N_\zeta} A_{\zeta_k}\,N_{\zeta_k}(\xi, \eta, \zeta). \tag{5.11}$$

To obtain the tangential continuity, the scalar functions in Eq. (5.9), Eq. (5.10), and Eq. (5.11) have to be chosen in the right manner. On edges, to which the covariant coordinate $\vec{a^i}$ is not perpendicular, they must be *zero* except on the edge to which they are assigned.
To ensure tangential continuity on edge one the assigned function must fulfil the following conditions:

$$N_{\xi_1} \neq 0 \qquad \text{on edge 1} \tag{5.12}$$
$$N_{\xi_1} = 0 \qquad \text{on edge 3,5,7} \tag{5.13}$$

whereas $\vec{a^\xi}$ is perpendicular to the edges 2,4,6,8,9,10,11, and 12.
Two different procedures of matching the tangential continuity are used, namely pointwise [31],[32] or edgewise [33]. In the latter the integrals of the interpolation functions along the edges are matched. The integrals are computed in the following way:

$$\int_{edge_i} N_{L_{kj}} \bigtriangledown L_k \, ds_j = \begin{cases} 1 & \text{if i = j} \\ 0 & \text{if i} \neq \text{j} \end{cases} \tag{5.14}$$

where L_k stands for the local coordinates (ξ, η, ζ). The order of the scalar functions n_N determines the number of the matching conditions which is always $(n_N + 1)$. Because of Eq. (5.6) and Eq. (5.14) the following relation for any edge of the global FE-mesh is valid:

$$\int_{edge_i} \vec{A} \cdot d\vec{s} \;=\; \sum_{i=1}^{n_e} A_i \int_{edge_i} \vec{N_{e_i}} \cdot d\vec{s} \;=\; A_{edge_i}. \tag{5.15}$$

A various number of different types of edge-elements for 2d as well as 3d problems have been developed [34]. Here a curvilinear hexahedral element with 36 degrees of freedom (DOF) [33] shown in Fig. (5.4) is applied.

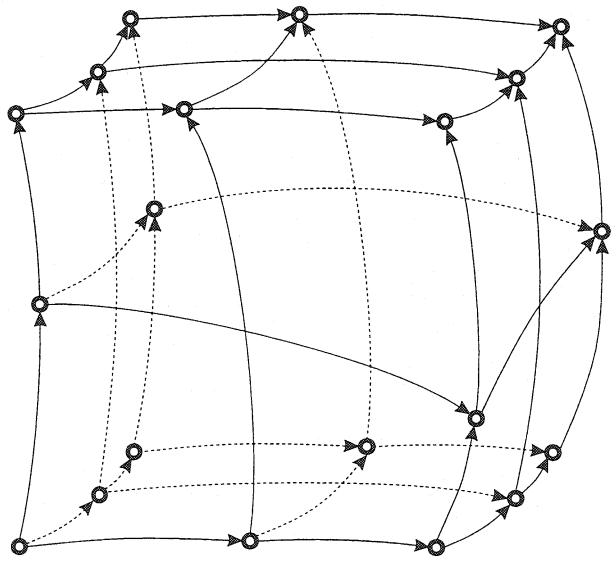

Figure 5.4: Curvilinear edge-element with 36 DOF's

5.2 The $\vec{A}_r$-formulation

The elementary model problem may be the same as it was introduced in chapter 3 for the $\vec{A}_r$-formulation with node-based elements (Fig. 3.5). It consists of two different volumes Ω_i and Ω_a where Ω_i is the iron region and Ω_a is the air region. These two volumes are connected to each other at the interface Γ_{ai}. The non conductive air region contains the conductor sources $\vec{J}_s$ which are not allowed to intersect the region Ω_i.

5.2.1 Field equations in terms of $\vec{A}_r$

The vector potential $\vec{A}$ according to its introduction in Eq. (3.88) is split up into

$$\vec{A} = \vec{A}_s + \vec{A}_r \tag{5.16}$$

where $\vec{A}_r$ is the reduced vector potential due to the magnetisation and $\vec{A}_s$ is the impressed vector potential due to the source currents in free space. Starting from Maxwell's equations for the magnetostatic case, pointed out in section (3.1), and considering that the current density $\vec{J}$ in Ω_i by definition is set to zero the differential equations are

$$\nabla \times \nu \nabla \times \vec{A}_{r_i} = -\nabla \times \nu \nabla \times \vec{A}_s \qquad \text{in } \Omega_i, \tag{5.17}$$

$$\nabla \times \nu_0 \nabla \times \vec{A}_{r_a} = 0 \qquad \text{in } \Omega_a. \tag{5.18}$$

The interface conditions at the boundary Γ_{ai} reduce to

$$(\nu_0 \nabla \times \vec{A}_{r_a} + \nu_0 \nabla \times \vec{A}_s) \times \vec{n}_a + (\nu \nabla \times \vec{A}_{r_i} + \nu \nabla \times \vec{A}_s) \times \vec{n}_i = 0 \qquad \text{on } \Gamma_{ai} \tag{5.19}$$

since the normal component of the magnetic flux density B_n is implicitly set continuous by the tangential continuity of the vector potential $\vec{A}$.
The complete $\vec{A}_r$-formulation assuming edge-elements therefore is

$$\nabla \times \nu \nabla \times \vec{A}_{r_i} = -\nabla \times \nu \nabla \times \vec{A}_s \qquad \text{in } \Omega_i, \tag{5.20}$$

$$\nabla \times \nu_0 \nabla \times \vec{A}_{r_a} = 0 \qquad \text{in } \Omega_a, \tag{5.21}$$

$$\nu \nabla \times \vec{A}_{r_i} \times \vec{n} = 0 \qquad \text{on } \Gamma_{H_i}, \tag{5.22}$$

$$\nu_0 \nabla \times \vec{A}_{r_a} \times \vec{n} = 0 \qquad \text{on } \Gamma_{H_a}, \tag{5.23}$$

$$\vec{n} \times \vec{A}_{r_i} = 0 \qquad \text{on } \Gamma_{B_i}, \tag{5.24}$$

$$\vec{n} \times \vec{A}_{r_a} = 0 \qquad \text{on } \Gamma_{B_a}, \tag{5.25}$$

and along the interface Γ_{ai}

$$(\nu_0 \nabla \times \vec{A}_{r_a} + \nu_0 \nabla \times \vec{A}_s) \times \vec{n}_a + (\nu \nabla \times \vec{A}_{r_i} + \nu \nabla \times \vec{A}_s) \times \vec{n}_i = 0 \qquad \text{on } \Gamma_{ai}. \tag{5.26}$$

5.2.2 Ritz's equations

The general Laplacian operators for both the region Ω_i and Ω_a are found to be the following:

$$\begin{aligned} \nabla \times \nu \nabla \times \vec{A}_{r_i} \; + \; & \delta_{\Gamma_{H_i}} \nu \nabla \times \vec{A}_{r_i} \times \vec{n} \; + \\ & \delta_{\Gamma_{ai}} \{ (\nu \nabla \times \vec{A}_{r_i} \; + \; \nu \nabla \times \vec{A}_s) \times \vec{n}_i \} \; + \\ & \delta_{\Gamma_{ai}} \{ (\nu_0 \nabla \times \vec{A}_{r_a} + \nu_0 \nabla \times \vec{A}_s) \times \vec{n}_a \} \; = -\nabla \times \nu \nabla \times \vec{A}_s \end{aligned} \tag{5.27}$$

in Ω_i, and

$$\nabla \times \nu_0 \nabla \times \vec{A}_{r_a} + \delta_{\Gamma_{Ha}} \nu_0 \nabla \times \vec{A}_{r_a} \times \vec{n} + \delta_{\Gamma_{ai}} \{(\nu_0 \nabla \times \vec{A}_{r_a} + \nu_0 \nabla \times \vec{A}_s) \times \vec{n_a}\} + \delta_{\Gamma_{ai}} \{(\nu_0 \nabla \times \vec{A}_{r_i} + \nu_0 \nabla \times \vec{A}_s) \times \vec{n_i}\} = 0 \quad (5.28)$$

in Ω_a. Both operators are symmetric and positiv according to the evidence described in section (3.1.4.2). Applying Ritz's method and approximating the vector potential as

$$\vec{A}_r \approx \vec{A}_r^n = \sum_{i=1}^{n_e} A_{r_i} \vec{N}_{e_i} \quad (5.29)$$

Ritz's equations are:

$$\int_{\Omega_i} \vec{N}_j \cdot (\nabla \times \nu \nabla \times \vec{A}_{r_i}^n)\, d\Omega + \int_{\Gamma_{H_i}} \vec{N}_j \cdot (\nu \nabla \times \vec{A}_{r_i}^n \times \vec{n})\, d\Gamma + \int_{\Gamma_{ai}} \vec{N}_j \cdot \{(\nu \nabla \times \vec{A}_{r_i}^n + \nu \nabla \times \vec{A}_s) \times \vec{n_i}\}\, d\Gamma + \int_{\Gamma_{ai}} \vec{N}_j \cdot \{(\nu_0 \nabla \times \vec{A}_{r_a}^n + \nu_0 \nabla \times \vec{A}_s) \times \vec{n_a}\}\, d\Gamma = -\int_{\Omega_i} \vec{N}_j \cdot (\nabla \times \nu \nabla \times \vec{A}_s)\, d\Omega \quad (5.30)$$

in Ω_i and

$$\int_{\Omega_a} \vec{N}_j \cdot (\nabla \times \nu_0 \nabla \times \vec{A}_{r_a}^n)\, d\Omega + \int_{\Gamma_{Ha}} \vec{N}_j \cdot (\nu_0 \nabla \times \vec{A}_{r_a}^n \times \vec{n})\, d\Gamma + \int_{\Gamma_{ai}} \vec{N}_j \cdot \{(\nu_0 \nabla \times \vec{A}_{r_a}^n + \nu_0 \nabla \times \vec{A}_s) \times \vec{n_a}\}\, d\Gamma + \int_{\Gamma_{ai}} \vec{N}_j \cdot \{(\nu \nabla \times \vec{A}_{r_i}^n + \nu \nabla \times \vec{A}_s) \times \vec{n_i}\}\, d\Gamma = 0 \quad (5.31)$$

in Ω_a for all $j = 1, \cdots, n$.
The vector functions $\vec{N}_{e_i}$ must satisfy the homogeneous Dirichlet boundary conditions

$$\vec{n} \times \vec{N}_{e_i} = 0 \quad \text{on } \Gamma_B. \quad (5.32)$$

With Green's identities shown in Eq. (3.121) and Eq. (3.122) and applying the condition of Eq. (5.32) Ritz's equations reduce to

$$\int_{\Omega_i}(\nabla \times \vec{N}_j \cdot \nu \nabla \times \vec{A}_{r_i}^{n})\, d\Omega \; + \int_{\Gamma_{ai}} \vec{N}_j \cdot \{\, (\nu_0 \nabla \times \vec{A}_{r_a}^{n} + \nu_0 \nabla \times \vec{A}_s) \times \vec{n_a} \,\}\, d\Gamma \; + = -\int_{\Omega_i}(\nabla \times \vec{N}_j \cdot \nu \nabla \times \vec{A}_s)\, d\Omega \quad (5.33)$$

in Ω_i, and

$$\int_{\Omega_a}(\nabla \times \vec{N}_j \cdot \nu_0 \nabla \times \vec{A}_{r_a}^{n})\, d\Omega \; + \int_{\Gamma_{ai}} \vec{N}_j \cdot (\nu_0 \nabla \times \vec{A}_s \times \vec{n_a})\, d\Gamma \; + \int_{\Gamma_{ai}} \{(\nu \nabla \times \vec{A}_{r_i}^{n} + \nu \nabla \times \vec{A}_s) \times \vec{n_i}\,\}\, d\Gamma = 0 \quad (5.34)$$

in Ω_a. Keeping in mind that $\vec{n_i} = -\vec{n_a}$ and adding up Eq. (5.33) and Eq. (5.34) Ritz's equations for $\Omega = \Omega_i \cup \Omega_a$ are:

$$\int_{\Omega_i}(\nabla \times \vec{N}_j \cdot \nu \nabla \times \vec{A}_{r_i}^{n})\, d\Omega \; + \int_{\Omega_a}(\nabla \times \vec{N}_j \cdot \nu_0 \nabla \times \vec{A}_{r_a}^{n})\, d\Omega = -\int_{\Omega_i}(\nabla \times \vec{N}_j \cdot \nu \nabla \times \vec{A}_s)\, d\Omega + \int_{\Gamma_{ai}} \vec{N}_j \cdot \{\, \nu_0 \nabla \times \vec{A}_s \times \vec{n_i} \,\}\, d\Gamma. \quad (5.35)$$

5.3 Why ungauged?

It was shown in section (3.1.2) that the set of Eq. (3.11) to Eq. (3.14) define the magnetic field uniquely whereas the vector potential is determined up to a gradient function. If gauging is neglected, this gradient function remains undefined. Using edge-elements, one way to fix this gradient function is by assigning certain values to the line integrals along the edges of a tree of the graph spanned by the finite element mesh [35].

(5.36) to (5.38) show the element shape functions of a curvilinear edge-element with 36 DOF's as shown in Fig. (5.4):

$$\{1, \eta, \zeta, \eta\zeta, \eta^2, \zeta^2, \eta\zeta^2, \zeta\eta^2\} \nabla \xi + \xi\{1, \eta, \zeta, \eta\zeta\} \nabla \xi \quad (5.36)$$

$$\{1, \xi, \zeta, \xi\zeta, \xi^2, \zeta^2, \xi\zeta^2, \zeta\xi^2\} \nabla \eta + \eta\{1, \xi, \zeta, \xi\zeta\} \nabla \eta \quad (5.37)$$

$$\{1, \xi, \eta, \xi\eta, \xi^2, \eta^2, \xi\eta^2, \eta\xi^2\} \nabla \zeta + \zeta\{1, \xi, \eta, \xi\eta\} \nabla \zeta. \quad (5.38)$$

This element is consistent or called a H(curl) element. H(curl) elements can model the null-space of a curl operator, which is a gradient field, exactly [34]. But not all of the shape functions are linearly independent, thus the dimension of the null-space of the curl operator is less than 36, namely 19 which is the number of tree-edges in the element.
This indeed leads to a singular matrix with zero eigenvalues but can be solved by the conjugate gradient method [36]. The convergence problems do not appear as long as the same dependence in the system matrix can be found on the rhs of the equation system.
In our particular case the second term on the rhs of Eq. (5.35) adversely effects the dependencies on the rhs of the equation system since the shape functions $\vec{N}_j$ are not differentiated. This causes convergence problems which in fact can be overcome by eliminating this term. It was assumed that the current density $\vec{J}_s$ in the iron region Ω_i is zero (see section (3.1.6.3)), i.e. the magnetic field $\vec{H}_s$ in Ω_i is curl-free. The identity

$$\bigtriangledown \cdot (\vec{N}_i \times \vec{H}_s) = \vec{H}_s \cdot (\bigtriangledown \times \vec{N}_i) \; - \; \vec{N}_i \cdot (\bigtriangledown \times \vec{H}_s) \tag{5.39}$$

integrated over the volume Ω_i reduces by applying the divergence theorem of Gauss:

$$\oint_{\Gamma_{ai}} (\vec{N}_i \times \vec{H}_s) \cdot \vec{n} \, d\Gamma = \int_{\Omega_i} \vec{H}_s \cdot (\bigtriangledown \times \vec{N}_i) \, d\Omega \; - \; \int_{\Omega_i} \vec{N}_i \cdot (\bigtriangledown \times \vec{H}_s) \, d\Omega. \tag{5.40}$$

The second term on the right hand side vanishes according to the assumption above and substituting the surface integral of Eq. (5.35) gives the Ritz equations as following

$$\int_{\Omega_i} (\bigtriangledown \times \vec{N}_j \cdot \nu \bigtriangledown \times \vec{A_{r_i}^n}) \, d\Omega \; + \; \int_{\Omega_a} (\bigtriangledown \times \vec{N}_j \cdot \nu_0 \bigtriangledown \times \vec{A_{r_a}^n}) \, d\Omega$$

$$= \int_{\Omega_i} (1 - \nu\mu_0)(\bigtriangledown \times \vec{N}_j) \cdot \vec{H}_s \, d\Omega. \tag{5.41}$$

Furthermore, the identification of the boundary Γ_{ai} and the calculation of the magnetic field on it can be omitted which saves indeed computing time. The same procedure is applied to the $\vec{A}_r$-formulation for the 2d case.

Chapter 6

Numerical Investigations in 3D

6.1 Comparison to 2D results

6.1.1 Description of the FE-model

A model was set up to evaluate the new FE-formulation presented in chapter 5. The model shown in Fig. (6.1) is based on the 2D cross-section of the LHC main dipole described in section (4.2). The cross-section of the coil is extended so that its magnetic field along the z-axis can be considered to be constant. Thus, a 2D harmonic analysis of the field at $z = 0$ can be performed. The iron yoke is reduced to just one layer of $d = 5mm$ thickness similar to the iron laminations of the real magnet model. Electrical boundary conditions are assigned to ensure $A_t = 0$ at the xy-planes at $z = 0$ and $z = d$.

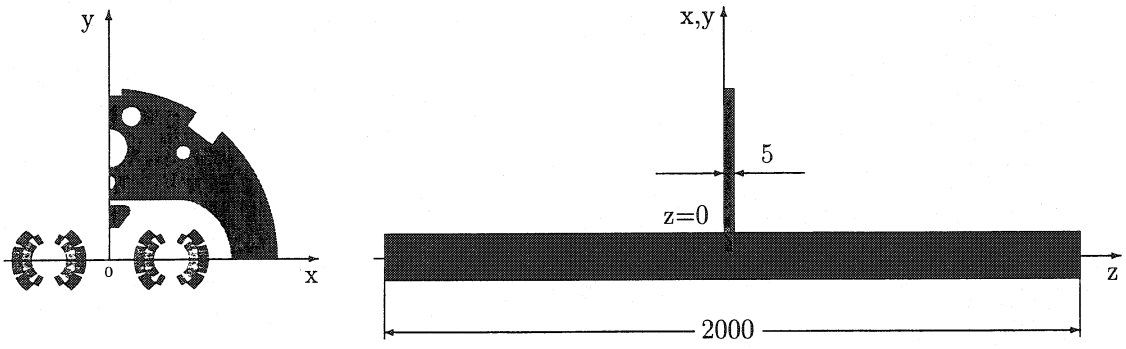

Figure 6.1: Three dimensional extension of the main dipole geometry for $B_z = const.$

6.1.2 Relative multipoles at nominal operation field

Table (6.1) gives the harmonics as calculated by the 2D and 3D reduced vector potential formulation. The magnitude of the z-component of the magnetic field B_z inside the aperture at $r = 10mm$ was found to be less than $10^{-12}T$.

Table 6.1: Relative multipole errors / 10^{-4} as calculated by FEM2D and FEM3D (at z=0)

	FEM2D	FEM3D
	Number of equations	
	36000	60000
n	norm. b_n	norm. b_n
1	−8.36880	−8.37450
2	1.28377	.96045
3	−.23928	−.27793
4	−.14875	−.14739
5	−.18650	−.18675
6	.00067	.00067
7	.03380	.03428
8	.00002	.00011
9	−.01026	−.01110
10	.00009	.00000
11	.00769	.00888

The results correspond quite well to each other even though two completely different types of finite elements are applied. The 2D results have been presented in Table (4.6).

6.2 The end configuration of the LHC main dipole model

The main objective concerning the iron saturation in the magnet ends to be studied are the peak fields in the conductor of the end turns of the coil. Since the ends are mechanically less rigid than the collared part of the coil, conductor placements due to the peak fields can cause quenches. The closer the ferromagnetic laminations get to the end turns the higher the induced peak fields are. Therefore, the very last part of the magnet-end configuration consists of non-magnetic laminations rather than ferromagnetic ones, as shown in drawing 06LHCMBP-N1060.

6.2.1 The magnet ends

The magnet end configuration considered for this study is shown in Fig. (6.2). The 2D cross-section is the same as in section (4.2). The design length of the coil end is $155mm$ and it starts off at $z = 400mm$. The iron yoke finishes at $z = 300mm$. This guarantees the iron to be sufficiently far away from the coil end and therefore it should not induce local peak fields in the end turns. Furthermore, the solenoidal part of the field induced by the coil end is considered to be decayed sufficiently so that it is negligible at $z = 0$.
Table (6.2) shows the 2D relative multipole errors as computed by the FEM2D and FEM3D packages. The 3D results are calculated at $z = 0$.

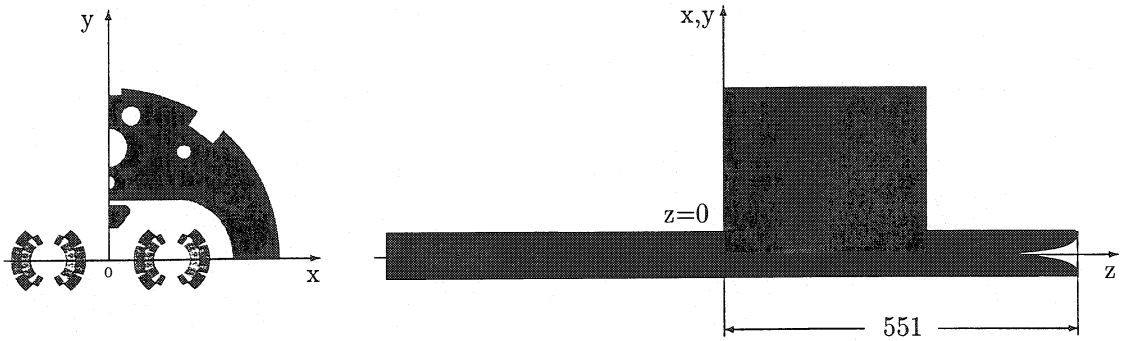

Figure 6.2: Magnet end configuration considered for the investigations

In order to obtain the solution on our AlphaStation 600 5/333 in a reasonable time, i.e. in about 24 h CPU-time, the number of equations of the FE-model was chosen to be around 300000. The 560 macro-elements of the 2D cross-section allow for 40 cuts in the z-direction which give the described number of equations above. This actually leads to a weak representation of the integrated coil field. Thus, the difference in the higher order multipoles can be explained. At least twice as many cuts in z-direction would be needed for a more accurate representation of the integrated coil field.

Table 6.2: Relative multipole errors / 10^{-4} as calculated by FEM2D and FEM3D (at z=0)

	FEM2D	FEM3D
	Number of equations	
	36000	286500
n	norm. b_n	norm. b_n
1	−8.36880	−8.36991
2	1.28377	1.27031
3	−.23928	−.19860
4	−.14875	−.14555
5	−.18650	−.20631
6	.00067	.01214
7	.03380	−.06044
8	.00002	.02193
9	−.01026	.07068
10	.00009	−.00644
11	.00769	.01048

6.2.2 Integrated multipoles in the magnet ends

The expression for the multipole expansion of the 2D field at the origin is given by

$$B_y + iB_x = B_1 \sum_{n=1}^{\infty} (b_n + ia_n)(z/r_0)^{n-1} \tag{6.1}$$

where r_0 is the reference radius and B_1 is the magnitude of the dipole field in the y-direction at the reference radius.

It can be shown that the same expression can be applied to the integrated multipoles $\int b_n$ of a complete end, if the coefficients are integrated with respect to z over the entire end [37]. The normal integrated multipoles $\int b_n$ are computed the following way:

$$\int b_n = \frac{\int_z B_n \, dz}{B_1} \tag{6.2}$$

where B_n are the normal multipoles at $z = z_i$ and B_1 is the dipole field of the straight section at $z = z_0$. The *fundamental*, $\int b_1$, expressed in unit-meters, when divided by 10^4 is the effective magnetic length l_{eff} of the end in meters.

Table 6.3: Integrated multipoles as calculated by FEM3D at 8.4T

	$\int b_1$	$\int b_2$	$\int b_3$	$\int b_4$	$\int b_5$	$\int b_6$
FEM3D	2755.29	−5.88	−0.56	−0.056	−0.177	0.002

Table (6.3) shows the integrated multipoles calculated over z at nominal operation field. The integration path goes from $z = 200mm$ to $z = 600mm$. The effective magnetic length l_{eff} was computed to be $l_{eff} = 275.53mm$. The integrated multipole errors in the ends are relatively small (in fact they were previously minimised using analytical methods). The biggest error is produced by the cross-talk resulting from the bare coil of the second aperture sticking out of the common two-in-one iron yoke. As can be seen in Fig. (6.2), the iron yoke ends at z=300 in order to reduce the peak field in the coils. This reduces, however, the screening of one aperture with respect to the other. Note that the quadrupole component of the straight section is in the order of 1.28 units. Compared to a two-in-one coil without iron yoke, where in the straight section a cross-talk of about 58 units of b_2 would be noticeable, the cross-talk in the bare coil ends is a order of magnitude less. Scaled to the magnetic length of the entire coil of about 14.2 m we get: two ends create two times 5.88 units on an effective magnetic length of $l_{eff} = 275.53mm$. The straight section contributes 1.28 units on a magnetic length of 13.65 m which yields an average quadrupole component of 1 unit over the entire length of the magnet.

6.2.3 Field components in the magnet ends

Fig. (6.3) shows the positioning of the paths in the xy cross-section where the variation of the field components along the z-axis is evaluated. The position a is the location of the beam axis,

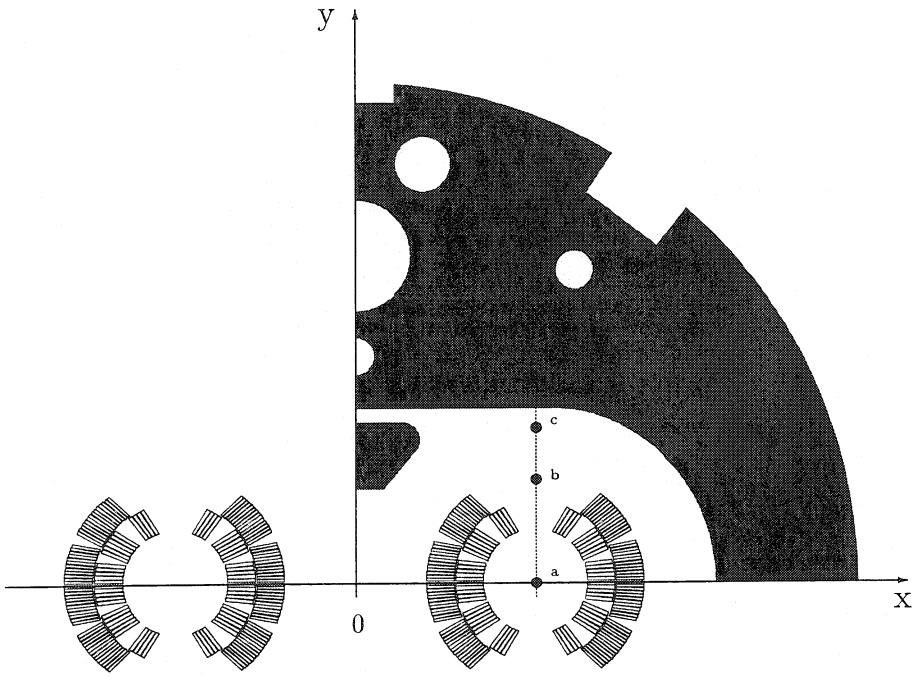

Figure 6.3: Positioning of the evaluation points for the field components (a ... beam axis, b ... y=60mm, c ... y=90mm)

i.e. at $x = 97mm$ and $y = 0$. The position b is at $y = 60mm$ and c at $y = 90mm$ respectively.

Fig. (6.5) shows the main dipole field B_1 as a function of z in the coil end. The field starts to go down at about $100mm$ inside the iron yoke and gets to its final 2D bare coil value of 7.41 T at about $120mm$ outside the iron yoke.

For values of z bigger than $400mm$ the field drops due to the onset of the coil end. The drop is very smooth, there are no local field enhancements visible in the main component.

The end of the iron yoke creates a fringing field with a noticeable z-component as can be seen in Fig. (6.7). The field is computed along the line c at a location of $y = 90$ mm above the beam axis as shown in Fig. (6.3) and Fig. (6.6). The z-component of the field is maximal slightly outside the end of the iron yoke at $z > 300mm$.

The closer in y-direction we get to the coil the lower is the influence of the iron yoke, i.e. the z-component of the field decreases considerably. The variation of the field components at $y = 60mm$ which is slightly above the outer coil radius is plotted in Fig. (6.9).

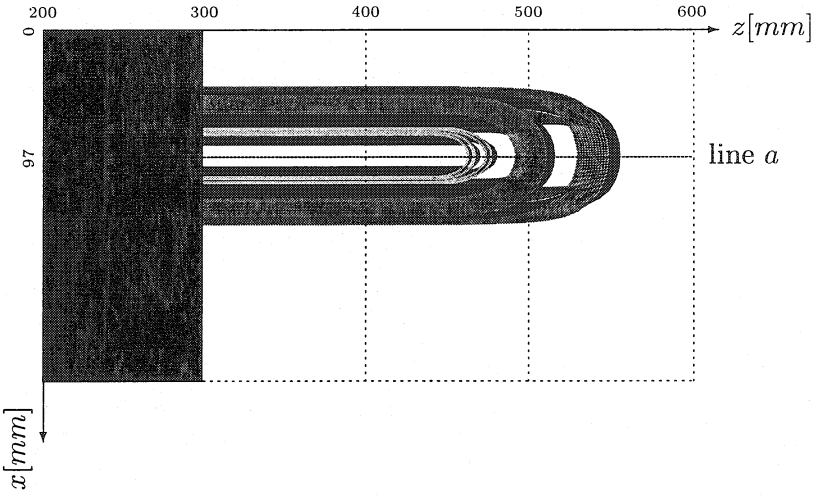

Figure 6.4: Principal view on the magnet end configuration

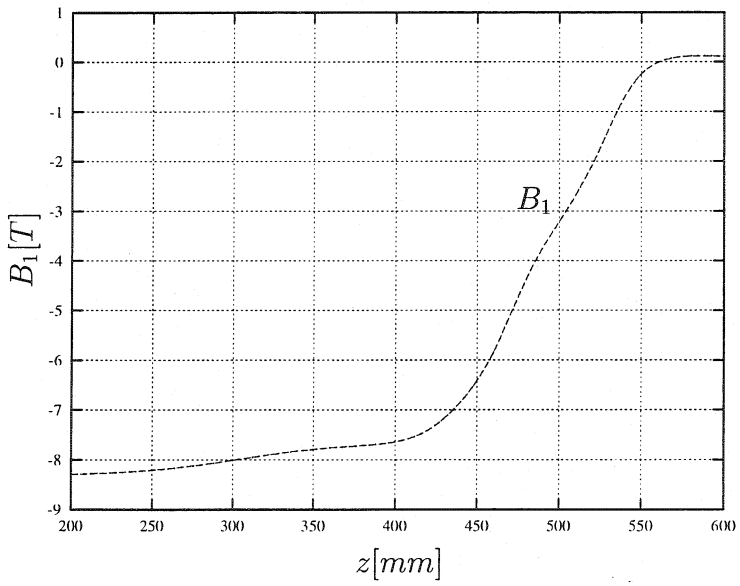

Figure 6.5: Variation of the dipole field B_1 in the magnet end along line a (see Fig. (6.3))

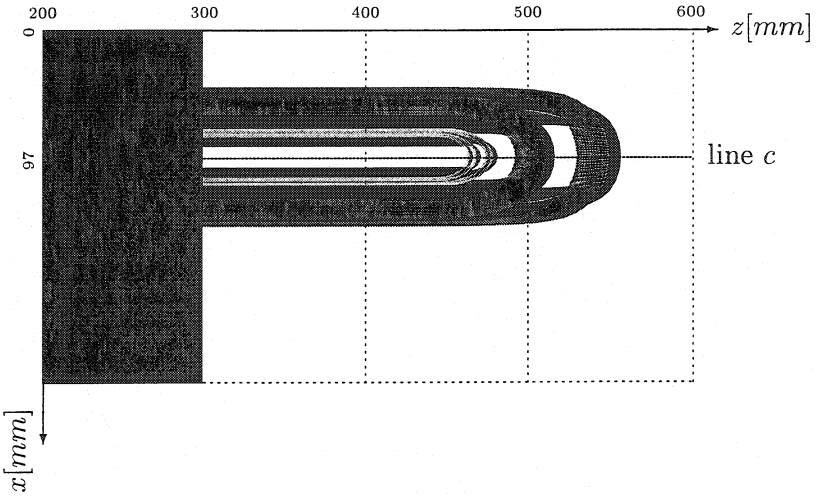

Figure 6.6: Principal view on the magnet end configuration

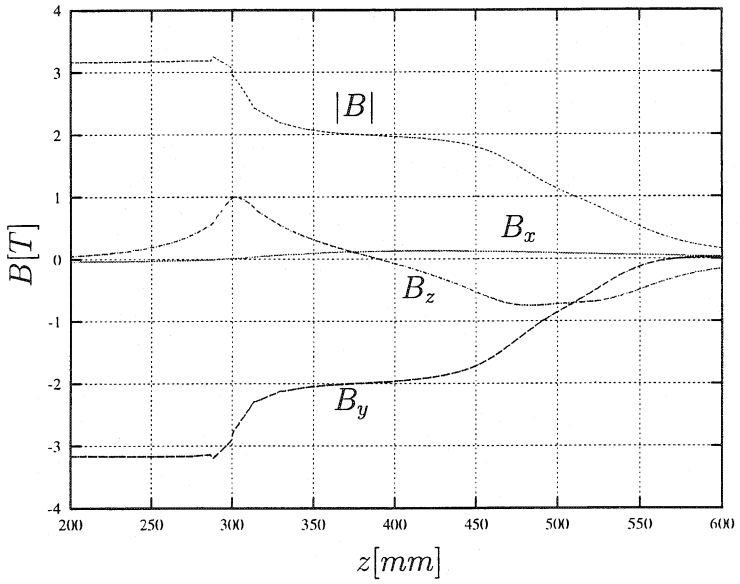

Figure 6.7: Field components and modulus of the magnetic field in the magnet end along line c (see Fig. (6.3))

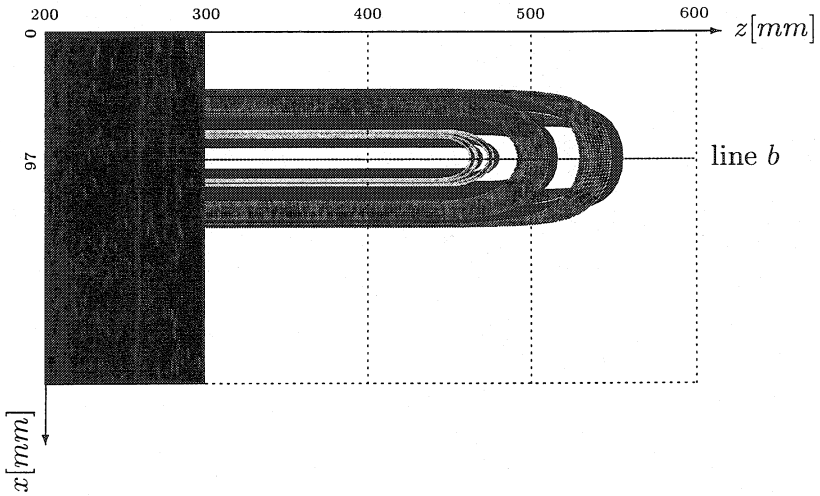

Figure 6.8: Principal view on the magnet end configuration

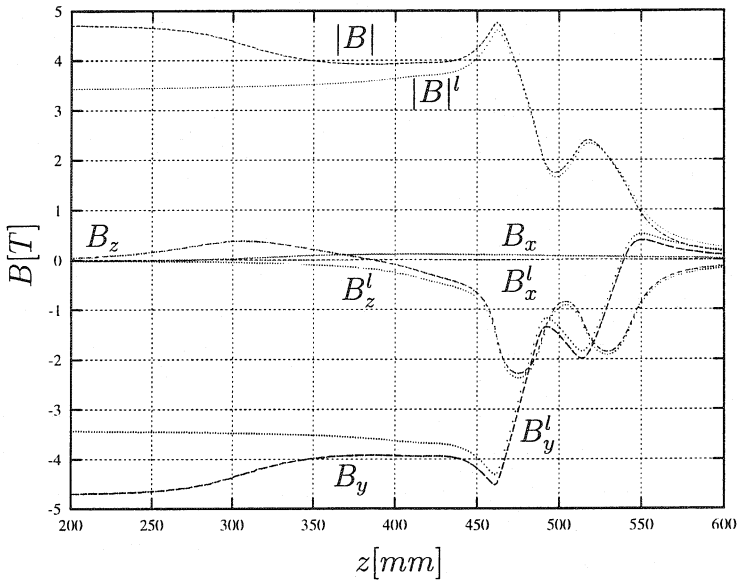

Figure 6.9: Field components and modulus of the magnetic field in the magnet end along line b (^{l} ... as calculated by means of the classical ROXIE program for linear iron)

There is a peak in the field-modulus at about $z = 470mm$ which results from the local field enhancement. The z-component is caused by the additional solenoidal field of the coil end.

The variation of the field-modulus is rather small between $z = 350mm$ and $z = 420mm$. This is interesting as the ferromagnetic laminations are replaced by stainless steel laminations in order to reduce the peak field in the coil, thus increasing the quench margin in the critical region. A bare straight section of about 100 mm is sufficient.

Fig. (6.9) also shows the field components for the linear case as calculated by Biot Savart's law for a "one-in-one" structure. Since there is no cross-talk which comes from a second aperture the field components B_x^l are therefore zero. Clearly visible is the influence of the saturated iron yoke on the field components for $z < 450mm$.

Chapter 7

Conclusions

The LHC, CERN's future extension of its accelerator complex, requires high field superconducting lattice dipoles and quadrupoles together with 30 different kinds of magnets. In total, there are more than 8400 magnet units to be build. Therefore, it is of major interest to provide the magnet designers with a tool which enables to perform an integrated magnet design, as described in section (1.2.1).

The classical ROXIE program is an approach to an integrated design tool for superconducting magnets with its feature-based creation of the 2D and 3D coil configurations, using mathematical optimisation techniques. Fig. (7.1) shows basically the main steps of the integrated design procedure, as they have been performed by means of the classical ROXIE program. In order to estimate the saturation induced field errors, an interface to commercially available FE-codes is provided.

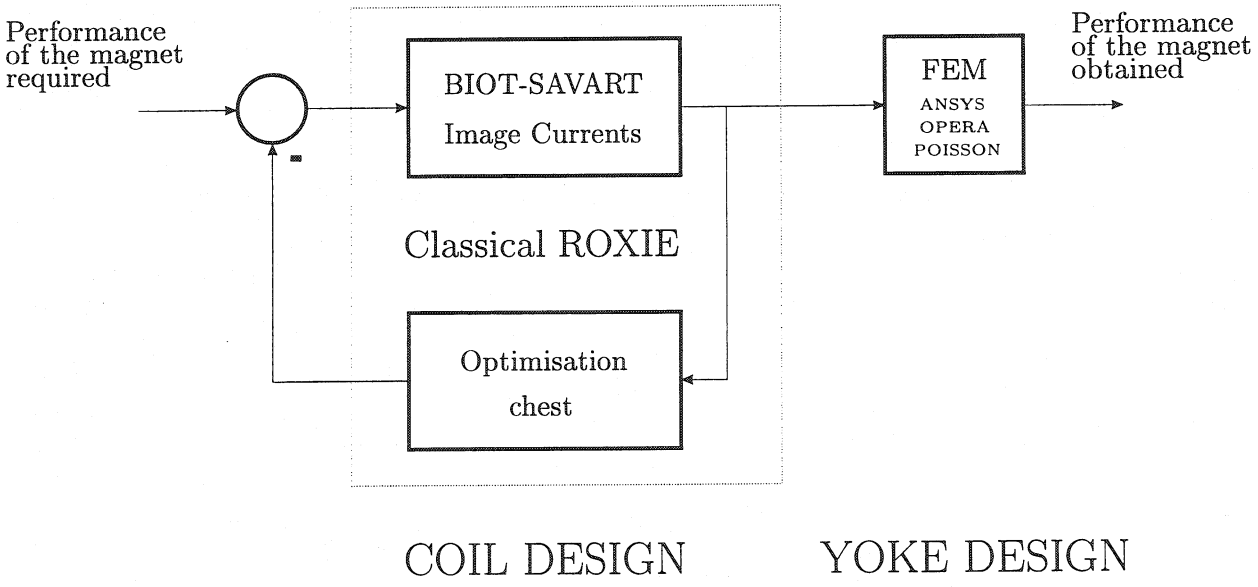

Figure 7.1: Integrated magnet design process with the classical ROXIE program and exporting coil data to FEM codes

The weak point of this procedure is that the yoke design depends on a different coil model. As it was shown in section (4.1.3), the remodelling of the complicated coil shapes with finite elements has a strong influence on the field errors. A simplified model based on a homogeneous current density distribution within the conductor blocks, i.e. the grading of the current density is neglected, as required by commercially available Finite Element packages based on a total vector potential formulation, is simply not adequate to achieve accurate results.

The basic idea of this work is to use the same coil model for the finite element calculation, as it is computed by the classical ROXIE program. Thus, a finite element code based on a reduced vector potential formulation was implemented and added to the classical ROXIE program. It takes, instead of the coils being part of the finite element mesh, the Biot-Savart field of the coils as its input representing the excitational field. In other words, the coils have been eliminated from the mesh grid. A further objective was to implement the FE-code so that it can be called from within the classical ROXIE program. With the characteristic input data for both the coil and the iron configuration to be parametric, it makes it possible to optimise a magnet without the intermediate step exporting data to an external finite element package.

A comparison between the commercially available FE-packages ANSYS, OPERA, POISSON and the $\vec{A}_r$-formulation showed that additional field errors due to the nature of the different types of finite elements appear. The explanation was found in the position of the sampling points of the Gauss quadrature within a finite element which is different in triangular and quadrilateral elements and thus is the integrated magnetic field of the coil. The distribution in quadrilateral elements is similar to the positioning of the line currents in the ROXIE program thus they allow for a better representation of the integrated coil field. The iron induced field errors for a simple one layer coil due to this effect are of the same magnitude compared to those where the grading of the current density is neglected. This effect gets even more pronounced for coils with two or more layers. Therefore, it has to be concluded that the application of a FE-package based on triangular elements in combination with the ROXIE program is not the optimal choice for the integrated design process of coil-dominated accelerator magnets.
Fig. (7.2) shows a cross-sectional view of a coil block, made out of Rutherford conductors with its superconducting strands. As it can be seen, the distribution of the strands vary within the conductors. This has as well a certain influence on the field distribution in coil dominated magnets as those found due to the distribution of the sampling points of the Gauss quadrature. Therefore, a modification of the conductor modelling as currently performed by the ROXIE program should be investigated.

A major advantage of the $\vec{A}_r$-formulation is the substitution of further conductors to the FE-model. The mesh grid does not change no matter where additional conductors are placed. The influence on the field errors due to bus-bars, as presented in section (4.3.3), or due to shifted coils, as presented in section (4.3.4), can be computed keeping the same mesh grid.

The 3D extension of the reduced vector potential formulation, based on edge-elements, has been presented in chapter 5. The classical formulation using node-based elements is not suited for the 3D implementation. Convergence problems arise due to an incomplete repre-

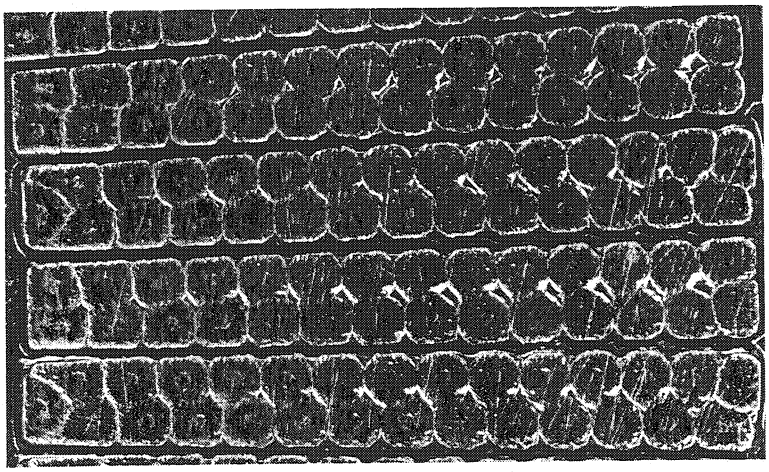

Figure 7.2: Cross-sectional view of a conductor block with the Rutherford cable and its superconducting strands

sentation of the term $(\nu \bigtriangledown \cdot \vec{A}) \cdot \vec{n}$ on the boundary Γ_{ai}. In order to overcome these convergence problems, the rhs of the equation system was reduced by the surface integral on the boundary Γ_{ai}, as discussed in section (5.3). This lead to an improvement of this formulation since the identification of the boundary Γ_{ai} falls off.

The investigations presented in section (6.1.2) have demonstrated the applicability of the 3D reduced vector potential formulation to accelerator magnets. Concerning the computational means that have been currently available (AlphaStation 600 5/ 333 MHz with 576 MB) to our group, it must be said, that the accuracy of the solution of a real 3D application is far from being the same as the one for the 2D case. The maximum number of equations for a 3D problem is around 300000 supposed one gets a result in reasonable time which is about 24 hours CPU-time. Nevertheless, the analysis presented in section (6.2.1) shows that the lower order multipoles correspond quite well with each other which, however is not true for higher order multipoles. This indicates an insufficient discretisation of the iron domain which results in a weak representation of the excitational field.

In view of a comparison of calculated results to measurements, the modelling has turned out to be of major importance. Several investigations on the ends of the MBSMS model magnets [3], altogether including 6 magnets, were carried out but there was no correlation found between calculation and measurements. Therefore, no further results have been presented. As a matter of fact, remarkable conductor displacements in the coils were observed which do not correspond with the nominal design. The input format for the coil blocks of the ROXIE program is block-orientated and therefore the treatment of single misaligned conductors in a coil block is rather difficult. Furthermore, the hardware components of the measurement facility with their connections placed next to the ends may influence the field distribution as well. Therefore, they should be considered in the modelling too.

The integration of the Biot-Savart field can be very time-consuming especially for the 3D case. This is sometimes considered to be a major drawback of the class of FE-formulations

based on a reduced potential. In our case, the emphasis is rather put on an accurate solution than on CPU-time spent on the computation of the excitational field. It was found that approximately 10 % of the total CPU-time are needed to compute the excitational field of a highly saturated magnet.

In my opinion, the methods presented in this thesis are well suited for the estimation of the saturation induced field errors of coil dominated accelerator magnets. In view of the FE-formulation applied to the integrated design process it has to be stated that consistency in the modelling of the coil is essential. This is ensured by applying the reduced vector potential formulation.

Nomenclature

Magnetostatic field equations

B	Magnetic flux density	$[T]$
H	Magnetic field strength	$[Am^{-1}]$
μ	Material permeability	$[VsA^{-1}m^{-1}]$
μ_0	Material permeability of vacuum	$[VsA^{-1}m^{-1}]$
ν	Material reluctivity	$[AmV^{-1}s^{-1}]$
ν_0	Material reluctivity of vacuum	$[AmV^{-1}s^{-1}]$
K	Surface current	$[Am^{-1}]$
b_m	Fictitious magnetic charge density	$[Vsm^{-2}]$
α	Function describing the tangential components of the vector potential	$[Tm]$
ψ_i	Surface flux	$[Vs]$
U_m	Magnetic voltage	$[A]$
A	Total magnetic vector potential	$[Tm]$
A_t	Tangential component of A	$[Tm]$
ϕ	Reduced magnetic scalar potential	$[A]$
ψ	Total magnetic scalar potential	$[A]$
A_r	Reduced magnetic vector potential	$[Tm]$
A_{r_i}	Reduced magnetic vector potential in the iron region	$[Tm]$
A_{r_a}	Reduced magnetic vector potential in the air region	$[Tm]$
A_s	Impressed magnetic vector potential	$[Tm]$
H_s	Impressed magnetic field strength	$[Am^{-1}]$
J	Current density	$[Am^{-2}]$
J_s	Source current density	$[Am^{-2}]$

Harmonic multipole analysis

B_1	Magnitude of dipole field in the y direction	$[T]$
B_y	Real part of the dipole field	$[T]$
B_x	Imaginary part of the dipole field	$[T]$

b_n	Normal multipole	–
a_n	Skew multipole	–
z	Complex plane	–
i	Imaginary unit	–
x	Real axis	–
y	Complex axis	–
r_0	Reference radius for the harmonic analysis	$[m]$
$\int b_i$	Integrated multipoles	$[unit - meters]$
$\int b_1$	*fundamental* at r_0	$[unit - meters]$
l_{eff}	effective magnetic length of the magnet end configuration	$[m]$

Finite Element Method

$f_k^{(e)}$	Element shape functions of node-based elements	–
N_{e_i}	Element shape functions of edge-based elements	–
η, ξ, ζ	Local coordinates	$[m]$
η_k, ξ_k, ζ_k	Local coordinates of a node	$[m]$
L_k	Local coordinates of a node	$[m]$
x_k, y_k, z_k	Global coordinates of a node	$[m]$
$x(\xi, \eta, \zeta)$	Global coordinates of an element	$[m]$
$y(\xi, \eta, \zeta)$	"	$[m]$
$z(\xi, \eta, \zeta)$	"	$[m]$
u	Potential function to be approximated	$[A]$
$u^{(e)}(x, y, z)$	Potential function in an element	$[A]$
u_k	Value of the potential in the node k	$[A]$
e_x, e_y, e_z	Cartesian unit vectors	[1]

Ritz's Method

u	Unknown potential function	$[A]$
L	Second order elliptic differential operator	$[m^{-2}]$
f	Forcing function	$[Am^{-2}]$
$W^{(u)}$	Potential energy in a magnetostatic system	$[J]$
f_i	Entire function set	–
u_D	Function satisfying the inhomogeneous Dirichlet BC	$[A]$
$a_i^{(n)}$	Coefficients of the equation system	$[A]$
δ_Γ	General Dirac function	$[m^{-1}]$
Ω	Region of the elementary model problem	–

Γ	Boundary of the region Ω	–
n	Outer normal vector	–
n_i	Outer normal vector of the iron region	–
n_a	Outer normal vector of the air region	–

Multipole expansion

I	Line current	$[A]$
r_a	Field point	$[m]$
r_q	Source point	$[m]$
R	Distance between r_q and r_a	$[m]$
ξ	Arbitrary complex number	–
ϕ	Angle of source point (Polar coordinates)	$[rad]$
Θ	Angle of field point (Polar coordinates)	$[rad]$
B_x	Field component (Cartesian coordinates)	$[T]$
B_y	Field component (Cartesian coordinates)	$[T]$
B_r	Field component (Polar coordinates)	$[T]$
B_Θ	Field component (Polar coordinates)	$[T]$
B_z	Field component (Polar coordinates)	$[T]$
I_ϕ	Uniform current distribution on a cylinder	$[A]$
I_0	Amplitude of the current distribution	$[A]$
$A_z(r_a, \Theta)$	Vector potential generated by a line current in z direction	$[Tm]$
$A_z(r, \Theta)$	Vector potential generated by the current distribution $I_{(\phi)}$	$[Tm]$
a_n	Skew multipole	–
b_n	Normal multipole	–
α_0	inclination angle of a conductor	$[rad]$
ϕ_0	positioning angle of a conductor	$[rad]$

Cable characteristics

B_i	Field in operating point of coil block i	$[T]$
J_i	Current in operating point of coil block i	$[Amm^{-2}]$
B_{ss_i}	Short sample field for coil block i	$[T]$
J_{ss_i}	Short sample current for coil block i	$[Amm^{-2}]$
$B_{c,0}$	Reference field	$[T]$
$T_{c,0}$	Reference temperature	$[K]$
$I_{c,0}$	Critical current at $(B_{c,0}, T_{c,0})$	$[A]$
$J_{c,0}$	Critical current density at $(B_{c,0}, T_{c,0})$ in the superconducter	$[Amm^{-2}]$

J_c	Current density in the superconducter	$[Amm^{-2}]$
$\frac{dJ_c}{dB}$	Field dependence of J_c	$[Amm^{-2}T^{-1}]$
A_{sc}	Area of the SC strands in the cable	$[mm^2]$
I_{cable}	Total current in the cable	$[A]$
d	Strand diameter	$[mm]$
n	Number of strands in the cable	–
$\frac{Cu}{Sc}$	Copper to Superconductor ratio	–

Subscripts

a	Air
c	critical
e	Element
$edge$	Edge
i	Iron or numerical index
k	Node or edge of an element
m	magnetic
s	Source
sc	superconducting
ss	short sample
r	reduced
red	reduced
$c,0$	critical at reference temperature
t	tangential
tot	total
x, y, z	Cartesian coordinates
B	Magnetic flux density
D	Dirichlet
H	Magnetic field strength
0	Vacuum
ϕ	Reduced scalar potential
ψ	Total scalar potential

Superscripts

(e)	Element
(n)	Number of equation
(u)	Potential function

l	linear iron
(ξ,η,ζ)	Covariant coordinates

References

[1] The LHC Study Group. *The Yellow Book, LHC - The Large Hadron Collider - Conceptual Design.* CERN/AC/95-5(LHC), 1995.

[2] R. Perin. Superconducting Magnets for the Large Hadron Collider. *LHC Project Report 52*, 1996. 10^{th} General Conference of the European Physical Society Sevilla - Spain.

[3] N. Andreev et. al. The 1 m Long Single Aperture Dipole Coil Test Program for LHC. *LHC Project Report 25*, July 1996. 10^{th} General Conference of the European Physical Society.

[4] M. Chorowski et. al. A Simplified Cryogenic Distribution Scheme for the Large Hadron Collider. *Proceedings of the CEC/ICMC 1997*, July 1997.

[5] S. Russenschuck. A Computer Program for the Design of Superconducting Accelerator Magnets. *LHC Note 354*, 1995.

[6] S. Russenschuck, C. Paul, and K. Preis. ROXIE - A Feature Based Design and Optimization Program for superconducting Accelerator Magnets. *LHC Project Report 46*, 1996.

[7] O. Birò and K. R. Richter. *CAD in Electromagnetism*, volume 82 of *Advances in Electronics and Electron Physics*, pages 1 – 96. Academic Press, 1991.

[8] J. Simkin and C. W. Trowbridge. Three dimensional non-linear electromagnetic field computations using scalar potentials. *Proceedings of IEE*, 127(6), 1980.

[9] C. A. Magele, O. Birò, and K. Preis. Solution of TEAM Workshop Problem No. 13. *Proceedings of the* 4^{th} *Int. IGTE Symposium and European TEAM Workshop*, pages 283 – 287, October 1990.

[10] K. Preis, I. Bardi, O. Birò, C. Magele, W. Renhart, K. R. Richter, and G. Vrisk. Numerical Analysis of 3D Magnetostatic Fields. *IEEE Trans. on Magnetics*, 27(5):3798 – 3803, 1991.

[11] K. Simonyi. *Theoretische Elektrotechnik.* VEB Deutscher Verlag der Wissenschaften, Berlin, 10 edition, 1993.

[12] J. C. Nèdèlec. Mixed Finite Elements in R^3. *Numer. Math.*, 35:315 – 341, 1980.

[13] J. F. Lee and Z. J. Cendes. Tangential Vector Finite Elements for Electromagnetic Field Computation. *IEEE Trans. on Magnetics*, 27:4032 – 4035, 1991.

[14] J. S. Wang and N. Ida. Curvilinear and higher order 'Edge' elements in electromagnetic field computation. *IEEE Trans. on Magnetics*, 29:1491 – 1493, 1992.

[15] J. P. Webb. Edge Elements and what They can do for You. *IEEE Trans. on Magnetics*, 29(2):1460 – 1465, 1993.

[16] P. J. Bryant and K. Johnsen. *The principles of Circular Accelerators and Storage Rings.* Cambridge University Press, 1993.

[17] K.H. Mess. Superconducting Accelerator Magnets. *CAS - Superconductivity in Particle Accelerators*, March 1989. CERN 89-04.

[18] B. J. Holzer. Impact of Perisitent Currents on Accelerator Performance. *CAS - Superconductivity in Particle Accelerators*, May 1996. CERN 96-03.

[19] Ph. Lebrun. Operating at 1.8 K: The Technology of Superfluid Helium. *CAS - Superconductivity in Particle Accelerators*, May 1996. CERN 96-03.

[20] M. Linder et al. Construction details and test results from RHIC sextupoles. *IEEE Trans. on Magnetics*, 30(4):1730 – 1733, 1994.

[21] P. M. McIntyre, R. M. Scanlan, and W. Shen. Ultra-high-field magnets for future hadron collider. *Proc. ASC-94*, October 1994.

[22] A. Faus-Golfe. Minimization of the ramp-induced non-linear field imperfections in LHC . *LHC Project Note 9*, May 1995.

[23] S. Russenschuck and T. Tortschanoff. Mathematical Optimization of Superconducting Accelerator Magnets. LHC Note 246. CERN, AT-MA.

[24] M.N. Wilson. *Superconducting Magnets.* Oxford University Press, 1983.

[25] A. R. Mitchell and D. F. Griffiths. *The Finite Difference Method in Partial Differential Equations.* John Wiley and Sons, New York, 1980.

[26] S. C. Mikhlin. *Variational methods in Mathematical Physics.* Macmillan, 1964.

[27] O. C. Zienkiewicz. *The Finite Element Method.* MacGraw-Hill Book Company (UK) Limited, 3 edition, 1977.

[28] R. Wolf. *Private communications.* CERN/LHC-MMS.

[29] M. L. Barton and Z. J. Cendes. New vector finite elements for three-dimensional magnetic field computation. *J. Appl. Phys.*, 61(8):3919 – 3921, 1987.

[30] J. A. Stratton. *ELECTROMAGNETIC THEORY.* Mc Graw-Hill Book Company, Inc., New York and London, 1941.

[31] R. Miniowitz and J. P. Webb. Covariant-Projection Quadrilateral Elements for the Analysis of Waveguides with Sharp Edges. *IEEE Trans. on Microwave Theory Techn.*, 39:501 – 505, March 1991.

[32] J.P. Webb and R. Miniowitz. Analysis of 3D microwave resonators using covriant-projection elements . *IEEE Trans. on Microwave Theory Techn.*, 39:1895 – 1899, November 1991.

[33] A. Kameari. Calculation of transient 3D eddy current using edge-elements. *IEEE Trans. on Magnetics*, 26:466 – 469, March 1990.

[34] I. Bardi, R. Birò, O.and Dyczij-Edlinger, K. Preis, and K. R. Richter. Higher Order Edge Finite Elements in Electromagnetic Field Modelling. *1995 Digest of the USNC/URSI Radio Science Meeting*, June 1995.

[35] R. Albanese and G. Rubinacci. Solution of three dimensional eddy current problems by integral and differential methods. *IEEE Trans. on Magnetics*, 24:98 – 101, 1988.

[36] K. Preis, I. Bardi, O. Birò, C. Magele, G. Vrisk, and K. R. Richter. Different Finite Element Formulations of 3D Magnetostatic Fields. *IEEE Trans. on Magnetics*, 28(2):1056 – 1059, 1992.

[37] F. E. Mills and G. H. Morgan. A Flux Theorem for the Design of Magnet Coil Ends. *Particle Accelerators*, 5:227 – 235, 1973.